(2)

NSWC TR 86-253

NONAXISYMMETRIC BODY, SUPERSONIC, AERODYNAMIC PREDICTION

BY LEROY DEVAN
WEAPON SYSTEMS DEPARTMENT

AUGUST 1987

NAVAL SURFACE WEAPONS CENTER
Dahlgren, Virginia 22448-5000 • Silver Spring, Maryland 20903-5000

UNCLASSIFIED
SECURITY CLASSIFICATION OF THIS PAGE

A189538

REPORT DOCUMENTATION PAGE

1a. REPORT SECURITY CLASSIFICATION UNCLASSIFIED	1b. RESTRICTIVE MARKINGS
2a. SECURITY CLASSIFICATION AUTHORITY	3. DISTRIBUTION/AVAILABILITY OF REPORT Approved for public release; distribution is unlimited.
2b. DECLASSIFICATION/DOWNGRADING SCHEDULE	
4. PERFORMING ORGANIZATION REPORT NUMBER(S) NSWC TR 86-253	5. MONITORING ORGANIZATION REPORT NUMBER(S)
6a. NAME OF PERFORMING ORGANIZATION Naval Surface Weapons Center 6b. OFFICE SYMBOL (If applicable) G23	7a. NAME OF MONITORING ORGANIZATION
6c. ADDRESS (City, State, and ZIP Code) Dahlgren, VA 22448-5000	7b. ADDRESS (City, State, and ZIP Code)
8a. NAME OF FUNDING SPONSORING ORGANIZATION 8b. OFFICE SYMBOL (If applicable)	9. PROCUREMENT INSTRUMENT IDENTIFICATION NUMBER
8c. ADDRESS (City, State, and ZIP Code)	10. SOURCE OF FUNDING NOS. PROGRAM ELEMENT NO. / PROJECT NO. / TASK NO. / WORK UNIT NO.

11. TITLE (Include Security Classification)
Nonaxisymmetric Body, Supersonic, Aerodynamic Prediction

12. PERSONAL AUTHOR(S)
Devan, Leroy

13a. TYPE OF REPORT	13b. TIME COVERED	14. DATE OF REPORT (Yr., Mo., Day)	15. PAGE COUNT
Final	FROM _TO	1987, August	93

16. SUPPLEMENTARY NOTATION

17. COSATI CODES		
FIELD	GROUP	SUB. GR.

18. SUBJECT TERMS (Continue on reverse if necessary and identify by block number)
Supersonic Flow Computational Model
Nonaxisymmetric Body Skin Friction ;
Inviscid Flow Regime Base Drag
Viscous Crossflow Lift

19. ABSTRACT (Continue on reverse if necessary and identify by block number)

A supersonic flow computational model was developed for flight vehicles with nonaxisymmetric bodies. The bodies may be pointed, with arbitrary initial cross section, or blunted, with initially circular cross section; the remainder of the body may have an arbitrary cross-sectional variation. A vertical plane of symmetry is assumed except for fin deflections. The body is divided into piecewise continuous sections by planar discontinuities including inlets. All sections, except for the first one, may have fin sets. The fins, up to six per set, (1) are assumed to be aligned with a cylindrical coordinate ray, (2) depart only slightly from the midplane (thin fin approximation), and (3) are symmetric about the midplane.

20. DISTRIBUTION/AVAILABILITY OF ABSTRACT	21. ABSTRACT SECURITY CLASSIFICATION	
X UNCLASSIFIED/UNLIMITED SAME AS RPT. DTIC USERS	UNCLASSIFIED	
22a. NAME OF RESPONSIBLE INDIVIDUAL Leroy Devan	22b. TELEPHONE NUMBER (Include Area Code) 703-663-7443	22c. OFFICE SYMBOL G23

DD FORM 1473, 84 MAR EDITION OF 1 APR 83 IS OBSOLETE.

UNCLASSIFIED
SECURITY CLASSIFICATION OF THIS PAGE

19. (Cont.)

For the low Mach-number range, new research was developed for the inviscid flow regime (constitutes the major portion of this report). The computational model is based on a finite-difference, second-order, linear, potential solution. For pointed bodies, the computation is implicit up to the first planar body discontinuity and an explicit MacCormack scheme thereafter. Blunt body computations (1) assume an effective origin of disturbances and a modified Newtonian pressure distribution up to a matching or starting plane and (2) utilize an explicit solution thereafter. Local "jump" relations for discontinuities on the body, at fin roots, and fin edges are conservation relations obtained by applying the method of "weak solutions" to first- and second-order equations. For subsonic or slightly supersonic edges, adhoc heuristic assumptions are made.

At high Mach numbers, where linear methods are not applicable, local pressure coefficient models were adapted for predicting the inviscid loading contributions.

Viscous contributions are evaluated using approximate methods for estimating skin friction, base drag, and viscous crossflow lift.

FOREWORD

This work was conducted in order to develop a capability to predict aerodynamic loading for supersonic Mach numbers on nonaxisymmetric flight vehicles using rapid/accurate computational models. The resulting computer program, which will be described in a later report, allows one to predict static aerodynamics in the preliminary and intermediate design stage.

Support for the work was provided by the following sponsors:

1. Aerodynamics and Structures Block of the Surface-Launched Weaponry Technology Program, Project Numbers RS32-392E/RS32-392 4208

2. Tactical Missile and Air Warfare Block Program for Surface/Aerospace Weaponry and Missile Propulsion Technology, Project Number RW32-395

3. NSWC IR Funds

4. AFATL/DLCA, Eglin AFB
   A minor support contract was let to ASG of Rockville, Maryland.

This report was reviewed and approved by Dr. F. G. Moore, Head, Aeromechanics Branch and C. A. Cooper, Head, Missile Systems Division.

Released by:

J. L. SLOOP, Deputy Head
Weapon Systems Department

ACKNOWLEDGEMENTS

Dr. F. G. Moore has expressed an interest in developing the current capability since FY78. The current work effort was initiated in FY82.

L. A. Kania, who is currently employed by Martin-Marietta (Orlando), contributed significantly to the work during FY83-FY85 and was a second author for two AIAA meeting papers.

J. Hase implemented the high Mach number local solution methods and assisted in coding the skin friction and base pressure routines.

Contributors to the graphics in the report were R. Buchburger, D. Falabella, and ASG of Rockville, Maryland.

CONTENTS

Section		Page
1.0	INTRODUCTION	1
2.0	GEOMETRY, FREE-STREAM VELOCITY, AND FORCE CONVENTIONS	2
	2.1 BODY GEOMETRY	2
	2.2 FIN GEOMETRY	2
	2.3 FREE-STREAM VELOCITY VECTOR	4
	2.4 FORCE CONVENTION	4
	2.5 SYMMETRY CONSIDERATIONS AND NONZERO FORCE COEFFICIENTS	4
3.0	THEORETICAL DEVELOPMENT FOR THE FIRST- AND SECOND-ORDER POTENTIAL SOLVERS	4
	3.1 FIRST- AND SECOND-ORDER POTENTIAL EQUATIONS	4
	3.2 COMPUTATIONAL COORDINATES AND GRIDS	6
	3.3 VELOCITY ADVANCEMENT EQUATIONS IN ξ, θ COORDINATES	7
	3.4 IMPLICIT MARCHING SOLUTION	9
	3.5 PLANAR BODY DISCONTINUITY JUMP CONDITIONS	11
	3.6 EXPLICIT MARCHING SOLUTION OVER CONTINUOUS BODY SECTIONS	14
	3.7 BLUNT BODY SOLUTION	17
	3.8 FIN EDGE TREATMENT AND SURFACE DISCONTINUITIES	18
	3.9 FIN SURFACE ADVANCEMENT EQUATIONS	22
	3.10 FIN-BODY CORNER ADVANCEMENT EQUATIONS	25
	3.11 EXPLICIT FINITE-DIFFERENCE SCHEME	26
4.0	HIGH MACH NUMBER INVISCID SOLUTION	29
5.0	INVISCID LOADING COEFFICIENTS	29
6.0	SKIN FRICTION, BASE PRESSURE, AND HIGH ANGLE-OF-ATTACK PREDICTION	31
	6.1 SKIN FRICTION	31
	6.2 BODY BASE PRESSURE AXIAL FORCE	33
	6.3 HIGH ANGLE-OF-ATTACK PREDICTION	34
7.0	EVALUATION OF THE NUMERICAL METHODS	37
	7.1 INVISCID POTENTIAL THEORY	37
	7.1.1 Continuous Bodies Alone	37
	7.1.2 Discontinuous Bodies Alone	38
	7.1.3 Configurations With Lifting Surfaces	39
	7.2 HIGH MACH NUMBER PREDICTION	40

CONTENTS (CONTINUED)

Page

7.3 COMPLETE CONFIGURATIONS INCLUDING VISCOUS ESTIMATES 41
7.3.1 High Angle-of-Attack Normal Force and Pitching Moment 41
7.3.2 Axial Forebody and Total Force Prediction 41

8.0 CONCLUDING REMARKS 42

REFERENCES 43

NOMENCLATURE 71

DISTRIBUTION . . . . . (1)

ILLUSTRATIONS

Figure		Page
1	HALF-PLANE BODY GEOMETRY	46
2	THIN FIN GEOMETRY	46
3	FIN PLANFORM GEOMETRY	47
4	CYLINDRICAL, ARC, AND NORMAL COORDINATE SYSTEM ASSOCIATED WITH A DISCONTINUITY WAVEFRONT	47
5	BLUNT BODY GEOMETRY	48
6	WAKE SHADOW GEOMETRY FOR NEWTONIAN CROSSFLOW ESTIMATES	48
7	COMPARISON COMPUTATIONS FOR A $dr_b/dx = \tan(20\ deg)$ $(1-0.5\cos\theta)$ CONE, $M_\infty = 2.0$, $\alpha = 0.0$ DEG, $\beta' = 0.0$ DEG	49
8	COMPARISON COMPUTATIONS; HALF CIRCLE, $dr_b/dx = 0.4$ $(0 < \theta < 90\ deg)$; HALF 2/1 ELLIPSE; $M_\infty = 2$, $\alpha = 0.0$ DEG, $\beta' = 0.0$ DEG	49
9	COMPARISONS FOR A 2/1 ELLIPTICAL CROSS-SECTION BODY, $M_\infty = 1.2$, $\alpha = 2.$ DEG, $\beta' = 0.0$ DEG	50
10	NONSIMILIAR NASA FOREBODY	50
11	a. C_p (0, 180 DEG) AND TOTAL LOAD COMPARISONS FOR FOREBODY 4, $M_\infty = 1.7$, $\alpha = 5.0$ DEG, $\beta' = 5.02$ DEG	51
	b. C_p (90, 270 DEG) COMPARISON FOR FOREBODY 4, $M_\infty = 1.7$, $\alpha = 5.0$ DEG, $\beta' = 5.02$ DEG	51
12	HAACK - ADAMS 3/1 ELLIPTICAL CROSS-SECTION BODY C_N AND C_m COMPARISIONS, $M_\infty = 2$	52
13	COMPARISON OF NASA DATA WITH SWINT AND NANC FOR A BLUNTED CONE, $M_\infty = 1.9$, $\alpha = 8$ DEG, $r_n = 0.175$ CALIBERS, $\delta_c = 11.5$ DEG	52
14	C_p AND $dC_N/d\,(x/D)$ COMPARISONS FOR A CONE-CYLINDER DISCONTINUITY	53

ILLUSTRATIONS (CONTINUED)

Figure		Page
15	C_p AND $dC_N/d(x/D)$ COMPARISONS FOR A CIRCULAR INLET DISCONTINUITY	53
16	INLET-CYLINDER BODY WITH TWO DISCONTINUITIES	54
17	C_p AND AERODYNAMIC COEFFICIENT COMPARISONS FOR AN INLET-CYLINDER BODY, $M_\infty = 1.7$, $\alpha = 5$ DEG, $\beta' = 0$ DEG	54
18	LEADING EDGE JUMPS FOR VARIOUS SWEEP ANGLES, $M_\infty = 2$, $\alpha = 10$ DEG	55
19	BODY-TAIL CONFIGURATIONS IN CALIBER DIMENSIONS	56
20	2/1 ELLIPTICAL CROSS-SECTION BODY CONFIGURATION	56
21	C_N AND C_m COMPARISONS FOR A 2/1 ELLIPTICAL CROSS-SECTION MISSILE, $M_\infty = 1.5$, $\phi = 0$ DEG, $\phi = 50$ DEG	57
22	C_Y AND C_n COMPARISONS FOR A 2/1 ELLIPITICAL CROSS-SECTION MISSILE, $M_\infty = 1.5$, $\phi = 90$ DEG, $\phi = 50$ DEG	57
23	3/1 ELLIPTICAL BWT CONFIGURATION (DIMENSIONS IN BODY LENGTHS)	58
24	C_N AND C_m COMPARISONS FOR A 3/1 ELLIPTICAL CROSS-SECTION BWT CONFIGURATION, $M_\infty = 2.0$	58
25	VARIABLE ELLIPTICAL CROSS-SECTION BODY MISSILE MODEL (DIMENSIONS IN CENTIMETERS)	59
26	C_N AND C_m COMPARISONS FOR A VARIABLE ELLIPTICAL CROSS-SECTION BLUNTED BODY, $M_\infty = 2.5$	60
27	C_N AND C_m FOR A VARIABLE ELLIPTICAL CROSS-SECTION BWT CONFIGURATION, $M_\infty = 2.5$	61
28	C_N COMPARISON FOR A VARIABLE ELLIPTICAL CROSS-SECTION BWT CONFIGURATION, $M_\infty = 2.96$	62
29	C_m COMPARISON FOR A 3/1 ELLIPTICAL CROSS-SECTION BODY CONFIGURATION, $M_\infty = 2.96$	62
30	MONOPLANE-WING ELLIPTIC MISSILE MODEL (DIMENSIONS IN CENTIMETERS)	63
31	C_N AND C_m COMPARISONS FOR A MONOPLANE-WING ELLIPTIC MISSILE MODEL, $M_\infty = 2.86$	64

ILLUSTRATIONS (CONTINUED)

Figure		Page
32	C_N AND C_m COMPARISONS FOR A 3/1 ELLIPTIC MONOPLANE MISSILE MODEL AT HIGH ANGLE OF ATTACK, $M_\infty = 2.0$	64
33	C_N AND C_m COMPARISONS FOR A 3/1 ELLIPTIC MONOPLANAR MISSILE MODEL AT HIGH ANGLE OF ATTACK, $M_\infty = 3.95$	65
34	C_N AND C_m COMPARISONS FOR A 3/1 ELLIPTIC MONOPLANE MISSILE MODEL AT HIGH ANGLE OF ATTACK, $M_\infty = 1.3$	65
35	NASA/LRC TF-4 MISSILE MODEL WITH KING-SIZE TAIL FINS	66
36	C_N AND C_m COMPARISONS FOR THE NASA TF-4, $M_\infty = 2.5$	66
37	FOREBODY AND TOTAL AXIAL FORCE COMPARISONS FOR A 3/1 ELLIPTIC BODY MONOPLANAR MISSILE MODEL, $\alpha = 0$ DEG	67
38	FOREBODY AXIAL FORCE COMPARISON FOR A 3/1 ELLIPTIC BODY MISSILE MODEL, $\alpha = 0$ DEG, $\delta_f = -10$ DEG	67

TABLES

Table		Page
1	LOCAL SOLUTION PREDICTION METHODS	68
2	COMPARISON COMPUTATIONS FOR BODY/FIN 1 CONFIGURATIONS, $M_\infty = 2.0$, $\alpha = 5$ DEG, $x' = 3.0$ CALIBERS FROM NOSE, A_R = CYLINDER CROSS SECTION, L_R = CYLINDER DIAMETER	69
3	SEMI-MAJOR, SEMI-MINOR AXIS VARIATIONS FOR VARIABLE ELLIPTICAL CROSS-SECTION BODIES	70

INTRODUCTION

The need to investigate a large number of free-stream and geometric combinations for preliminary design studies requires rapid/accurate computational models. It is assumed that the flow field computation can be separated into inviscid, boundary layer, crossflow separation, and separated base region computations.

The bulk of the theoretical effort was devoted to developing an inviscid computational model for configurations with nonaxisymmetric bodies that would be valid at low angle of attack. The objective was to develop a code for the free-stream Mach number range of $1.2 \leq M_\infty \leq 3.0$ with an accuracy approaching that of the nonlinear Euler or potential models, but which requires significantly shorter run times.

Linear surface singularity methods [1,2] have been highly developed for complex configurations, including high angle-of-attack vortex modelling. Set up and run times are fairly long. Nonlinear compressibility is not well modelled.

For axisymmetric bodies at low angle of attack, component-buildup methods can be utilized for a restricted range of configurations and free-stream conditions that are applicable to many current designs.[3,4] For nonaxisymmetric bodies with inlets and more general free-stream conditions, the component buildup approach is less applicable.

The Van Dyke second-order potential method [5] was adapted for the body-alone inviscid prediction described in References 3 and 4. The method only requires the evaluation of axial source-sink and doublet distributions that are evaluated as the solution is marched down the body. Extension of the model to nonaxisymmetric bodies requires evaluation of the first-order solution in the flow field. The axisymmetric body solution at angle of attack is not a full second-order solution.

The second-order Van Dyke model has been extensively developed for nonaxisymmetric bodies with planar discontinuities including inlets. [6-8] In this report, extensions to bodies with blunted noses and lifting surfaces are given. The numerical techniques are finite-difference implicit and explicit marching. The current method tracks the origin of disturbances or nose Mach cone. This limits the small disturbance solution to bodies that lie within the Mach cone. The work described here and in References 6-8 required original research that did not exist in the current literature.

At higher Mach numbers, local pressure solution methods [9] are utilized (generally for Mach numbers greater than 3.0). However, for better accuracy, an Euler solution such as given by the SWINT code [10,11] is recommended.

The effects of viscosity (e.g., surface skin friction, crossflow separation at high angles of attack, and base wake flow) are treated by rapid, very approximate methods.

2.0 GEOMETRY, FREE-STREAM VELOCITY, AND FORCE CONVENTIONS

2.1 BODY GEOMETRY

The body is assumed to have a vertical plane of symmetry. For the linearized computations, the body (including fins) must lie within the Mach cone of disturbances. For a blunted body, the origin of the Mach cone begins upstream of the nose. However, body geometry is always referred to the nose.

A half-plane for a general body is depicted in Figure 1. Body geometry is given in cylindrical coordinates and the body radius, r_b, must be single valued in the azimuth angle, θ. For the blunted body shown, the choice of origin of coordinates 0' will be discussed in Section 3.7. The body is assumed to be continuous between planar discontinuities. However, r_b is assumed to be continuous in θ.

An initial blunted section, O to the plane OO, must be circular in cross section. The r_b variation with x need not be that of a circular arc. Typical planar discontinuities are shown for OO, AA, and BB: OO may have a slope discontinuity or a radius of curvature discontinuity; AA depicts a radius or planar inlet discontinuity; and BB depicts a slope discontinuity.

The body is divided into sections equal to the number of planar discontinuities plus one. The body is assumed to be piecewise continuous to second order in x derivatives between planes of discontinuity. No limit to the number of sections is assumed. Any section, except the first, may have a set of fins (up to six fins per set). Each section may be similar or nonsimilar. Similarity implies a basic cross-sectional outline that is scaled. An axisymmetric body is similar throughout.

Each cross section is quarter- or half-plane symmetric and $\partial r_b/\partial\theta$ is assumed to be zero at the ends of the symmetry intervals.

Body geometry is input analytically by code source updates or numerically as planes of r_b vs θ point sets. Each section may have a different mode of body geometry description.

For similar sections, only one reference x plane of r_b, $\partial r_b/\partial\theta$, and $\partial^2 r_b/\partial\theta^2$ need be evaluated for the quarter- or half-plane. For the remaining x locations, r_b, $\partial r_b/\partial x$, and $\partial^2 r_b/\partial x^2$ are required only at the initial computational θ plane. For the numerical mode of input, r_b, $\partial r_b/\partial x$, $\partial^2 r_b/\partial x^2$ are computed using a four-point Lagrange polynominal fit; $\partial r_b/\partial\theta$, $\partial^2 r/\partial\theta^2$, and $\partial^2 r_b/\partial x\partial\theta$ are computed numerically using third-order spline fits.

2.2 FIN GEOMETRY

The fins are treated as thin fins in a manner very close to that described in Reference 10. The fins are assumed to be symmetric about a midplane that lies on a constant θ plane. Figure 2 depicts the sectional view, CC, from Figure 1. Also depicted is an intermediate computational plane and an expanded view of the fin cross section.

Again, symmetry is built into the code. The fin configuration is input as quarter- or half-plane symmetric. Thus, if the body has quarter-plane symmetry and the fin set has half-plane symmetry, the body information is for $0<\theta<\pi/2$ and the fin information is for two fins as shown in Figure 2.

As indicated in Section 2.1, up to six fins per full-plane are allowed. For fin quarter-plane symmetry, only one or two fins are allowed in the interval $0<\theta<\pi/2$. Two fins are allowed if one of the fins lies on either $\theta=0$ or $\theta=\pi/2$ planes.

For fin half-plane symmetry, one to four fins are allowed in the interval $0<\theta<\pi$; four fins are allowed if two of the fins lie on $\theta=0$ and $\theta=\pi$ planes. None of the fins for fin quarter- or half-plane symmetry need to be identical.

The indices i, j, and k refer to a computational grid that is not shown in detail in Figure 2 and will be discussed later in this document. ξ is a shearing transformation

$$\xi = \frac{r - r_b}{x/\beta - r_b} \tag{2-1}$$

that maps the region between the body and the Mach cone to a rectangular region.

The thin-fin assumption implies that the fin surface lies close to the fin midplane. For computational purposes, the fin is assumed to have sharp edges. Fin boundary conditions are evaluated at the midplane. Thus, points A and B coalesce to two computational points on either side of the midplane. The fin plane is located by the index j=JFIN. The θ_f values are obtained from the body input array; $\theta_1, \theta_2, \ldots \theta(j) \ldots, \theta_m = \theta(JM)$; to be discussed later.

From the geometry of Figure 2,

$$\psi = \theta - \theta_f(JFIN) - \sigma \tag{2-2}$$

$$\sigma = tan^{-1}(t/r), \tag{2-3}$$

where ψ, σ, and t are assumed to be small.

All moveable control deflections are treated only as streamwise slopes. For a fin deflection, in reality, leading and trailing edges are displaced out of the original fin plane. The location of the deflected fin hinge line is not an input. Individual fin deflections are input. A positive deflection occurs when the trailing edge of the fin lies clockwise from the fin plane.

A consideration of free-stream conditions, fin symmetry, fin deflections, and body symmetry determines the values of θ_1 and θ_{max} and whether the computation is quarter-, half-, or full-plane. This will be discussed later.

Figure 3 depicts the geometry used to describe a single-fin planform. XMI is the minimum value of x for the fin. XMA is the maximum x distance of the fin from the origin. RMI is the minimum radial distance from the x axis. s+RMI locates the general radial distance of a fin point. SMA+RMI is the maximum radial extent of the fin. All the values in this paragraph are input numerically. With this type of input, the same fin may be positioned any place on the body.

The planform outline, its inclinations, and the fin thickness derivatives are given as analytic functions of s and x. The planform outline is given as inner, SI, and outer, SO, values of s. Currently, the fin surface is assumed to be a continuous surface for most applications. For the high Mach number range, discontinuous fin slopes may be input as is. For the potential flow computation, discontinuous slopes are scaled down; fin axial force is then scaled back up. The scaling is also needed for thick continuous surfaces.

Also shown in Figure 3 are the traces of constant ξ values on the fin. For the high Mach number regime, these traces are based on a pseudo Mach cone that lies outside all fins in the section. The edge where a ξ trace enters the fin is a leading edge. The edge where a ξ trace leaves the fin is a trailing edge. If the trailing edge is subsonic, it is a side edge.

2.3 FREE-STREAM VELOCITY VECTOR

The Cartesian components of the free-stream dimensionless velocity vector are given by

$$q_\infty = \cos\alpha \cos\beta' \, i' + \sin\beta' \, j' + \sin\alpha \cos\beta' \, k' \tag{2-4}$$

2.4 FORCE CONVENTION

The axial force, F_A, acts in the x direction; the normal force, F_N, acts in the z direction; and the side force, F_Y, acts in the negative y direction. The roll moment, M_ℓ, acts in the negative x direction; the yawing moment, M_n, acts in the negative z direction; and the pitching moment, M_m, acts in the negative y direction.

2.5 SYMMETRY CONSIDERATIONS AND NONZERO FORCE COEFFICIENTS

As earlier indicated in Section 2.2, the range of θ and the nonzero force coefficients are determined by the free-stream velocity vector, body geometry symmetry, fin symmetry, and fin deflection. In the coding, the individual force and moments are labled 1 through 6 for axial force, normal force, pitching moment, side force, yawing moment, and roll moment, respectively. There are four possible combinations or modes, LM, of θ range and active force coefficients. The LM value may change from body section to body section and is associated with the highest value of force label. LM is an input variable. LM = 1 is for quarter-plane symmetry for body and fin, $\alpha = 0$, $\beta' = 0$, and mirror image fin deflections about $\theta = \pi/2$. Only the axial force is nonzero. LM = 3 is for vertical half-plane symmetry. It is obtained by various combinations where β' is always zero. Active force labels are 1 through 3. LM = 5 is the upper half-plane symmetry associated with any combination of yaw deflection and/or side slip and body quarter-plane symmetry. Active force labels are 1, 4, and 5 LM = 6 is for the full range of θ and forces. Configuration symmetry may vary from section to section. I M $\geq$ LML, where LML is the previous section value of LM, is required by the hyperbolic character of the flow. Thus, LM may vary from 1 to 3, 1 to 5, 1 to 6, 1 to 3 to 6, 1 to 5 to 6, or 5 to 6 in the downstream direction.

3.0 THEORETICAL DEVELOPMENT FOR THE FIRST- AND SECOND-ORDER POTENTIAL SOLVERS

3.1 FIRST - AND SECOND-ORDER POTENTIAL EQUATIONS

The full nonlinear dimensionless potential equation is given by

$$\left\{1 + \frac{\gamma - 1}{2} M_\infty^2 (1 - Q^2)\right\} \nabla \cdot \; Q = \frac{M_\infty^2}{2} Q \cdot \; \nabla \, (Q^2) \tag{3-1}$$

A small disturbance from the free-stream dimensionless velocity vector is given by

$$Q = q_\infty + q = (\cos\alpha \cos\beta' + u)\, i' + q_{\infty c} + q_c \tag{3-2}$$

where Q is the total velocity vector, q is the disturbance velocity, q_∞ is the free-stream velocity, and $q_{\infty c}$ and q_c are crossflow components of q_∞ and q, respectively.

Substituting Equation (3-2) into (3-1) and neglecting higher-order terms, one obtains the well-known first-order wave equation

$$\nabla_c \cdot\ q_{1c} - \beta^2 \frac{\partial u_1}{\partial x} = 0 \tag{3-3}$$

∇_c is the crossflow gradient operator. The subscript $_1$ indicates first order. Equation (3-3) is supplemented by the two crossflow irrotationality equations.

$$(\nabla \times q_1)_c = 0 \tag{3-4}$$

An improved solution to the first-order problem is obtained by evaluating the neglected nonlinear terms using the first-order solution and solving the nonhomogeneous wave equation for a second-order iterative solution. Second-order equations are

$$\nabla_c \cdot\ q_{2c} - \beta^2 \frac{\partial u_2}{\partial x} = M_\infty^2 \left[\frac{\partial A}{\partial x} + \nabla_c \cdot\ \Omega_c - \frac{M_\infty^2}{\beta^2} \frac{2-\gamma}{2}\, q_{1c}^2\, \nabla_c \cdot\ q_{1c} \right] \tag{3-5}$$

$$(\nabla \times q_2)_c = 0 \tag{3-6}$$

$$A = u_1 \left(\tfrac{1}{2}\, q_1^2 - \frac{2-\gamma}{6} M_\infty^2\, u_1^2 - 1\right)$$

$$+ \cos\alpha \cos\beta' \left[q_1^2 + \frac{\gamma-1}{2} M_\infty^2\, u_1^2 + q_1 \cdot\ q_\infty \right] \tag{3-7}$$

$$\Omega_c = \tfrac{1}{2}\, q_1^2\ q_{1c} + (q_1^2 + q_1 \cdot\ q_\infty)\, q_{\infty c}$$

$$+ \frac{M_\infty^2 (\gamma-1)}{\beta^2} \left[\frac{q_{1c}^2}{2}\, q_{\infty c} + q_{1c} \times (q_{1c} \times q_{\infty c}) \right] \tag{3-8}$$

The subscript 2 refers to the second order. The first- and second-order equations are in nearly conservative general vector form. Only the last term on the right hand side of Equation (3-5) is in non-conservative form.

The boundary condition on all surfaces is

$$Q \cdot\ n = 0 \tag{3-9}$$

where n is the outward normal.

Any set of coordinates may be used for the crossflow plane. An ideal set of body fitted orthogonal coordinates would transform the region between the body, including fins and the bounding Mach cone, to a rectangular computational region. This would require a numerical solution of Laplace's equation. This would lead to a simplified boundary condition evaluation. However, the disturbance envelope Mach cone is circular and, hence, the choice of cylindrical coordinates eliminates the grid generation problem. However, the range of configurations is limited unless one introduces the complex multizone approach of Reference 12.

3.2 COMPUTATIONAL COORDINATES AND GRIDS

The shearing transformation has been introduced in Equation (2-1). The basic variables ξ and θ are further clustered independently for unequally spaced grids.

The θ grid may be uniform or nonuniform; θ points are clustered near points of greatest curvature of the body. It is assumed that the nonuniform grid θ is mapped to the uniform unspecified grid ϕ. For a uniform grid, only the maximum θ, θ_m, compatible with the body symmetry is input and divided equally according to a maximum input, j = JM. For a nonuniform grid, the individual θ computational points are input. Transformed first and second derivatives are evaluated by applying central or one-sided differences in ϕ. Combinations that are needed are

$$\partial/\partial\theta\,(\ ) = \frac{1}{\dfrac{d\theta}{d\phi}}\,\partial/\partial\phi\,(\ ) \approx \frac{C_1}{\dfrac{d\theta}{d\phi}\,\Delta\phi} \tag{3-10}$$

$$\frac{\partial^2}{\partial\theta^2}(\ ) = \frac{1}{\left(\dfrac{d\theta}{d\phi}\right)^2}\left[\frac{\partial^2}{\partial\phi^2} - \frac{d^2\theta}{d\phi^2} \Big/ \frac{d\theta}{d\phi}\,\partial/\partial\phi\right](\ ) \tag{3-11}$$

$$= \frac{1}{\left(\dfrac{d\theta}{d\phi}\,\Delta\phi\right)^2}\left[C_2 - C_1\,\frac{d^2\theta}{d\phi^2}\,(\Delta\phi)^2/\left(\frac{d\theta}{d\phi}\,\Delta\phi\right)\right]$$

The quantities $d\theta/d\phi\,\Delta\phi$ and $d^2\theta/d\phi^2\,(\Delta\phi)^2$ are evaluated by central or one-sided difference approximations of $O[(\Delta\phi)^4]$ accuracy. C_1 and C_2 are related to the finite-difference approximations.

The ξ grid may be uniform as determined by the input KM value or nonuniform; $\xi_1 = \xi(1) = 0$. The nonuniform grid may vary as a geometric progression in which $\xi_2 = \xi(2) = DO$ or may be input individually. ξ clustering is necessary far downstream on long bodies or for small span fins. The geometric progression clustering grid is given as

$$\xi_k = DO \sum_{L=0}^{L=k-2} a^L = \frac{DO\,(1-a^{k-1})}{1-a} \qquad k = 2, 3, \ldots, KM+1 \tag{3-12}$$

a is determined at k = KM + 1 from

$$1 = \frac{DO\,(1-a^{KM})}{1-a} \tag{3-13}$$

a is determined by Newton-Raphson iteration; $a \geq 1$. Once a is determined, Equation (3-12) evaluates the geometric progression distribution. A transformation from ξ to an unspecified uniform ζ grid is applied in a manner similar to that for the θ gridding. First- and second-order derivatives similar to that in Equations (3-10) and (3-11) need to be evaluated. Central and one-sided difference approximations of $0\,[(\nabla\zeta)^4]$ are used.

3.3 VELOCITY ADVANCEMENT EQUATIONS IN ξ,θ COORDINATES

The first- and second-order equations may be recast into an almost conservation form using ξ and θ coordinates.

The first-order equations are

$$\partial/\partial\xi\left\{x\left[R\,(-\beta^2 E_x u_1 + v_1) + E_T w_1\right]\right\} + \partial/\partial\theta\left[x\,(1/\beta - R_b)\,w_1\right] + \partial/\partial x\left[-\beta^2 x^2 R\,(1/\beta - R_b)\,u_1\right] = 0 \tag{3-14}$$

$$\partial/\partial x\left[x\,(1/\beta - R_b)\,v_1\right] + \partial/\partial\xi\left[-u_1 + E_x v_1\right] = 0 \tag{3-15}$$

$$\partial/\partial x\left[x^2 R\,(1/\beta - R_b)\,w_1\right] + \partial/\partial\xi\left\{x\left[R\,E_x w_1 - E_T u_1\right]\right\} - \partial/\partial\theta\left[x\,(1/\beta - R_b)\,u_1\right] = 0 \tag{3-16}$$

Here, $R = r/x$, $R_b = r_b/x$, and

$$E_x = -\left[R + x\frac{\partial R_b}{\partial x}\,(1-\xi)\right]$$

$$E_T = -(1-\xi)\frac{\partial R_b}{\partial\theta}$$

u_1, v_1, and w_1 are cylindrical coordinate velocities.

The second-order equations are of similar form.

$$\begin{aligned}&\partial/\partial x\left[-\beta^2 x^2 R(1/\beta - R_b)\, u_{2e}\right] + \partial/\partial\theta\left[x(1/\beta - R_b)\, w_{2e}\right] \\ &\quad + \partial/\partial\xi\left\{x\left[R(-\beta^2 E_x u_{2e} + v_{2e}) + E_T w_{2e}\right]\right\} \\ &= -q_N\left\{\partial/\partial\xi\left[x(R v_1 + E_T w_1)\right] + \partial/\partial\theta\left[x(1/\beta - R_b) w_1\right]\right\}\end{aligned} \tag{3-17}$$

$$\partial/\partial x\left[x(1/\beta - R_b) v_2\right] + \partial/\partial\xi\left[E_x v_2 - u_2\right] = 0 \tag{3-18}$$

$$\begin{aligned}&\partial/\partial x\left[x^2 R(1/\beta - R_b) w_2\right] + \partial/\partial\xi\left\{x\left[R E_x w_2 - E_T u_2\right]\right\} \\ &\quad - \partial/\partial\theta\left[x(1/\beta - R_b) u_2\right] = 0\end{aligned} \tag{3-19}$$

$$\begin{aligned}q_N &= \frac{M_\infty^4}{\beta^2}(v_1^2 + w_1^2)\frac{(2-\gamma)}{2} \\ u_{2e} &= u_2 + \frac{M_\infty^2}{\beta^2} A \\ v_{2e} &= v_2 - M_\infty^2 q_r \\ w_{2e} &= w_2 - M_\infty^2 q_\theta\end{aligned} \tag{3-20}$$

A is given by Equation (3-7) with

$$\begin{aligned}q_\infty &= \cos\alpha\cos\beta'\, i' + (\sin\alpha\cos\beta'\cos\theta + \sin\beta'\sin\theta)\, j' \\ &\quad + (\sin\beta'\cos\theta - \sin\alpha\cos\beta'\sin\theta)\, k' \\ &= u_\infty i' + v_\infty j' + w_\infty k'\end{aligned} \tag{3-21}$$

i', j', k' are unit vectors for the cylindrical coordinate system.

$$q_r = v_1\frac{q_1^2}{2} + v_\infty(q_\infty \cdot q_1 + q_1^2) + \frac{(\gamma-1)M_\infty^2}{\beta^2}\left[\frac{v_\infty}{2}(v_1^2 - w_1^2) + w_\infty v_1 w_1\right] \tag{3-22}$$

$$q_\theta = \frac{w_1 q_1^2}{2} + w_\infty(q_\infty \cdot q_1 + q_1^2) + \frac{\gamma-1}{\beta^2}M_\infty^2\left[-\frac{w_\infty}{2}(v_1^2 - w_1^2) + v_\infty v_1 w_1\right] \tag{3-23}$$

The equations in this section will be utilized to advance the field velocities by an explicit marching scheme to be discussed later.

3.4 IMPLICIT MARCHING SOLUTION

An implicit marching solution is used for continuous pointed bodies with no lifting surfaces and for the initial section of pointed bodies. The velocity vectors q_1, q_2 are replaced by the gradient of a potential

$$q_\ell = \nabla \phi_\ell \qquad \ell = 1,2 \tag{3-24}$$

A similar conical potential function is introduced as

$$\phi_\ell = x F_\ell(x, \xi, \theta) \tag{3-25}$$

The full first- or second-order boundary condition is given as

$$V_\ell = \frac{\partial r_b}{\partial x} U_\ell + \frac{1}{R_b} \frac{\partial R_b}{\partial \theta} W_\ell \tag{3-26}$$

U, V, W are total cylindrical coordinate velocities.

Equations (3-14) and (3-17) may be written in nonconservative form after substitution of Equations (3-24) and (3-25) as

$$C_1 (F_{\xi\xi})_\ell + C_2 (F_\xi)_\ell + C_3 (F_\theta)_\ell + C_4 (F_{\xi\theta})_\ell + C_5 x (F_{\xi x})_\ell + 2 C_6 x (F_x)_\ell + C_6 x^2 (F_{xx})_\ell = (RHS)_\ell \qquad \ell = 1,2$$

$$(RHS)_1 = 0.0 \tag{3-27}$$

The boundary conditions may be written as

$$(F_\xi)_\ell = B_1 + B_2 F_\ell + B_3 (F_\theta)_\ell + B_2 x (F_x)_\ell \tag{3-28}$$

Equations (3-27) and (3-28) could be written in ϕ, ζ variables as well.

At the Mach cone, the conical potential functions are known to be singular and assumed to behave as

$$F_1 = (1-\xi)^{3/2} \left[S_{11} + S_{12} (\xi - \xi_{KM}) \right] \tag{3-29}$$

$$F_2 = S_{21} (1-\xi) + S_{22} (1-\xi)^{3/2} \tag{3-30}$$

Second-order accurate difference schemes are the goal. For k = 2, KM-1, central difference approximations are utilized for all ζ derivatives. Central differences are utilized for all ϕ derivatives as well. At symmetry planes, F_θ and $F_{\xi\theta}$ are set to zero. At k = KM, ξ derivatives are obtained by differentiating

Equations (3-29) and (3-30). S_{11}, S_{12}, S_{21}, and S_{22} are computed by evaluating Equations (3-29) and (3-30) at k = KM and k = KM-1.

Only one previous plane of data is needed in evaluating the x derivatives. From a Taylor's series expansion about a known plane of data,

$$F_\ell = F_{\ell,i} + (F_x)_{\ell,i}\Delta x' + \frac{(F_{xx})_{\ell,i}(\Delta x')^2}{2} \tag{3-31}$$

It is assumed that F_{xx} is constant for the interval Δx. Here, $\Delta x' = x - x_i$.

$$(F_{xx})_{\ell,i+1} = (F_{xx})_{\ell,i} = \frac{2}{(\Delta x)^2}\left[F_{\ell,i+1} - F_{\ell,i}\right] - \frac{2(F_x)_{\ell,i}}{\Delta x} \tag{3-32}$$

Differentiating Equation (3-31) and substituting Equation (3-32) yields

$$(F_x)_{\ell,i+1} = -(F_x)_{\ell,i} + \frac{2}{\Delta x}\left[F_{\ell,i+1} - F_{\ell,i}\right] \tag{3-33}$$

$(F_x)_\ell$ and F_ℓ are stored at i, x_i. The solution is desired at i + 1, $x_i + \Delta x$. These x derivatives then may be substituted into Equations (3-27) and (3-28). At the initial plane, $(F_x)_{\ell,1}$ and $(F_{xx})_{\ell,1}$ are set to zero. At x = 0, the flow is conically similar. The advantage of an implicit scheme is that the initial plane of data is established immediately and large steps, Δx, may be taken.

At k = 1, the potential equations are evaluated with the aid of the boundary equations. $F_{\xi x}$ is obtained by differentiating Equation (3-28) with respect to x. Initially, $F_{\xi\theta}$ was evaluated by differentiating Equation (3-28) with respect to θ. A more stable approximation proved to be

$$(F_{\xi\theta})_{1,j} = \frac{1}{2\left(\frac{d\theta}{d\phi}\right)_{1,j}\Delta\phi}\left[F_{2,j+1} - F_{2,j-1} - F_{1,j+1} + F_{1,j-1}\right] \tag{3-34}$$

$F_{\xi\xi}$ is evaluted as

$$(F_{\xi\xi})_{1,j} = \frac{2x}{(\Delta\xi)^2}\left[F_{2,j} - F_{1,j} - (F_\xi)_{1,j}\right] \tag{3-35}$$

The resultant finite-difference scheme leads to a block tridiagonal matrix equation for $(F_1)_{i+1}$ and $(F_2)_{i+1}$. Each block is tridiagonal for quarter- or half-plane symmetry. For a full 360-deg solution, additional wrap-around terms are present for each block. Solution of the matrix equations is obtained by lower-upper decomposition involving the block matrices (see Reference 7 for details). Velocities are obtained from the definition of the potential and conical potential function combined with boundary condition and finite-difference approximations (see Reference 6 for details of the velocity relationships). Velocities are evaluated only at the boundary except where a transition from an implicit solver to the explicit solver is required.

3.5 PLANAR BODY DISCONTINUITY JUMP CONDITIONS

At the discontinuity, locally two-dimensional jump relations are sought that are compatible with the first- and second-order differential equations. Since the discontinuity is planar, disturbances are propagated into the flow along a surface that is the envelope of the Mach cones emanating from the surface cut curve just downstream of the discontinuity.

Figure 4 depicts a cylindrical coordinate system and the s, n coordinate system associated with the discontinuity cut curve; s is along the curve and n is normal to it. The wave front grows in the n direction. Jumps occur across the normal to the wave front. Velocity components tangential to the wave surface are conserved. The discontinuity surface is not tracked into the flow.

First-order equations in s, n, x coordinates are given as

$$\frac{1}{1+\kappa n}\frac{\partial v_{s1}}{\partial s}+\frac{1}{1+\kappa n}\,\partial/\partial n\left[v_{n1}(1+\kappa n)\right]-\beta^2\frac{\partial u_1}{\partial x}=0$$

$$\frac{\partial v_{n1}}{\partial x}-\frac{\partial u_1}{\partial n}=0$$

$$\partial/\partial x\left[(1+\kappa n)\,v_{s1}\right]-\frac{\partial u_1}{\partial s}=0 \tag{3-36}$$

Here, κ, is the cut curve curvature. v_{n1} and v_{s1} are normal and arc velocity components. Jump relations are established by an application of Gauss's theorem for the s, n, x system on either side of the as yet undetermined discontinuity surface. This approach is known as the method of "weak solutions"[13]. Applying the method of "weak solutions" to the set of Equation (3-36) yields

$$\Delta v_{s1}e_s+\Delta v_{n1}e_n-\beta^2\Delta u_1 e_x=0 \tag{3-37}$$

$$\Delta v_{n1}e_x-\Delta u_1 e_n=0 \tag{3-38}$$

$$\Delta v_{si}e_x-\Delta u_1 e_s=0 \tag{3-39}$$

e_n, e_s, e_x are components of the surface normal. Since $\Delta v_{s1}=0$, $e_s=0$.

From Equations (3-37) and (3-38),

$$e_n/e_x=-\beta \tag{3-40}$$

$$\Delta v_{n1}+\beta\Delta u_1=0 \tag{3-41}$$

Here, $\Delta(\ )=(\ )$ after $-(\ )$ before $=(\ )a-(\ )b$. Equation (3-40) is the well-known result that the discontinuity surface coincides with the characteristic surface for linear sets of equations.

From the geometry of Figure 4 and $\Delta v_{s1}=0$, one obtains,

$$\Delta v_{s1} = \Delta w_1 \cos\theta' + \Delta v_1 \sin\theta' = 0 \tag{3-42}$$

$$\Delta v_{n1} = \Delta v_1 / \cos\theta' \tag{3-43}$$

The boundary condition on the downstream surface is

$$V_{1b} + \Delta v_1 = \frac{\partial r_b}{\partial x}\left[(1-B)u_\infty + B(U_{1b} + \Delta u_1)\right] + \tan\theta'(W_{1b} + \Delta w_1) \tag{3-44}$$

where

$$\tan\theta' = \frac{1}{R_b}\frac{\partial R_b}{\partial \theta} \tag{3-45}$$

Equations (3-41) through (3-45) lead to a solution for Δu_1, Δv_1, Δw_1. The factor B allows for application of the modified, B = 0, or full, B = 1, boundary conditions. Van Dyke [14] showed that B = 1 is best for surfaces with positive inclination jumps in slope and B = 0 is best for surfaces inclined at large negative angles.

Applying the same approach to the second-order equation leads to

$$\Delta v_{n2} e_n - \beta^2 \Delta u_2 e_x = \beta^2 \Delta u' e_x + \Delta v_n' e_n \tag{3-46}$$

$$\Delta v_{n2} e_x - \Delta u_2 e_n = 0 \tag{3-47}$$

$$\Delta v_{s2} = 0 \tag{3-48}$$

$$\Delta u' = \frac{M_\infty^2}{\beta^2}\Delta A \tag{3-49}$$

$$\frac{v_n'}{M_\infty^2} = v_{n1}\frac{q_1^2}{2} + v_{n\infty}(q_1^2 + q_\infty \cdot q_1) + \frac{M_\infty^2}{\beta^2}(\gamma-1)\left[\frac{v_{n1}^2}{2}v_{n\infty} + v_{s1}v_{s\infty}v_{n1}\right] - \frac{M_\infty^4}{\beta^2}\frac{(2-\gamma)}{2}\left[\frac{v_{n1}^3}{3} + v_{s1}^2 v_{n1}\right] \tag{3-50}$$

Here, $\Delta v_{s1} = 0$ has been used in deriving Equation (3-50). Also,

$$v_{n\infty} = v_\infty \cos\theta' - w_\infty \sin\theta' \tag{3-51}$$

$$v_{s\infty} = w_\infty \cos\theta' + v_\infty \sin\theta' \tag{3-52}$$

Equations (3-46) and (3-47) combined may be written as

$$e_n/e_x = -\beta + \frac{(\Delta v_{n2} + \beta \Delta u_2)}{\Delta u_2} \tag{3-53}$$

$$\Delta v_{n2} + \beta \Delta u_2 = \frac{(\beta^2 \Delta u' + \Delta v'_n e_n/e_x)}{e_n/e_x - \beta} \tag{3-54}$$

If e_n/e_x is set equal to the first-order value of $-\beta$ in Equation (3-54), one obtains

$$\Delta v_{n2} + \beta \Delta u_2 = -\beta \frac{\Delta u'}{2} + \frac{\Delta v'_n}{2} \tag{3-55}$$

Equation (3-55) leads to a set of linear relations for Δu_2, Δv_2, and Δw_2 and is compatible with Van Dyke's[5] jump relations for the second-order axisymmetric case. An alternate approach is to combine Equations (3-53) and (3-54), which leads to a quadratic relationship

$$\Delta v_{n2}^2 - \Delta v_{n2} \Delta v'_n - \beta^2 \left[(\Delta u_2)^2 + \Delta u_2 \Delta u' \right] = 0 \tag{3-56}$$

Equations (3-55) or (3-56) combined with $\Delta v_{s2} = 0$, $\Delta v_{n2} = \Delta v_2/\cos\theta'$, and the second-order downstream boundary condition lead to a solution for Δu_2, Δv_2, and Δw_2. The second-order boundary condition is given by

$$V_{2b} + \Delta v_2 = \frac{\partial r_b}{\partial x} \left[(1-B) U_{1a} + B (U_{2b} + \Delta u_2) \right] + \tan\theta' (W_{2b} + \Delta w_2) \tag{3-57}$$

Choice of sign for the nonlinear quadratic solution depends on whether the local turning angle is compressive or expansive.

The turning angle in the n, x plane for the second-order case is

$$DTH = \tan^{-1} \left[\left(\frac{\partial r_b}{\partial x} \right)_a \cos\theta' \right] - \tan^{-1} \left[\frac{V_{2b} \cos\theta' - W_{2b} \sin\theta'}{U_{2b}} \right] \tag{3-57a}$$

Note that the only difference in applying the jump relations for surface slope discontinuities and inlets is that the upstream velocity vector at the inlet lip must first be determined by interpolation in the upstream velocity field. To continue marching downstream of the inlet, the entire velocity field between the lip and the Mach cone from the origin must be determined by interpolation.

Numerical solution without special damping or tracking of flow discontinuities becomes difficult downstream of a discontinuity. An explicit MacCormack marching scheme was developed in the hope that the internal propagation of discontinuities would be captured.

3.6 EXPLICIT MARCHING SOLUTION OVER CONTINUOUS BODY SECTIONS

Equations (3-14) through (3-19) may be used to advance the field velocities. Characteristic-compatibility relations will be combined here with the boundary condition[15] to advance the boundary velocity components.

The basic equations for combined first- and second-order may be written as

$$u_x + u_\xi \xi_x - \frac{1}{\beta^2}\left[v_\xi \xi_r + \frac{1}{r} w_\xi \xi_\theta\right] = R_u \tag{3-58}$$

$$v_x + v_\xi \xi_x - u_\xi \xi_r = 0 \tag{3-59}$$

$$w_x + w_\xi \xi_x - \frac{1}{r} u_\xi \xi_\theta = u_\theta / r \tag{3-60}$$

$$\begin{aligned} R_u = {} & \frac{v}{r\beta^2} + \frac{1}{r\beta^2}\frac{\partial w}{\partial \theta} - \frac{M_\infty^2}{\beta^2}\left\{\frac{\partial A}{\partial x} + \xi_x \frac{\partial A}{\partial \xi}\right. \\ & + \frac{1}{r}\xi_r \partial/\partial_\xi (r q_r) + \left[\frac{1}{r}\partial/\partial\, 0 + \frac{1}{r}\xi_\theta \partial/\partial \xi\right] q_\theta \Big\} \\ & + \frac{q_N}{\beta^2}\left\{\frac{1}{r}\xi_r \partial/\partial_\xi (r v_1) + \left[\frac{1}{r}\partial/\partial\theta + \frac{1}{r}\xi_\theta \partial/\partial \xi\right] w_1\right\} \end{aligned} \tag{3-61}$$

Here, ξ_r, ξ_x, and ξ_θ are transformation partial derivatives.

Characteristic eigenvalues and eigenvectors are sought for the ξ, x plane with θ as an interior variable.

The set of Equations (3-58) through (3-60) are of the form

$$P_x + R P_\xi = RH \tag{3-62}$$

The eigenvalues and eigenvectors are given by

$$L^i \left[R - \lambda_i I\right] = 0 \qquad i = 1,2 \tag{3-63}$$

$$R = \begin{bmatrix} \xi_x & \dfrac{-\xi_r}{\beta^2} & -\dfrac{1}{\beta^2 r}\xi_\theta \\ -\xi_r & \xi_x & 0 \\ -\dfrac{1}{r}\xi_\theta & 0 & \xi_x \end{bmatrix} \tag{3-64}$$

Solving for the eigenvalues from Equation (3-63),

$$\lambda_1 = \xi_x - \frac{1}{\beta}\left(\xi_r^{\,2} + \frac{1}{r^2}\xi_\theta^{\,2}\right)^{1/2}, \lambda_2 = \xi_x \tag{3-65}$$

The choice of sign for λ_1 is associated with the incoming characteristic that is of interest. Corresponding left eigenvectors are

$$L_1^1 = \frac{\beta r\left[\xi_r^{\,2} + \left(\frac{1}{r}\xi_\theta\right)^2\right]^{1/2}}{\xi_\theta}, L_2^1 = \frac{r\xi_r}{\xi_\theta}, L_3^1 = 1 \tag{3-66}$$

$$L_1^2 = 0, L_2^2 = \frac{-\xi_\theta}{r\xi_r}, L_3^2 = 1 \tag{3-67}$$

Multiplying Equation (3-62) by the left eigenvectors and utilizing Equation (3-63), one obtains two compatibility equations.

$$L^i P_x + \lambda_i L^i P_\xi = L^i R H \tag{3-68}$$

The second compatibility advancement equation of (3-68) may be simplified by utilizing the third unused irrotationality component.

$$\frac{\partial v}{\partial \theta} = \partial/\partial r\,(wr) \tag{3-69}$$

This eliminates the r or ξ dependence. For computational applications, Equation (3-68) is evaluated at the surface.

The first-order compatibility equations are of the form

$$\frac{\partial E_{1i}}{\partial x} + \frac{\partial G_{1i}}{\partial \xi} + \frac{\partial H_{1i}}{\partial \theta} = C_{1i} \quad i = 1,2 \tag{3-70}$$

$$E_{11} = \frac{v_{n1} + \beta u_1}{\cos\theta'} \tag{3-71}$$

$$E_{12} = c_1 v_{s1}, c_1 = x R_b/\cos\theta' \tag{3-72}$$

$$G_{11} = -c_2 E_{11}, c_2 = \left(\frac{\partial r_b}{\partial x} + c_3\right) c_4 \tag{3-73}$$

$$c_3 = \frac{1}{\beta\cos\theta'}, c_4 = \frac{1}{x(1/\beta - R_b)}, G_{12} = 0 \tag{3-74}$$

$$H_{11} = (\tan\theta'\ u_1 - c_3 w_1)c_5,\ c_5 = \frac{1}{xR_b} \tag{3-75}$$

$$H_{12} = -u_1 - \frac{\partial r_b}{\partial x} v_1 \tag{3-76}$$

$$C_{12}=0,\ C_{11}=c_6(c_7 u_1 - w_1)+c_5(c_8 u_1+c_3 v_1-c_9 w_1),\ c_6=\frac{\partial \tan\theta'}{\partial x},\ c_7=\beta \sin\theta', \tag{3-77}$$
$$c_8=\frac{\partial \tan\theta'}{\partial\theta}-\left(\tan\theta'\right)^2,\ c_9=\frac{\sin\theta'}{\beta}\left(\frac{\partial \tan\theta'}{\partial\theta}-\frac{\partial \tan\theta'}{\partial\theta'}\right)$$

Here, θ', v_{si}, and v_{n1} have been defined earlier in connection with the jump conditions.

The second-order compatibility equations are

$$\frac{\partial E_{2i}}{\partial x}+\frac{\partial G_{2i}}{\partial \xi}+\frac{\partial H_{2i}}{\partial\theta}=C_{2i}+q_N\left(\frac{\partial S}{\partial \xi}+\frac{\partial T}{\partial\theta}\right)\ i=1,2 \tag{3-78}$$

$$E_{21}=\frac{v_{n2}+\beta u_{2e}}{\cos\theta'} \tag{3-79}$$

$$E_{22}=c_1 v_{s2} \tag{3-80}$$

$$G_{21}=-c_2 E'_{21}-c_{10}M_\infty^2\left(A\frac{\partial r_b}{\partial x}-q_r\frac{R}{R_b}+\tan\theta' q_\theta\right),\ c_{10}=c_3 c_4,\ G_{22}=0.0 \tag{3-81}$$

$$E'_{21}=(v_{n2}+\beta u_2)/\cos\theta',\ H_{21}=c_5(\tan\theta'\ u_2-c_3 w_{2e}) \tag{3-82}$$

$$H_{22}=-u_2-\frac{\partial r_b}{\partial x}v_2 \tag{3-83}$$

$$S=c_{10}\left(\frac{R}{R_b}v_1-\tan\theta' w_1\right) \tag{3-84}$$

$$T=c_3 c_5 w_1 \tag{3-85}$$

$$C_{22}=0,\ C_{21}=c_6(c_7 u_{2e}-w_2)+c_5\left[c_8 u_2+c_3 v_2-c_9(w_{2e}+q_N w_1)\right] \tag{3-86}$$

Equations (3-14) through (3-19) are already in a form similar to Equations (3-70) and (3-78).

Finite-difference schemes will be developed after the fin boundary scheme is developed.

3.7 BLUNT BODY SOLUTION

As earlier indicated in the geometry description, a blunt body is assumed to have an initial circular cross section; however, the meridian curve need not be a circular arc segment. At the nose of the body, the slope angle is 90 deg and is larger than the Mach cone angle. Sharp nose bodies with initial angles greater than the Mach angle are not considered.

The basic idea is to start the surface pressure distribution as a modified Newtonian one and continue the computation by some approximate model. This approach was first utilized in Reference 16 for relatively large supersonic Mach numbers. The second-order shock expansion method[17] was utilized to continue the computation.

Two different methods of matching a Van Dyke second-order axisymmetric solution with a Newtonian pressure distribution are described in References 3, 18, and 19. Both of these methods use surface boundary conditions, axial source, sinks, and doublets.

The first thing to establish is the effective origin of disturbances and a match point between a modified Newtonian pressure distribution and a continuing potential solution. In Figure 5, a meridian plane and the choice of match point and origin is shown. A match point at $x = x_m$ is chosen so that

$$\tan \delta_m = \left(\frac{\partial r_b}{\partial x} \right)_m = a/\beta, \; a \leq 0.95 \tag{3-87}$$

where $a \leq 0.95$ is an input. x_m is determined by Newton-Raphson iteration.

A tangent from m is drawn to OT. A Mach line is drawn from m to OU. The effective origin is at 0′, $x = x_o \leq 0.0$.

$$x_o = x_m - r_b(x_m) \left[\frac{1-c}{\dfrac{\partial r_b}{\partial x}(x_m)} + c\beta \right] \tag{3-88}$$

where c is an input. Various combinations of a and c have been tried. $a = 0.8$, $c = 0$ seems to be about optimum.

Various approaches were tried for a model blunted cone problem. None of them were fully successful.

The modified Newtonian pressure coefficient distribution is given by

$$C_p = \frac{p - p_\infty}{\gamma/2 \, M_\infty^2} = C_{po} \sin^2 \delta_e \tag{3-89}$$

$$\begin{aligned} \sin \delta_e &= q_\infty \cdot n_{in} \\ &= \cos \alpha_T \sin \delta_m - \sin \alpha_T \cos(\theta - v) \cos \delta_m \end{aligned} \tag{3-90}$$

n_{in} is the inward normal to the body. C_{po} is the stagnation pressure coefficient. α_T is the total angle of attack, and v is the roll angle of the crossflow free-stream velocity component.

The first- and second-order potential functions are given by

$$\phi_1 = f_o(x, r) + f_1(x, r)\cos(\theta - v)\sin\alpha_T \tag{3-91}$$

$$\phi_2 = \chi_o(x, r) + f_1(x, r)\cos(\theta - v)\sin\alpha_T \tag{3-92}$$

This is the "hybrid" approximation of References 5 and 19.

The potential Bernoulli pressure coefficient is given by

$$C_p = \frac{\left[1 + \frac{\gamma - 1}{2} M_\infty^2 (1 - Q^2)\right]^{\gamma/(\gamma-1)} - 1}{\gamma/2\, M_\infty^2} \tag{3-93}$$

Equation (3-92) may be substituted into Equation (3-93) and Equation (3-90) into Equation (3-89) and matched to 0 ($\sin^3\alpha_T$) as in Reference 19. Matching coefficients yields χ_{ox}, χ_{or}, f_1, f_{1x}, and f_{1r} at the surface.

It is then assumed that the ratio of first- to second-order surface velocities at zero angle of attack is the same as the conical solution ratio. This yields an approximation for f_{ox} and f_{or} at the surface.

The remainder of the initial plane of data is obtained by utilizing the homogeneous conical potential functions for f_{ox}, f_{or}, f_{1x}, f_{1r}, and f_1.

In summary, an approximate initial plane of velocity data is obtained that matches the modified Newtonian pressure distribution. The solution is then marched downstream by an explicit routine. Implicit routines lead to strongly oscillating flow prediction.

The blunt body option should only be used for significantly blunted bodies that have large wave drags, since the CFL step size (to be treated later) is very small for almost pointed bodies.

3.8 FIN EDGE TREATMENT AND SURFACE DISCONTINUITIES

The first objective is to obtain jump conditions for supersonic leading and trailing edges. For a fin leading edge, the velocity ahead of the edge is known and the velocity on both edge sides is to be determined. For a variable sweep leading edge, the envelope of disturbances or wavefront from the edge is rotated with respect to the local θ plane of the lifting surface.

Conservation relations for the first-order wave equation may again be derived by the method of "weak solutions".

$$(\Delta w_1)^2 + (\Delta v_1)^2 - \beta^2 (\Delta u_1)^2 = 0 \tag{3-94}$$

Here, the conservation jump relations for the three marching equations have been combined.

At $k = 1$, the remaining relationships are determined by satisfying both the body and fin boundary conditions where the fin meets the body or the beginning of the corner. At $k \neq 1$, the conservation of the tangential velocity component and the fin boundary condition provides the needed two relations for closure.

At the fin surface (from Figure 2),

$$\psi = \theta - \theta_f - \sigma = 0 \tag{3-95}$$

Equation (3-95) may be used to determine the fin surface normal. The fin full boundary condition may be written as

$$W_1 = r\sigma_x U_1 + r\sigma_r V_1 \tag{3-96}$$

$$r\sigma_x = r\partial/\partial x \left[tan^{-1}(t/r) \right] = \frac{t_x}{1+(t/r)^2}$$

$$\approx t_x = tan\,\delta_f \pm t_{ox}$$

$$r\sigma_r = \frac{t_r - t/r}{1+(t/r)^2} \approx t_r - t/r \tag{3-97}$$

Here δ_f is the fin control deflection, t_{ox} is the fin slope; (+) for $\theta > \theta_f$ and (−) for $\theta < \theta_f$ sides of the fin.

The fin boundary condition is further approximated by neglecting the spanwise contribution.

$$W_{1b} + \Delta w_1 = t_x \left[(1-F)u_\infty + F(U_{1b} + \Delta u_1) \right] \tag{3-98}$$

In almost all applications, F = 0 or the approximate fin boundary condition yields a result superior to that for F = 1.

For $k \neq 1$, the tangential velocity may be written as

$$V_t = sin\,\lambda \left[U cos\,\delta_f + W sin\,\delta_f \right] + V cos\,\lambda \tag{3-99}$$

where λ is the local sweepback angle. Applying conservation of the tangential velocity component yields

$$\Delta v_1 = - tan\,\lambda\,(\Delta u_1 cos\,\delta_f + \Delta w_1 sin\,\delta_f) \tag{3-100}$$

In all cases, a quadratic equation must be solved for the jump velocities. Choice of sign is determined by the turning angle being compressive or expansive.

The case for $k \neq 1$, constant λ, $U_{1b} = 1$, $W_{1b} = -\sin\alpha$, $\delta_f = 0$, $t_{ox} = 0$ may be readily solved and is illustrative.

$$\Delta u_1 = \mp \frac{sin\,\alpha}{(\beta^2 - tan^2\lambda)^{1/2}} \tag{3-101}$$

This is the well-known result for the constant supersonic region for a thin wing due to Ackeret. The solution indicates that as λ increases, the jumps in velocity gets very large and that small disturbance theory is violated locally. The subsonic leading edge case, for which conservation relations do not exist, occurs when $\tan \lambda > \beta$. Such singularities do not arise for the full nonlinear potential equations.

A maximum sine of the sweepback angle, $\sin \lambda_m$, is defined by requiring that the Mach wave angle be swept back at least λ_0 from the leading edge.

$$\sin \lambda_m = (-\sin \lambda_o + \beta \cos \lambda_o)/M_\infty \tag{3-102}$$

where $\sin \lambda_0$ is a code input. For $\lambda > \lambda_m$, a subsonic leading edge heuristic treatment is used.

In order to evaluate the nonconservative gradient jump contributions, it is assumed that the local wave front orientation for the second-order is the same as for the first-order case.

The wave front angle, ε, is defined clockwise from the fin plane. On a wave front, the tangential component of velocity is conserved in the local r, θ plane, which yields

$$\tan \varepsilon = \frac{-\Delta v_1}{\Delta w_1} \tag{3-103}$$

For the case of Equation (3-101),

$$\tan \varepsilon = \mp \frac{\tan \lambda}{(\beta^2 - \tan^2 \lambda)^{1/2}}, \sin \varepsilon = \mp \frac{\tan \lambda}{\beta} \tag{3-104}$$

This is also a well-known result from conical flow theory of a flat plate swept wing.

A second-order application of the method of "weak solutions" and Equation (3-103) yields

$$(\Delta w_2)^2 + (\Delta v_2)^2 - \beta^2 (\Delta u_2)^2 = \beta^2 \Delta u' \Delta u_2 + \Delta v' \Delta v_2 + \Delta w' \Delta w_2 \tag{3-105}$$

$$\Delta u' = \frac{M_\infty^2}{\beta^2} \Delta A \tag{3-106}$$

$$\frac{\Delta v'}{M_\infty^2} = \Delta q_r - \frac{2-\gamma}{2} \frac{M_\infty^4}{\beta^2} \Delta \bar{v} \tag{3-107}$$

$$\frac{\Delta w'}{M_\infty^2} = \Delta q_\theta - \frac{2-\gamma}{2} \frac{M_\infty^2}{\beta^2} \Delta \bar{w} \tag{3-108}$$

$$\Delta \bar{v} = \frac{1}{3}\Delta(v_1^3) + \Delta(w_1^2 v_1) + 2/3\ tan\,\varepsilon\,\Delta(w_1^3) - (v_{1b} + w_{1b}\,tan\,\varepsilon)\,\Delta(w_1^2) \tag{3-109}$$

$$\Delta \bar{w} = \frac{1}{3}\Delta(w_1^3) + \Delta(v_1^2 w_1) + 2/3\ cot\,\varepsilon\,\Delta(v_1^3) - (w_{1b} + v_{1b}\,cot\,\varepsilon)\,\Delta(v_1^2) \tag{3-110}$$

Closure equations comparable to (3-98) and (3-100) are

$$W_{2b} + \Delta w_2 = t_x \left[(1-F)\,U_{1a} + F(U_{2b} + \Delta u_2) \right]$$

$$\Delta v_2 = -tan\,\lambda \left[\Delta u_2 \cos\delta_f + \Delta w_2 \sin\delta_f \right] \tag{3-111}$$

The supersonic trailing edge requires different treatment. Here, the flow goes from upper and lower surfaces to the free stream. A formal full analysis would require an iterative solution for the flow turning angle. In many cases, no solution would be possible. The simplest approach is to assume that the downstream velocity vector lies in the plane of the fin. This is the same as $t_x = 0$.

At the trailing edge, there is a velocity and pressure jump on both sides of the arbitrary wake cut (the fin plane). The resultant pressure coefficients and v component of velocity are averaged across the wake. At the corner, the v velocity component is not averaged and the body boundary condition is used.

Turning angle for the corner at $k = 1$ is

$$DTH = -sin^{-1}\left\{ \left[-t_{ox} U_{2b} \pm (-tan\,\delta_f U_{2b} + W_{2b}) \right] / \left[|Q_b| (1 + t_x^2)^{1/2} \right] \right\} \tag{3-112}$$

Turning angle away from the corner for $k \neq 1$ is

$$DTH = -sin^{-1}\left\{ \left[-t_{ox} (U_{2b} - V_t) \pm (-tan\,\delta_f U_{2b} + W_{2b}) \right] / \left[(Q_b^2 - V_t^2)(1 + t_x^2) \right]^{1/2} \right\} \tag{3-113}$$

Equation (3-101) illustrates the problem for subsonic leading edges or edges that are slightly supersonic. The quadratic solution for the velocity jump is imaginary or very large. For a delta wing in a free stream, the first-order conical solution due to Busemann is well known. The pressure coefficient has a square root singularity near the leading edge. The subsonic leading edge pressure distribution is assumed to behave like

$$C_{pk} = \frac{A_k}{(\xi_o^2 - \xi_k^2)^{1/2}},\ k \neq 1 \tag{3-114}$$

Here, ξ_o is the value of ξ at the leading edge and ξ_k is the value of ξ at a point near the leading edge. Inner edges are always assumed to be supersonic. The root point, $k = 1$, is always supersonic. A_k is evaluated by setting

$$C_{pk} = (C_p)_{k-1} \tag{3-115}$$

Alternates to the expression (3-115) were tried, but proved to be somewhat less successful. One of these alternatives was the mean value relationship.

$$\int_{\xi_{KI}}^{\xi_{(k-1)}} C_p \, d_\xi = \int_{\xi_{KI}}^{\xi_{(k-1)}} \frac{A_k}{(\xi_o^2 - \xi^2)^{1/2}} \, d\xi \tag{3-116}$$

Here, KI is the value of k near the inner edge.

The above relations hold for first- or second-order and either side of the fin.

Closure conditions for the subsonic edge were given by the requirement that the velocity vector component parallel to the edge is conserved and the downstream boundary condition is satisfied. The former requirement is given by Equation (3-99).

The boundary conditions are to first- and second-order:

$$W_1 = t_x \left[(1-F) u_\infty + F U_1 \right]$$

$$W_2 = t_x \left[(1-F) U_1 + F U_2 \right] \tag{3-117}$$

The velocity vector squared is determined from the value of C_{pk}

$$U^2 + V^2 + W^2 = 1 - \left\{ \frac{\left[\frac{C_{pk} \gamma M_\infty^2}{2} + 1 \right]^{\frac{\gamma-1}{\gamma}} - 1}{\frac{\gamma-1}{2} M_\infty^2} \right\} \tag{3-118}$$

At a subsonic side edge, it is assumed that the value of the velocities just leaving the edge are equal to value at next k point out; i.e., $u_{1k} = (u_1)_{k+1}$, etc.

3.9 FIN SURFACE ADVANCEMENT EQUATIONS

Characteristic compatibility relations for the fin advancement equations are sought for the ψ, x plane with ξ as an interior variable at $\psi = 0$.

Starting equations for first- and second-order combined are

$$u_x - u_\psi \sigma_x + \frac{1}{\beta^2}\sigma_r v_\psi - \frac{1}{r\beta^2} w_\psi = \frac{1}{\beta^2}\left[v/r + v_\xi \xi_r + \frac{1}{r} w_\xi \xi_\theta\right] - \frac{M_\infty^2}{\beta^2}\left\{\frac{\partial A}{\partial x} + \xi_x \frac{\partial A}{\partial \xi}\right.$$

$$-\sigma_x \frac{\partial A}{\partial \psi} + \frac{1}{r}\left[\partial/\partial\xi\,(rq_r)\,\xi_r - \sigma_r\,\partial/\partial\psi\,(r q_r) + \frac{1}{r}\left[\xi_\theta \frac{\partial q_\theta}{\partial \xi} + \frac{\partial q_\theta}{\partial \psi}\right]\right\} + \frac{q_N}{\beta^2}\left\{\frac{1}{r}\xi_r\,\partial/\partial\xi\,(rv_1)\right. \quad (3\text{-}119)$$

$$\left. - \frac{\sigma_r}{r}\frac{\partial(r v_1)}{\partial \psi} + \frac{1}{r}\left[\xi_\theta \frac{\partial w_1}{\partial \theta} + \frac{\partial w_1}{\partial \psi}\right]\right\} - u_\xi \xi_x$$

$$v_x - \sigma_x v_\psi + \sigma_r \frac{\partial u}{\partial \psi} = -v_\xi \xi_x + u_\xi \xi_r \quad (3\text{-}120)$$

$$w_x - \sigma_x w_\psi - \frac{1}{r} u_\psi = -w_\xi \xi_x + \frac{1}{r} u_\xi \xi_\theta \quad (3\text{-}121)$$

Solution for the eigenvalues and vectors are similar to that for the body

$$\lambda_1 = -\sigma_x \mp \frac{[1+(r\sigma_r)^2]^{1/2}}{\beta r}, \lambda_2 = -\sigma_x \quad (3\text{-}122)$$

Choice of sign is dictated by the incoming characteristic on either side of a fin. The first sign is for the $\theta > \theta_f$ side.

Left eigenvectors are

$$L_1^1/L_3^1 = \pm\beta\,[1+(r\sigma_r)^2]^{1/2}$$

$$L_2^1/L_3^1 = -r\sigma_r \quad (3\text{-}123)$$

$$L_1^2 = 0, L_2^2 = 1, L_3^2 = r\sigma_r \quad (3\text{-}124)$$

The surface fin boundary advancement equations are evaluated at $\psi = 0$, where $\partial/\partial\psi \rightarrow \partial/\partial\theta$ for the thin-fin approximation. In the second advancement equation, θ may be eliminated by using the unused third irrotationality equation as was done for the body.

Terms involving $r\sigma_r$ are dropped. However,

$$\partial/\partial x\,(r\sigma_r) = -t_x/r \quad (3\text{-}125)$$

is retained. The first-order advancement equations may be written as

$$\frac{\partial E_{11}}{\partial x} + \frac{\partial G_{11}}{\partial \xi} + \frac{\partial H_1}{\partial \theta} = C_{11} \quad (3\text{-}126)$$

$$\frac{\partial E_{12}}{\partial x} + t_x \frac{\partial G_{12}}{\partial \xi} - \frac{\partial u_1}{\partial \xi} = C_{12} \tag{3-127}$$

$$E_{11} = \frac{\pm \beta u_1 + w_1}{c_4} \tag{3-128}$$

c_4 has been defined earlier in Section 3.6.

$$E_{12} = v_1/c_4 \tag{3-129}$$

$$G_{11} = - E_T/R \left(u_1 \pm \frac{w_1}{\beta}\right) \mp \frac{v_1}{\beta} + E_x(\pm \beta u_1 + w_1) \tag{3-130}$$

E_T and E_x have been defined in Section 3.3.

$$G_{12} = w_1 - v_1 E_T/R \tag{3-131}$$

$$H_1 = -d_1 [t_x(\pm \beta u_1 + w_1) + u_1 \pm w_1/\beta], d_1 = (1/\beta - R_b)/R \tag{3-132}$$

$$C_{11} = d_1 v_1 \left(\pm \frac{1}{\beta} + t_x\right) - a_2 \left(\pm \frac{w_1}{\beta} + u_1\right), d_2 = \frac{\tan \theta'}{\beta R} \tag{3-133}$$

$$C_{12} = d_2 t_x v_1 \tag{3-134}$$

The second-order advancement equations are of the form

$$\frac{\partial E_{21}}{\partial x} + \frac{\partial G_{21}}{\partial \xi} + \frac{\partial H_2}{\partial \theta} = C_{21} + q_N \left(\frac{\partial S}{\partial \xi} + \frac{\partial T}{\partial \theta}\right) \tag{3-135}$$

$$\frac{\partial E_{22}}{\partial x} + t_x \frac{\partial G_{21}}{\partial \xi} - \frac{\partial u_2}{\partial \xi} = C_{22} \tag{3-136}$$

$$E_{21} = (\pm \beta u_{2e} + w_2)/c_4 \tag{3-137}$$

$$E_{22} = v_2/c_4 \tag{3-138}$$

$$G_{21} = - \frac{E_T}{R} (u_2 \pm w_{2e}/\beta) \mp \frac{v_{2e}}{\beta} + E_x(\pm \beta u_{2e} + w_2) \tag{3-139}$$

$$G_{22} = w_2 - E_T v_2 / R \tag{3-140}$$

$$H_2 = -d_1 \left[t_x (\pm \beta u_{2e} + w_2) + u_2 \pm w_{2e}/\beta \right] \tag{3-141}$$

$$C_{21} = d_1 \left[\pm \frac{1}{\beta} (v_{2e} + q_N v_1) + t_x v_2 \right] - d_2 \left[\pm \frac{1}{\beta} (w_{2e} + q_N w_1) + u_2 \right] \tag{3-142}$$

$$C_{22} = d_2 t_x v_2, S = \pm \frac{1}{\beta} (v_1 + E_T w_1/R), T = \pm d_1 w_1/\beta \tag{3-143}$$

3.10 FIN-BODY CORNER ADVANCEMENT EQUATIONS

The fin-body junction is a crossflow geometry discontinuity. In Reference 10, the corner is treated as a single valued point or streamline.

A full characteristic analysis involves the matrix equation form

$$P_x + A P_\xi + B P_\psi = R \tag{3-144}$$

The body and fin analysis have already considered characteristics in the $\xi = 0$ and $\psi = 0$ planes. In the current case, $\xi = 0$, $\psi = 0$ at the corner. In Reference 10, no unique solution was found, if one considers the corner as a streamline and hence isentropic for the Euler equations. In Reference 10, a heuristic analysis led to two alternate differential equations for advancing p. p combined with isentropy, total enthalpy and the corner vector is enough to advance all variables.

Here, a nonunique set of relations is established by advancing $Q^2/2$ and using both boundary conditions for a streamline along a corner

$$\frac{1}{2} \frac{\partial Q^2}{\partial x} = - \frac{1}{(\gamma - 1) M_\infty^2} \partial/\partial x \left[(p/p_\infty)^{\frac{\gamma - 1}{\gamma}} \right] \tag{3-145}$$

$$V = \frac{\partial r_b}{\partial x} U + tan\,\theta' W \tag{3-146}$$

$$W = t_x U \tag{3-147}$$

Equation (3-145) may be combined with the three vector velocity advancement equations. A combined first- and second-order nonconservative advancement equation for (3-145) may be written as

$$\frac{\partial E_e}{\partial x} + \xi_x \frac{\partial E_e}{\partial \xi} - \frac{t_x}{r} \partial/\partial\theta (E_e) = V \xi_r \frac{\partial u}{\partial \xi} + \frac{W}{r} \left[\xi_\theta \frac{\partial u}{\partial \xi} + \frac{\partial u}{\partial \theta} \right] +$$

$$\frac{U_e}{\beta^2}\left[\frac{1}{r}\xi_r\,\partial/\partial\xi(rv_e)+\frac{1}{r}\xi_\theta\frac{\partial w_e}{\partial\xi}+\frac{1}{r}\frac{\partial w_e}{\partial\theta}\right]+\frac{U_e}{\beta^2}q_N\left[\frac{1}{r}\xi_r\,\partial/\partial\xi(rv_1)+\frac{1}{r}\xi_\theta\frac{\partial w_1}{\partial\xi}+\frac{1}{r}\frac{\partial w_1}{\partial\theta}\right] \tag{3-148}$$

All the transformation derivatives are to be evaluated at $\xi=0$, $\theta=\theta_f$. In addition,

$$U_e = U + \frac{A\,M_\infty^2}{\beta^2}, E_e = \frac{U_e^{\,2}+V^2+W^2}{2} \tag{3-149}$$

For first order, $A=0$, $v_e=v_1$, and $w_e=w_1$. For second order, $v_e=v_{2e}$ and $w_e=w_{2e}$.

3.11 EXPLICIT FINITE-DIFFERENCE SCHEME

The MacCormack scheme[20] is applied to body surface points, field points, fin surface points, and fin-body corner points. For all these points, the E vectors are to be advanced by a predictor-corrector finite-difference scheme. For the field, there are three vector equations; for the fin and body, there are two vector equations; and for the corner, there is a single equation.

$$E^* = E_i + \left(\frac{\partial E}{\partial x}\right)_i \Delta x$$

$$E_{i+1} = E_i + \frac{\Delta x}{2}\left[\left(\frac{\partial E}{\partial x}\right)^* + \left(\frac{\partial E}{\partial x}\right)_i\right] \tag{3-150}$$

E^* is computed utilizing $(\partial E/\partial x)_i$ which is evaluated by using forward or backward one-side differences for ξ and θ derivatives. E^* is utilized to decode for the new velocity components at the predicted conditions. The $(\partial E/\partial x)^*$ vector is utilized to obtain the final trapezoidal rule value of E_{i+1}. The reverse backward or forward one-sided differences for ξ and θ derivatives is used to evaluate $(\partial E/\partial x)^*$ at the predicted state. A decoding of the E_{i+1} vectors yields the advanced velocities. For field points, a code option uses forward ξ and θ differences for the predictor and backward ξ and θ differences for the corrector or alternate order from step to step. At the surfaces, the boundary conditions are also used in the decoding.

At a solid body surface, only forward differences in ξ are possible. If $k=2$ lies on a fin point, the ξ derivative is set to zero.

For fins, the θ differences must be always forward on the $\theta>\theta_f$ side and backward on the $\theta<\theta_f$ side. Points on a fin next to an edge need special consideration. For supersonic edges, ξ differences for points like A or B in Figure 2 are always backwards. For similar points on an inner edge, ξ differences are forward. For subsonic outer edges, a forward difference to a point in the flow such as C is taken. For the point C in the flow, the ξ difference for a supersonic edge is always forward. For a subsonic edge, a backward difference to the average of A and B values is utilized.

For explicit hyperbolic schemes, a CFL condition for stability is required. A formal analysis was not made. The step size is chosen so that the upstream Mach cone from a point at $x+\Delta x$ lies within the nearest grid points of the plane at x.

The radius of the Mach cone at x, $\theta+\Delta\theta$, and $\xi+\Delta\xi$ to first order is

$$\left(\frac{\Delta x}{\beta}\right)^2 = r^2 (\Delta\theta)^2 + \left[\frac{\partial r_b}{\partial \theta}(1-\xi)\Delta\theta + x(1/\beta - R_b)\Delta\xi\right]^2 \tag{3-151}$$

For a constant ξ value, Equation (3-151) is a minimum at the surface.

$$(\frac{\Delta x}{\beta})min = min\left\{r_b\left[1 + \left(\frac{1}{r_b}\frac{\partial r_b}{\partial\theta}\right)^2\right]^{1/2}\right\}\Delta\theta \tag{3-152}$$

For a constant θ ray,

$$(\Delta x)min = min\left\{(x/\beta - r_b)\Delta\xi/[\frac{1}{\beta} + |\frac{\partial r_b}{\partial x}|]\right\} \tag{3-153}$$

Equation (3-153) is a minimum at $\xi = 0$ as well in most applications. A search as θ varies for Equations (3-152) and (3-153) is made for (Δx) min. The step size chosen is 0.9 of this value.

Discontinuities create large differences in advancement point velocity values. These differences must somehow be dissipated for the first few steps after the discontinuity.

For a body planar discontinuity (e.g., a slope or inlet discontinuity), the ξ derivatives at $\xi = 0$ are set equal to zero for the first step and increased linearly to the full value after i_d steps, which is a code input. A curvature discontinuity does not have to be damped. However, much better results are obtained by marching up to the curvature discontinuity rather than across it. An i_d of 3 or 4 steps is usually adequate for damping body discontinuity disturbances.

At a fin leading edge, the θ discontinuity disturbance can be very large and, for swept back fins, it can continually be created until all ξ traces cross the leading edge. Both ξ and θ derivatives can be severely affected, in particular for a subsonic leading edge. The root velocities are also affected.

Only damping of the θ derivatives just past the leading edge is used. The number of steps, i_{df}, for damping is computed from the turning angle of Equations (3-112) or (3-113).

$$i_{df} = INT\left[|9.55\,DTH| + 0.5\right] \tag{3-154}$$

INT is the integer conversion of the floating point value. For a subsonic edge, the number of steps is doubled. At the root, $i_{df} = 6$ is chosen for a subsonic edge.

Damping of θ derivatives for the fin is similar to ξ derivative damping for a planar discontinuity. The derivatives are linearly increased from zero to the final value after i_{df} steps. At the root, no damping is used for the first i_{df} steps. The velocity vectors are advanced using the corner jump relations twice: for the first jump, the body shape is advanced; and for the second jump, the fin shape is advanced.

Due to the strong velocity oscillations on a fin with subsonic leading edges and for subsonic ridge or surface discontinuity lines, no attempt was made to compute jumps for fin ridge discontinuities. For a fin with all supersonic edges, the jumps could be computed.

It is assumed that for a good design, the body drag contributes most of the wave drag and, hence, the fin wave drag may be approximated. The normal force contribution of a fin is given fairly accurately by the planform. The wave drag of the fins is given by the thickness distribution and deflection angle of the fins. The characteristic compatability boundary condition will capture small jumps on the fin surface. An equivalent

thickness distribution would be given by multiplying the actual t_{ox} by a thickness reduction factor, t_{rf}, and then accounting for the actual fin thickness when the axial force contributions are computed. This will be elaborated on later.

In order to dampen, somewhat, the very large amplitude oscillations in the surface pressure for lifting surfaces with subsonic or nearly subsonic edges, a smoothing operation was introduced for the E vectors before decoding E_{i+1}.

A weighting function is chosen as $Q_s = V_1^2 + V_1^2 + W_1^2$, which is a positive definite quantity. Field, body surface, fin surface, and corner vectors, E^c, are smoothed as follows:

Field

$$\begin{aligned} E_{j,k} = (1 - C_{j-1,k} - C_{j+1,k} - C_{j,k-1} - C_{j,\,k+1}) E^c_{j,k} \\ + C_{j-1,k} E^c_{j-1,k} + C_{j+1,k} E^c_{j+1,k} + C_{j,k-1} E^c_{j,k-1} \\ + C_{j,k+1} E^c_{j,k+1} \end{aligned} \tag{3-155a}$$

Body

$$E_{j,1} = (1 - C_{j-1,1} - C_{j+1,1}) E^c_{j,1} + C_{j-1,1} E^c_{j-1,1} + C_{j+1,1} E^c_{j+1,1} \tag{3-155b}$$

Fin

$$E_{j,k} = (1 - C_{j,k-1} - C_{j,k+1}) E^c_{j,k} + C_{j,k-1} E^c_{j,k-1} + C_{j,k+1} E^c_{j,k+1} \tag{3-155c}$$

Corner

$$E_{j,k} = (1 - C_{j\pm1,1} - C_{j,2}) E^c_{j,1} + C_{j\pm1,1} E^c_{j\pm1,1} + C_{j,2} E^c_{j,2} \tag{3-155d}$$

Here,

$$C_{j\pm1,k} = C_s \frac{|(Q_s)_{j,k} - (Q_s)_{j\pm1,k}|}{\left|(Q_s)_{j,k} + (Q_s)_{j\pm1,k}\right|} \tag{3-156a}$$

$$C_{j,k\pm1} = \frac{C_s |(Q_s)_{j,k} - (Q_s)_{j,k\pm1}|}{\left|(Q_s)_{j,k} + (Q_s)_{j,k\pm1}\right|} \tag{3-156b}$$

C_s is a smoothing constant level, typically 0.2.

Note that on the $\theta > \theta_f$ side of the Nth fin, the data are stored at $j = JM + N$.

The damping smoother does somewhat limit the amplitude of oscillations. The oscillations die down far from the leading edge.

The explicit marching solution will fail when the value

$$1 + \frac{\gamma - 1}{2} M_\infty^2 (1 - Q^2)$$

becomes negative in Equation (3-93). To avoid a complete halt, the Bernoulli quantity is set to zero at a solid surface and the pressure becomes the vacuum value. Readjustment of the total velocity components requires two additional relations. One of these relations is given by the fin or body boundary conditions: at the corner, both boundary conditions are used; on the body, the W component remains unchanged; and on the fin, the V component remains unchanged. Sometimes useful results can be obtained by this delay of solution breakdown. A complete breakdown in the computation occurs when the vacuum values of C_p are propagated along the solid surfaces.

4.0 HIGH MACH NUMBER INVISCID SOLUTION

At high Mach numbers, the origin Mach cone crosses pointed body surfaces and other compressibility effects become dominant. Here, an adaption of the local pressure solution methods of Reference 9 is used. The local pressures depend primarily on the orientation of the local normal with respect to the free-stream velocity vector. These methods are extended and applied in References 21 and 22. The methods are summarized in Table 1. The methods use Newtonian, tangent cone, tangent wedge, and Prandtl-Meyer pressures and empirical blends of these.

As indicated in Section 1.0, Euler code solutions such as described in Reference 10 give good solutions for complex configurations. The local solution methods run much faster than the marching Euler solution and provide rapid trade-off computations; however, they sacrifice considerable accuracy.

5.0 INVISCID LOADING COEFFICIENTS

Axial Force Coefficient

$$A_R \frac{dC_A}{dx} = \int_o^{2\pi} r_b \frac{\partial r_b}{\partial x} C_{pb}\, d\theta + \sum_{n=1}^{NF} \int_{r_{in}}^{r_{on}} (C_{ppn}\, t_{xpn} - C_{pmn}\, t_{xmn})\, dr \tag{5-1}$$

Here: n refers to the fin number; C_{pp} is the pressure coefficient on the $\theta > \theta_f$ side; C_{pm} is the pressure coefficient on the $\theta < \theta_f$ side; t_{xp} and t_{xm} are corresponding body slopes; r_i and r_o are inner and outer fin edge radii; and b refers to the body.

Due to large control deflections, fin discontinuities, or subsonic leading edges, some finned body configurations cannot be computed at the given geometry. The computation is made at reduced values of $t_{oxn} = t_{xon}$. The adjustment to the fin contribution is given as

$$C_{ppn}\, t_{xpn} - C_{pmn}\, t_{xmn} = (C'_{ppn} - C'_{pmn}) \tan\delta_{fn} + t_{xon}/t^2_{rfn} (C'_{ppn} + C'_{pmn}) \tag{5-2}$$

Prime, here, refers to the reduced slope geometry values. One uncertainty is whether or not the second term in Equation (5-2) will be lost in the noise of the oscillating pressure contribution to lift. Here, $t_{rfn} = t_{xon}/t_{oxn}$.

Normal Force Coefficient

$$A_R \frac{dC_N}{dx} = -\int_o^{2\pi} \left(r_b \cos\theta + \frac{\partial r_b}{\partial \theta} \sin\theta\right) C_{pb}\, d\theta + \sum_{n=1}^{NF} \int_{r_{in}}^{r_{on}} (C_{ppn} - C_{pmn}) \sin\theta_{fn}\, dr \tag{5-3}$$

Pitching Moment Coefficient

$$L_R A_R \frac{dC_m}{dx} = -(x - x') A_R \frac{dC_N}{dx} + \int_o^{2\pi} r_b^2 \frac{\partial r_b}{\partial x} \cos\theta\, C_{pb}\, d\theta + \sum_{n=1}^{NF} \int_{r_{in}}^{r_{on}} r \cos\theta_{fn} (C_{ppn}\, t_{xpn} - C_{pmn}\, t_{xmn}) dr \tag{5-4}$$

It is not certain whether the adjustments of Equation (5-2) are really needed for the finned contribution of moment due to drag.

Large combinations of α and δ do not permit inviscid computation of pitching moment and normal force in the pitch plane. Computation at reduced values will permit extracting the linear dependences. First, the computation is made at α' with no control deflection. Then, the computation is made at α' with a control deflection δ'. This is readily done, since the computational code saves computational values up to a section end and can be restarted at the section end and run to the end of the body. For more than one set of control deflections, additional computations may have to be made.

The adjusted inviscid normal force coefficient is then given by

$$C_N = C'_N \sin\alpha / \sin\alpha' + \Delta C'_N \tan\delta / \tan\delta' \tag{5-5}$$

$\Delta C'_N$ is given by

$$\Delta C'_N = C'_N(\alpha', \delta' \neq o) - C'_N(\alpha', \delta = 0) \tag{5-6}$$

The pitching moment coefficient is treated in a similar manner. The remaining coefficients are assumed to be computed at small angles of attack and side slip. For configurations without quarter-plane symmetry, α and α' must be relative to the $C_N = 0$ angle of attack. Note that C_N and C_m do not go to zero simultaneously for half-plane symmetry.

Side Force Coefficient

$$A_R \frac{dC_Y}{dx} = \int_o^{2\pi} \left(r_b \sin\theta - \frac{\partial r_b}{\partial \theta} \cos\theta\right) C_{pb}\, d\theta + \sum_{n=1}^{NF} \int_{r_{in}}^{r_{on}} (C_{ppn} - C_{pmn}) \cos\theta_{fn}\, dr \tag{5-7}$$

Yawing Moment

$$L_R A_R \frac{dC_n}{dx} = -(x - x') A_R \frac{dC_Y}{dx} - \int_o^{2\pi} r_b^2 \frac{\partial r_b}{\partial x} \sin\theta\, C_{pb}\, d\theta - \sum_{n=1}^{NF} \int_{r_{in}}^{r_{on}} r\,(C_{ppn}\, t_{xpn} - C_{pmn}\, t_{xmn}) \sin\theta_{fn}\, dr \tag{5-8}$$

Rolling Moment

$$L_R A_R C_\ell = -\int_o^{2\pi} r_b \frac{\partial r_b}{\partial \theta} C_{pb}\, d\theta + \sum_{n=1}^{NF} \int_{r_{in}}^{r_{on}} r\,(C_{ppn} - C_{pmn})\, dr \tag{5-9}$$

The θ integrals need not be taken to 2π in all cases, except for LM = 6. For no fins, the θ integration is continuous. For a finned body section, the θ integrals are piecewise continuous. θ integration is approximated by a three- or four-point Simpson's rule. This implies a minimum of three points between fins. The θ variable step integration is converted to ϕ equal step integration by the $\partial\theta/\partial\phi\ \Delta\phi$ values.

The r integrations are carried out with the aid of the ξ and ζ transformations. A Simpson's three-point or trapezoidal rule integration is used for the points between k = KI, KO. KI and KO do not lie on the edges. The end interval integrations utilize an extrapolated trapezoidal rule.

After the body section computation is completed , the coefficients are integrated from the origin to a value of x (i.e., a load coefficient buildup). For a section with no fins, a piecewise leap-frog three-point or quadratic approximation for the coefficient gradients is utilized. For a section with fins, a piecewise linear approximation is utilized for the coefficient gradients. Note that those integrations are not the same as trapezoidal and Simpson's rules.

6.0 SKIN FRICTION, BASE PRESSURE, AND HIGH ANGLE-OF-ATTACK PREDICTION

6.1 SKIN FRICTION

The approach here is that described in Reference 23. The body skin friction is based on the body surface area and body length Reynolds number. The fin skin friction is based on twice the fin planform area and the

mean aerodynamic chord Reynolds number. The mean skin friction coefficient is given by the Van Driest model of Reference 24.

The skin friction coefficient for a body or fin element is given by

$$C_{AF} = \frac{S_w}{A_R}\left[C_{FL} + \frac{R_{NC}}{R_{NL}}\left(\frac{1.328}{\sqrt{R_{NC}}} - C_{FC}\right)\right] \quad for\, R_{NL} > R_{NC} \tag{6-1a}$$

$$C_{AF} = \frac{Sw}{A_R}\frac{1.328}{\sqrt{R_{NL}}} \quad for\, R_{NL} < R_{NC} \tag{6-1b}$$

Here S_w is the element wetted area, A_R is the reference area, R_{NC} is the critical Reynolds number, and R_{NL} is the element Reynolds number. R_{NC} for the body is chosen as 1.0×10^6 and 0.5×10^6 for a fin. The Reynolds number is given by

$$R_{NL} = R_{MFM}\, M_\infty (1.0 \times 10^6) L_c L \tag{6-2}$$

R_{MFM} is the Reynolds number, per Mach number, per foot, per million, which is a function of altitude for a given atmosphere. L_c is a conversion factor for converting the element length, L, to feet. C_{FL} and C_{FC} are mean skin friction coefficients at the Reynolds numbers R_{NL} and R_{NC}, respectively.

The mean skin friction coefficient is given by

$$d_1/\sqrt{C_F} - \log C_F = d_2 \tag{6-3}$$

where

$$d_1 = 0.55723\left[\sin^{-1}(C_1) + \sin^{-1}(C_2)\right] \Big/ \left[A\,(T_w/T_\infty)^{\frac{1}{2}}\right]$$

$$d_2 = \log R_N - 1.26 \log (T_w/T_\infty)$$

$$C_1 = (2A^2 - B)/(B^2 + 4A^2)^{\frac{1}{2}}$$

$$C_2 = B/(B^2 + 4A^2)^{\frac{1}{2}}$$

$$A = \left[\frac{\gamma - 1}{2} M_\infty^2/(T_w/T_\infty)\right]^{\frac{1}{2}}$$

$$B = \frac{1 + \frac{\gamma - 1}{2} M_\infty^2}{T_w/T_\infty} - 1$$

$$T_w/T_\infty = 1 + 0.9\,\frac{\gamma - 1}{2} M_\infty^2$$

C_F in Equation (6-3) is solved by iteration at $R_N = R_{NL}$ and $R_N = R_{NC}$.

L for the body is the body length. $L = L_f$, the mean chord, for the fin for a nontrapezoidal planform is estimated for an equivalent trapezoidal planform.

From Figure 3,

$$\tfrac{1}{2} S_w = A_F = \tfrac{1}{2} SMA\,(C_{rm} + C_{tm}) = \int_{XMI}^{XMA} (SO - SI)dx \tag{6-4}$$

$$\bar{S}\, A_F = \frac{1}{6} SMA^2 (C_{rm} + 2C_{tm}) = \tfrac{1}{2} \int_{XMI}^{XMA} (SO^2 - SI^2)dx \tag{6-5}$$

C_{rm} and C_{tm} are the equivalent trapezoidal planform root and tip chords, respectively. Use Equations (6-4) and (6-5) to solve for C_{rm} and C_{tm} and, then,

$$L_f = \frac{2}{3} \frac{(C_{rm}^3 - C_{tm}^3)}{(C_{rm}^2 - C_{tm}^2)} \tag{6-6}$$

This approach avoids having to compute the chord at the spanwise location of center of planform area.

6.2 BODY BASE PRESSURE AXIAL FORCE

A solid noncircular base is considered. No extensive set of data bases seems to be available. Approximate wake boundary layer interaction models or Navier-Stokes model solutions are not compatible within the current context of rapid computation.

A rational approximation is developed that utilizes a minimum of available data:

$$C_p = \bar{C}_{po} + \left[C_{pr}(\theta) - \bar{C}_{po} \right] r^2/r_b^2(\theta) \tag{6-7}$$

$$C_{prr} = C_{p3} \left[M'(\theta) \right] K + C_{p2}(M')(1 - K) \tag{6-8}$$

C_{prr} is the base pressure coefficient assuming a local free-stream Mach number, M'. In Reference 26, Chapman correlates base pressure data using $p_b/p_\infty = p_b/p'\ p'/p_\infty$ for axisymmetric bodies. p'/p_∞ is the pressure distribution at the end of a body extended by a pseudo cylinder. The cylinder has a diameter and length equal to the base diameter. For a noncircular cylinder, the cylinder length may be assumed to be equal to the equivalent circular diameter based on the base area, $(4\,A_b/\pi)^{\frac{1}{2}}$. This approach is possible for the low Mach number regime. The base pressure distribution then becomes

$$C_{pr} = C_{prr}(M')^2 (1/M_\infty^2 + 0.7\,C_p') - C_p' \tag{6-8a}$$

For higher Mach numbers, this approach does not seem feasible and C_{pr} is assumed to be $C_{pr} = C_{prr}$.

$$K = \left[|\kappa/\kappa_{ma}| \right]^{\frac{1}{2}}$$

$$\bar{C}_{po} = \frac{1}{2\pi} \int_0^{2\pi} C_{pr}\, d\theta \tag{6-9}$$

Here M' (θ) is the local Mach number at the end of the body, C_{p2} (M') and C_{p3} (M') are the mean base pressures from References 25 and 26, respectively. C_{p2} is the base pressure for a wide and long plate and C_{p3} is the base pressure at the end of a long cylinder. κ is the local curvature

$$\kappa(\theta) = - \frac{\left[-1 + \frac{1}{r_b} \frac{\partial^2 r_b}{\partial \theta^2} - 2 \left(\frac{1}{r_b} \frac{\partial r_b}{\partial \theta} \right)^2 \right]}{r_b \left[1 + \left(\frac{1}{r_b} \frac{\partial r_b}{\partial \theta} \right)^2 \right]^{3/2}} \tag{6-10}$$

κ_{ma} is the maximum curvature. For a circular base, K = 1 and $C_{prr} = C_{p3}$. However, for a circular base, there is still an angle-of-attack dependence. The C_p variations in Equations (6-7), (6-8), and (6-8a) are clearly arbitrary and need some correlation with data.

The base axial force coefficient is given by

$$C_{AB} = - \frac{1}{4} \frac{\int_c^{2\pi} r_b^2(\theta) \left[\bar{C}_{po} + C_{pr}(\theta) \right] d\theta}{A_R} \tag{6-11}$$

At low Mach numbers, the C_{pr} computation given by Equation (6-8a) is sensitive to the M' computation for bodies with lifting surfaces. In this case, the value of C_{AB} given by Equation (6-8) should also be computed with no body extension. A minimum of the two computations is the best choice.

6.3 HIGH ANGLE-OF-ATTACK PREDICTION

The methods of Reference 2 predict nonlinear charcteristics for the pitch plane as well as rolled orientation. These methods combine nose vortex tracking, surface singularity solution, leading and side edge suction, and fin shed vortex tracking.

An alternate approach is to adapt the crossflow lift extension of Reference 27.

$$C_N = C_{NI} + \frac{C_{dc} (M_\infty \sin\alpha)\, \eta(L') \sin\alpha |\sin\alpha|}{A_R} \int_o^L \frac{C_{NC} d}{C_{NCO}} dx \tag{6-12}$$

Here, C_{dc} is the crossflow drag coefficient for an infinite circular cylinder, η(L') is a correction factor for a finite length of L' "calibers", and d is the projected width of active loading perpendicular to the negative of the crossflow velocity vector. Supersonic leading edge width on fin spans are not included. Side edges and subsonic leading edges widths are included. L' is a mean caliber value given by

$$L' = L^2 / \int_o^L d\, dx \tag{6-13}$$

C_{NC} and C_{NCO} are the modified Newtonian estimates for the cross section of interest and for a circle of diameter d, respectively. Note that α should be with respect to the $C_N = 0$ angle of attack for half-plane body symmetry.

What is really being corrected by the Newtonian ratio is the different wake. The impact side should be estimated by C_{NI}, which is the inviscid normal force coefficient. Hence, the ratio refers to the lee side. For a body that is not symmetric about a horizontal plane, the crossflow lift for negative α is different than for positive α.

The pitching moment is given by a similar integration:

$$C_m = C_{mI} - \frac{C_{dc}\,\eta(L')\sin\alpha\,|\sin\alpha|}{A_R L_R}\int_o^L \frac{(x-x')\,C_{NC}}{C_{NCO}}\,d\,dx \tag{6-14}$$

Here, α should be with respect to the $C_m = 0$ angle of attack. Here, x' is the moment center location, L_R is the moment reference length, and C_{mI} is the inviscid moment contribution.

The evaluation of C_{NC} and C_{NCO} requires further development. Figure 6 illustrates some possibilities. For half a circular cylinder, the Newtonian normal force is $\frac{2}{3}\,d\,C_{po}$. For the wake surfaces,

$$C_{NC} = C_{po}\int_s (k'_c \cdot n_i)^2 \cos\theta\, ds \tag{6-15}$$

Here, s, is the arc length and the integral is the over all wake surfaces.

$$k'_c \cdot n_i = \frac{\left[\cos\theta + \frac{1}{r_b}\frac{\partial r_b}{\partial\theta}\sin\theta\right]\sin\alpha/|\sin\alpha|}{\left[1+\left(\frac{1}{r_b}\frac{\partial r_b}{\partial\theta}\right)^2\right]^{\frac{1}{2}}} \geq 0.0 \tag{6-16}$$

$$k'_c \cdot n_i = 0 \text{ for } k'_c \cdot n_i < 0.0$$

For a body with quarter-plane symmetry, Equation (6-16) is 0 at $\theta = \pi/2$. For a body with half-plane symmetry, Equation (6-16) will determine the shadow boundary at $\theta = \theta_v$. For $\alpha > 0$, $0 < \theta < \theta_v$ are the limits of integration. For $\alpha < 0$, the limits are $\theta_v < \theta < \pi$.

For the fin-body section, it is questionable as to what should be the wake surface and how much to integrate over. The choice taken here is to treat the body and fins independently.

The value of d, then, is

$$d = d_b + 2\sum_{n=1}^{NF} S_n \sin\theta_{fn} \tag{6-17}$$

Here NF is the number of fins in the half plane and S_n = SO-SI for each fin that has a side edge or leading edge that is subsonic. $C_{NC}/C_{NCO}d$ becomes

$$\frac{C_{NC}}{C_{NCO}} d = 3 \left\{ \int_{\theta_{MI}}^{\theta_{MA}} \frac{\cos\theta \left(\cos\theta + \frac{1}{r_b} \frac{\partial r_b}{\partial \theta} \sin\theta \right)^2}{\left[1 + \left(\frac{1}{r_b} \frac{\partial r_b}{\partial \theta} \right)^2 \right]^{\frac{1}{2}}} r_b \, d\theta + \sum_{n=1}^{N_F} S_n \sin^3 \theta_{fn} \right\} \tag{6-18}$$

Here, θ_{MA} is the maximum θ and θ_{MI} is the minimum θ as determined by Equation (6-16).

Thus, for a circular cross section with a monoplanar wing at $\theta_{fn} = 90$ deg and semispan, s, one obtains $C_{NC}/C_{NCO}\, d = d_b + 3s$ for a subsonic edge. d_b is the value for a supersonic edge.

In the application of Equations (6-12) and (6-14), the values of

$$\frac{\eta(L')}{A_R} \int_o^L \frac{C_{NC}}{C_{NCO}} \, d\,dx \text{ and } -\frac{\eta(L')}{A_R L_R} \int_o^L \frac{(x-x')\, C_{NC}}{C_{NCO}} \, d\,dx$$

are only geometry dependent.

In evaluating C_{NI} and C_{MI}, one must sometimes reduce the value of α to α' in order to obtain a computation at high angle of attack. The control deflection also must be reduced for large control deflections by a factor $t_{r\delta}$. For configurations without quarter-plane symmetry, α must be relative to the $C_N = 0$ angle of attack.

Pitch plane coefficients are then adjusted as

$$C_{NI} = C'_{NI} \sin\alpha / \sin\alpha' \cos\alpha + (C''_N - C'_N)/t_{r\delta} \tag{6-19}$$

$$C_{MI} = C'_{MI} \sin\alpha / \sin\alpha' \cos\alpha + (C''_{MI} - C_{MI}')/t_{r\delta} \tag{6-20}$$

Implementation of Equations (6-19) and (6-20) requires two separate runs: the first run is at $\alpha = \alpha'$ and the control deflections are zero; the second run is at $\alpha = \alpha'$ and the control deflections are reduced by $t_{r\delta}$. Single prime values are for the first run. Double prime values are for the second run. The values of α and α' must be altered for half-plane symmetry as earlier discussed.

The axial force coefficient prediction requires more extensive computation. The axial force coefficient is assumed to vary as

$$C_A = (C_{AO} + C_{A2} \sin^2\alpha) \cos\alpha + \tan\delta\, (C_{ADD} \tan\delta + C_{AND} \sin\alpha) \cos\alpha \tag{6-21}$$

Here,

$$(C_{AO} + C_{A2} \sin^2\alpha) \cos\alpha = C_{AB}(\alpha, \delta = 0) + C_{AF} + C_{AI}(\alpha, \delta = 0) \tag{6-22}$$

Four computations at ($\alpha = 0, \delta = 0$), ($\alpha \neq 0, \delta = 0$), ($\alpha = 0, \delta \neq 0$), and ($\alpha \neq 0, \delta \neq 0$) are required to approximate the four coefficients of Equation (6-21). However, the entire range of α and δ variation is established for a given Mach number. The restart capability limits the amount of computation required. C_{AI} is the inviscid component of axial force coefficient. C_A at large combinations of α and δ is nonlinear and difficult to estimate.

7.0 EVALUATION OF THE NUMERICAL METHODS

7.1 INVISCID POTENTIAL THEORY

7.1.1 Continuous Bodies Alone

A number of examples of the computational feasibility of the implicit Van Dyke model were given in References 6 and 7. The significant differences between first- and second-order linear potential theory are illustrated best by conical self-similar flows.

Figure 7 shows the computational comparison between the linear potential models and the explicit Euler model, SWINT, of Reference 10 and the full nonlinear potential implicit model of Reference 28. The reference area is the cone base area; reference length is the cone length; and moment center is the nose. The nonlinear potential code solution was an unpublished solution provided by G. Smith of DEI-Tech, Newport News, Va. The nonlinear solutions are distance asymptotic, while the linear potential solutions are given by an unfactored matrix inversion. The linear potential solution utilized a JM = 19, KM = 10 uniform grid. The nonlinear solver grids were finer. Figure 7 indicates that the second-order solution compares fairly well with nonlinear solutions and is a significant improvement over the first-order solution. Run time is much faster for obtaining a starting conical solution.

Figure 8 illustrates another cone solution for a body with a curvature discontinuity in the cross section. Stancil refers to the second-order linear potential surface singularity code of Reference 29 (the unpublished solution was provided by R. Stancil). References are the same as before. Note that the Stancil code runs longer than the nonlinear codes with only fair accuracy. Once again, the second-order potential provides a much improved solution. The second-order code utilized a clustered grid (nonuniform) with JM = 21, KM = 10.

Nonconical configurations have smaller body slopes further back on the body.

Figure 9 illustrates a computation for a body with 2/1 elliptical similar cross sections. The body is described by

$$r_b(x,\theta) = X(x)\,T(\theta) = \frac{tan\,(20\ deg)\,x\,(1-0.5\,x)}{(2.5\,+\,1.5\,cos\,2\theta)^{\frac{1}{2}}} \tag{7-1}$$

Reference area and lengths are the same as before. For the linear potential codes, JM = 21, KM = 8, IM = 21 (number of constant x step lengths). NCOREL refers to a full nonlinear potential implicit relaxation code solver of Reference 30. NANC is the current linear potential code. Note that the first-order solution is quite adequate for this overall slender configuration.

Figure 10 shows a very complex nonsimilar cross-section body for which a wind tunnel model with pressure taps is described in Reference 31. The body is given parametrically as

$$y_b/X(x) = \left\{1 + \left[1.35\,T(\theta_1) - 1\right] sin^2 \pi x\right\} sin\,\theta_1 \tag{7-2}$$

$$z_b/X(x) = \left\{1 + \left[1.35T(\theta_1) - 1 + 0.35/cos\,\theta_1\right] sin^2 \pi x\right\} cos\,\theta_1 \tag{7-3}$$

$$T(\theta_1) = \left[1.25 - 0.25\cos 2\theta_1 + 0.13174\,(\cos\theta_1 - \cos 3\,\theta_1)\right]^{-1} \tag{7-4}$$

$$y_b/z_b = \tan\theta \tag{7-5}$$

$$r_b = (y_b^2 + z_b^2)^{\frac{1}{2}} \tag{7-6}$$

Given θ, one can solve for θ_1 by Newton-Raphson iteration, utilizing Equations (7-2) through (7-5). C_p load comparisons with data are shown in Figure 11. References are as before. For this fairly blunt body, second-order results significantly improve the first-order results. The flow is separated for $x > 0.75$. However, the integrated pressure results agree quite well with the various computations.

The final continuous body comparison is shown in Figure 12. The body (described in Reference 32) has a Haack-Adams area distribution 3/1 elliptical cross section. Reference area is the maximum area at $x/L = 0.68$. Reference length is the equivalent circular body diameter, $L_R = (4\,A_R/\pi)^{\frac{1}{2}}$. Moments are taken about $x/L = 0.6$. The Haack-Adams equivalent axisymmetric body is described in Reference 33. Departure from the nonlinear potential solution can be attributed to compressibility. Additional departure from the data can be attributed to crossflow separation. The NCOREL computation is taken from Reference 30. Body description near the nose was modified so that the blunted body could be approximated as a pointed body. For $0 < x/L < 0.3$, a third-order polynomial for the equivalent circular body radius was used as described in Reference 7.

7.1.2 Discontinuous Bodies Alone

Some of the results to be shown here were described in Reference 8.

Figure 13 depicts a comparison with the data of Reference 16 and an Euler computation. The Euler computation starts with a blunt body solution computed by a separate time asymptotic Euler code followed by a computation to account for the angle of attack and then the explicit marching SWINT computation. The two different Van Dyke second-order potential axial source and doublet distribution computations of References 3 and 6 produce results superior to that shown for the second-order NANC solution. However, when the general approaches of References 3 and 6 were used to create a starting plane of data for an explicit marching solution, the results were inferior to that shown for the current NANC computation. The nose-cone junction is a curvature discontinuity that leads to a jump in velocity gradient and pressure gradient. It is seen that the axial force result is adequate, but that the normal force and pitching moment results are degraded. The results are very sensitive to the input gridding. An optimum selection of a (i.e., the match point) and DO that controls the step size may require several trial runs up to the nose-body junction.

Figure 14 depicts a demonstration of the capability of local 2-D jump relations to predict the pressure just downstream from a planar discontinuity. The Euler solution was taken from the tables of Reference 34. The first-order solution deviates significantly from the second-order solution before the discontinuity as well as after. The second-order linear jump prediction is comparable to the Van Dyke hybrid solution of Reference 5.

Figure 15 depicts the local pressure distribution just downstream from an inlet discontinuity. The inlet lip lies on a 15-deg ray from the origin. Compressive turning angles varied from 10.8 to 15.7 deg. Accuracy deteriorates as oblique shock detachment angles are approached. Second-order accuracy is still quite adequate when compared with the first-order solution. Reference area for $dC_N/d(x/D)$ is the cross-sectional area just downstream of the inlet face.

The last local jump solution case is taken from Reference 14. $M_\infty = 1.5$ on a long cylinder with all disturbance velocities equal to zero before a 12-deg boattail. The cylinder is at $\alpha = \beta' = 0$ flow inclination. For this case, Van Dyke showed that $B = 0$ gives a superior result. A table of second-order C_p values for various combinations of methods is given below for comparison with the Prandtl-Meyer value of $C_p = -0.293$:

	B=0	B=1
Linear Jump	−0.274	−0.122
Nonlinear Jump	−0.301	−0.223

Other computations show that $B = 0$ is superior for flares following a uniform flow also.

A last comparison is for the body of Figure 16. The first body section ($0 < x < 1.0$) varies from a 10-deg cone to a 10- by 20-deg elliptical cross section. The semi-major axis varies as $a = x\{\tan(10\text{ deg}) + [\tan(20\text{ deg}) - \tan(10\text{ deg})]x\}$. The second section ($1.0 < x < 2.0$) has an elliptical cross-section conical frustum with $b = \tan(10\text{ deg})\,x$ and $a = \tan(20\text{ deg})\,x$. The first discontinuity leads to a 0.0 to -8.8-deg expansion (compression is positive) over the quarter plane. The third section ($2.0 < x < 4.0$) is a constant cross-section ellipse with $b = 2\tan(15\text{ deg})$ and $a = 2\tan(20\text{ deg})$. The computational comparison is given in Figure 17. No suppression of derivatives is used for the first discontinuity. The second discontinuity has expansion turning angles from -7.5 deg to -20.7 deg. The ξ derivatives were suppressed for four steps after the second discontinuity. Reference area is the base area; reference length is $(4\,A_R/\pi)^{1/2}$; and moments are taken about $x = 2.0$.

7.1.3 Configurations with Lifting Surfaces

A large number of computations indicate that superior results occur for the approximate fin boundary condition, $F = 0.0$, for all fin computations. Figure 18 indicates some comparisons for supersonic leading edge jump conditions. The body shape is $r_b = \tan(15\text{ deg})\,x\,(1\text{-}0.5\,x)$. Flat plate fins begin at $x = 0.5$. The span, s, is 0.15. For $\lambda = 50$ deg, the compressive turning angles are too large for attached oblique shock solutions.

Figure 19 depicts a number of biconvex cruciform fin configurations in the 45-deg roll position. Comparisons with SWINT computations are made for various thickness ratios, t/c, and control deflections, δ, as given in Table 2. Results for FIN 4 are quite good, considering the fact that the pressure oscillations were strong for the subsonic leading edge case.

The next example is similar to the previous examples of Figures 19 and Table 2. The FIN 1 fins are rolled to the plus position. The horizontal fins are shifted back one-half caliber on the body so that the fins are staggered. The fins are flat plates. The fins are all deflected 10 deg (roll control). The body length is 6.5 calibers. Free-stream conditions and reference dimensions are the same as for the previous case. Coefficient comparisons with a SWINT computation are given below:

	C_A	C_N	C_M	C_Y	C_n	C_ℓ
NANC (1st)	0.32	0.74	−1.18	0.050	−0.23	1.27
NANC (2nd)	0.35	0.79	−1.23	0.053	−0.25	1.37
SWINT	0.33	0.82	−1.41	0.086	−0.34	1.28

It is seen that the first- and second-order computations compare favorably. The small induced side force and moment are sensitive computations.

The next computational example is for the configuration of Figure 20 and References 35 and 36. Data and computations are for $M_\infty = 1.5$. At this Mach number, the wing leading edge is subsonic and the tail leading edges are barely supersonic, but are treated computationally as subsonic. Figure 21 compares

pitching moment and normal force coefficients for two roll positions. In Figure 22, side moment and side force comparisons are shown. Rolling moment is a more nonlinear coefficient. At α_T = 10 deg, ϕ = 50 deg, the code predicts C_ℓ = -0.32; the data value is C_ℓ = -0.75. Reference area is the base area and reference length is the equivalent circular body diameter.

The next computational example is for a body-wing-tail configuration from Reference 32. A body-alone comparison has been made earlier in Figure 12. The geometry for the 3/1 ellipical cross-section body configuration is shown in Figure 23. Figure 24 shows a comparison of pitch plane coefficients. References are the same as for the body-alone case. Nonlinearity for the moment occurs for small α values. A roll control computation was attempted at M_∞ = 2.0, δ = 7.04 deg, α = 0 deg. C_ℓ = 0.39 for the computation and the data value is C_ℓ = 0.5. The computation is smoothed. An unsmoothed flat plate fin computation yields C_ℓ = 0.45.

Thus far, all the computational examples use analytical description of the body geometry. The next case taken from References 37 and 38 required a numerical input of data. The blunt nose variable elliptical cross-section body is shown in Figure 25. The spherical nose cap was input analytically. Numerical data were generated from the right-side columns of Table 3. The nose cap has a circular cross section and a discontinuity at the shoulder. The cross sections of the body vary from circular to a 3/1 ellipse and back to circular. The fins are the same as for the previous example. The body-alone forebody axial force (including surface friction) is 0.20; the experimental value is 0.18 for M_∞ = 2.5. References are the same as for the previous example. Figure 26 compares pitch plane body-alone comparisons with data. Note that the first-order theory needs a significant compressibility correction. For this complex shape, the second-order solution departs from the data significantly above a 4-deg angle of attack. Clearly, a crossflow correction will drive the solution in the wrong direction for second-order theory. First-order results will be improved by crossflow corrections. The flow over the rear portion of the body probably separates longitudinally as well as in the crossflow plane. C_N and C_m for the body-wing-tail configuration are compared in Figure 27. C_N comparisons are good. C_m is a sensitive computation for x_{cp} close to x'.

7.2 HIGH MACH NUMBER PREDICTION

Figures 28 and 29 depict comparisons for the configuration earlier considered in Figure 23 and described in Reference 32. The BWT1 comparison considers only the fin on the windward side. The BWT2 computation takes into account both fins. Note that the local solution method prediction for the body normal force is above the experimental, hence, a crossflow correction would be inappropriate. The same is true for the entire configuration. The same conclusion is true for the moment computation. x_{cp} experimentally is close to x' for the entire α range; hence, the computation is very sensitive. Departure from the data seems to occur at high angles of attack where the flow turning angles used for the local wedge shock and Prandtl-Meyer solutions on the lifting surfaces become large.

A slightly different approach is taken for the computation for the configuration shown in Figure 30 and taken from Reference 39. Figure 31 compares linear aerodynamics extrapolated from computations at α = 5 deg with data for M_∞ = 2.86. In this case, the normal force computation is below the data. The moment data are typically more nonlinear.

Computations for higher Mach numbers show the same trend as in Figures 28 and 29 for general configurations with lifting surfaces, but closer to the data. On the compression side at higher angles of attack, shock detachment is delayed for higher Mach numbers.

7.3. COMPLETE CONFIGURATIONS INCLUDING VISCOUS ESTIMATES

7.3.1 High Angle-of-Attack Normal Force and Pitching Moment

Here computational examples will be given for the quadratic dependencies on angle of attack predicted by Equations (6-12), (6-14), and (6-19) through (6-21).

Figure 32 depicts a comparison for the missile model of Figure 25 at $M_\infty = 2$. The normal force computation is quite good. All inviscid computations were made at $\alpha' = 5$ deg. The data departs from theory for the moment at small angles of attack as had been shown in an earlier inviscid computational comparison. The inviscid model is the second-order potential theory.

Figure 33 shows another comparison for the 3/1 elliptic body missile model at $M_\infty = 3.95$. The inviscid model is the local solution high Mach number estimate. Lifting surface contributions to the crossflow terms are neglected. The normal force computation is significantly improved over that for Figures 28 and 29 when $\alpha' = 5$ deg is used. The center of pressure is also not predicted well for this Mach number.

Figure 34 shows a third comparison for the 3/1 elliptical cross-section body model. This time the effect of a -10-deg control deflection was considered; $\alpha' = 3$ deg was used for this case. The increment due to control deflection was assumed to be a constant and was computed at $\alpha = 0$ deg. The actual control deflection about the fin plane was -7.04 deg. At $M_\infty = 1.3$, the computation was considerably more sensitive for the subsonic leading edges. Again, the data indicates considerable nonlinearity for the pitching moment close to zero magnitude.

The next computational comparison is for the configuration of Figure 35 and Reference 40. At $M_\infty = 2.5$, all leading edges are supersonic. The computations for $\alpha \leq 10$ deg were made directly. For $\alpha > 10$ deg, $\alpha' = 10$ deg was utilized. At $M_\infty = 2.5$, the comparison for pitching moment in Figure 36 is good, since the moment center is not close to the center of pressure.

7.3.2 Axial Forebody and Total Force Prediction

The first computational example for this section returns again to the 3/1 elliptical cross-section missile model. Figure 37 compares forebody and total axial force coefficient at $\alpha = 0$. The base pressure model leads to overprediction of the total axial force coefficient. The forebody axial coefficient is predicted somewhat better. It is not clear from Reference 32 what accuracy can be expected for the base pressure correction.

In Reference 39, the base pressure axial force coefficient is given as a function of angle of attack. A table of comparison for C_{AB} is given below

M	C_{AB}	C_{AB} (Data)
1.6	0.128	0.096
2.16	0.098	0.087
2.86	0.067	0.063

The current model overpredicts C_{AB}. Considerably more data are needed to modify the current estimate. At $M_\infty = 2.86$, the high Mach number model was used. Conversion from C_p to M uses the isentropic relation. This case has very large turning angles from the end of the cylindrical afterbody onto the boattail. The expansion angles vary from 9.5 to 16.0 deg.

The last computation in this section is for the 3/1 elliptical cross-section missile of earlier examples. Figure 33 depicts a comparison between data and theory for the forebody axial force at zero angle of attack with a -10-deg control deflection. At $M_\infty = 1.6$, the increment in axial force due to control deflection had to extracted from the zero thickness case. This increment was added to the undeflected fin case forebody axial force with nonzero thickness.

8.0 CONCLUDING REMARKS

Computational methods have been developed that predict the aerodynamic loading on noncircular body configurations for supersonic Mach numbers.

At small incidence and for the lower part of the Mach number range, considerable effort was expended in developing a finite-difference second-order linear potential model based on the ideas of M. D. Van Dyke. The implementation of the second-order model required some significant new research. Both first- and second-order solutions are obtained by implicit and explicit finite-difference marching computations. Other first-order potential solvers utilize surface singularity models almost exclusively. Jump discontinuities of supersonic leading and trailing edges of lifting surfaces and for planar body discontinuities are predicted by local 2-D jump relations based on the linear equations of conservation. At the subsonic leading and side edges of fins, the jump relations are not applicable and the computation would appear to be elliptic in character. The solutions in this case also have a strong square root singularity as well at the leading edge. It was anticipated initially that only a first-order surface singularity approach would remove this severe obstacle to successful computation. However, an approximate starting solution or jump solution at the fin edge followed by a marching solution did indeed lead to useful normal and even axial force prediction for fins with subsonic leading edges. However, the pressure coefficients are strongly oscillatory and the solutions are somewhat sensitive. For other configurations with no significant subsonic edges, the pressure predictions are quite good. For blunt nose bodies, the solution is poor on the nose, but overall aerodynamic coefficients are quite adequate. The entire body must lie within an effective origin of disturbances free-stream Mach cone.

The shearing transformation between the body surface and the free-stream Mach cone, the explicit boundary advancement model, the local 2-D jump relations, and the "thin fin" geometry model are motivated by the work of A. Wardlaw in developing the SWINT code. The SWINT code was also very useful for generating comparison computions where no experimental data were available.

The local solution model, when adapted properly, predicts quite adequate inviscid loads. Computational times are very short. The simple crossflow and average skin friction models predict forebody axial force and normal and pitching moment well when combined with the inviscid prediction for the pitch plane. A full 6-deg-of-freedom model at large incidence would require vortex generation and tracking methods.

The current computer code utilizes approximately 250,000 octal storage locations for a 15-by-60 grid. This storage requirement can be significantly reduced for the half-plane symmetry case where a 15-by-30 grid is adequate. Computational times depend on the gridding sizes and dimensions, body length, Mach number, and Mach number range. Computational times vary from 0.05 to 30 s for the CDC CYBER 875. Considerable flexibility in geometry and free-stream data input modes is built into the code. A separate user's guide is in preparation as a companion document to this report.

REFERENCES

1. A. E. Magnus and M. A. Epton, *PAN AIR-A Computer Program for Predicting Subsonic or Supersonic Linear Potential Flows About Arbitrary Configurations Using a Higher Order Panel Method, Vol. I - Theory Document*, NASA CR-3251, 1980.

2. M. F.E. Dillenius and J. N. Nielsen, *Computer Programs for Calculating Pressure Distributions Including Vortex Effects on Supersonic Monoplane or Cruciform Wing-Body-Tail Combinations with Round or Elliptical Bodies*, NASA CR-3122, April 1979.

3. F. G. Moore, *Body-Alone Aerodynamics of Guided and Unguided Projectiles at Subsonic, Transonic, and Supersonic Mach Numbers*, NWL TR 2796, November 1972.

4. L. Devan, L. A. Mason, and F. G. Moore, *Aerodynamics of Tactical Weapons to Mach Number 8 and Angles -of-Attack of 180 Degrees*, AIAA Paper 82-0250, AIAA 20th Aerospace Sciences Meeting, Orlando, Florida, January 1982.

5. M. D. Van Dyke, *First- and Second-Order Theory of Supersonic Flow Past Bodies of Revolution*, Journal of the Aeronautical Sciences, March 1951.

6. L. Devan, *Conical, Noncircular, Second-Order, Potential Theory of Supersonic Flow*, AIAA Journal, Vol. 22, No. 5, May 1984.

7. L. Devan and L. A. Kania, *Nonconical Nonaxisymmetric Body, Second-Order, Linear Supersonic Flow Prediction*, AIAA Paper 84-0313, AIAA 22nd Aerospace Sciences Meeting, Reno, Nevada, January 1984.

8. L. Devan and L. A. Kania, *Nonaxisymmetric Discontinuous Body, Second-Order, Linear, Supersonic Flow Prediction*, AIAA Paper 85-1810-CP, AIAA 12th Atmospheric Flight Mechanics Conference, Snowmass, Colorado, August 1985.

9. A. E. Gentry, D. N. Smyth, and W. R. Oliver, *The Mark IV Supersonic - Hypersonic Arbitrary - Body Program, Vol. I: Users Manual Vol. II: Program Formulation: Vol. III: Program Listings*, AFFDL TR 73-159, November 1973.

10. A. B. Wardlaw, Jr., J. M. Solomon, and F. P. Baltakis, *An Inviscid Computational Method for Tactical Missile Configurations*, NSWC TR 81-457, December 1981.

11. A. B. Wardlaw, Jr., L. B. Hackerman, and F. Baltakis, *An Inviscid Computational Method for Supersonic Missile Type Bodies-Program Description and User's Guide*, NSWC TR 81-459, December 1981.

12. F. J. Priolo, A. B. Wardlaw, Jr., F. P. Baltakis, and J. M. Solomon, *Inviscid Multiple Zone Strategy Applied to Complicated Supersonic Tactical Missile Configurations*, AIAA Paper 85-1813-CP, AIAA 12th Atmospheric Flight Mechanics Conference, Snowmass, Colorado, August 1985.

13. R. Courant, and D. Hilbert, *Methods of Mathematical Physics*, Vol. II, Interscience Publishers, 1953, pp. 486-490.

14. M. D. Van Dyke, *Practical Calculation of Second-Order Supersonic Flow Past Nonlifting Bodies of Revolution*, NACA TN 2744, July 1952.

15. C. P. Kentzer, *Discretization of Boundary Conditions on Moving Discontinuities*, Second International Conference on Numerical Methods in Fluid Dynamics, Berkeley, California, September 1970.

16. C. M. Jackson, W. C. Sawyer, and R. S. Smith, *A Method for Determining Surface Pressure on Blunt Bodies of Revolution at Small Angles of Attack in Supersonic Flow*, NASA TN D-4865, 1968.

17. C. A. Syvertson, and D. H. Dennis, *A Second-Order Shock-Expansion Method Applicable to Bodies of Revolution Near Zero Lift*, NACA TN 3577, January 1956.

18. L. A. Mason, L. Devan, F. G. Moore, and D. McMillan, *Aerodynamic Design Manual for Tactical Weapons*, NSWC TR 81-156, July 1981.

19. L. Devan, *An Improved Second-Order Theory of Inviscid Supersonic Flow Past Bodies of Revolution*, Paper 80-0030, AIAA 18th Aerospace Sciences Meeting, Pasadena, California, January 1980.

20. R. W. MacCormack, *The Effect of Viscosity on Hypervelocity Impact Cratering*, AIAA Paper 69-354, Cincinnati, Ohio, April 1969.

21. R. J. Krieger, J. E. Gregoire, R. F. Hood, E. A. Eiswirth, and M. L. Taylor, *Aerodynamic Configured Missile Development, Volume III - Missile Aerodynamics Prediction Rational Using the S/HABP*, AFWAL TR 80-3071, July 1980.

22. J. E. Williams, J. E.. Gregoire, and L. J. Mockapetris, *Aerodynamic Analysis for Missiles - Guide to Using S/HABP, APAS, and Aerodyn*, AFWAL TR 83-3007, February 1983.

23. F. G. Moore, *Aerodynamics of Guided and Unguided, Weapons Part I - Theory and Application*, NWL TR-3018, December 1973.

24. E. R. Van Driest, *Turbulent Boundary Layer in Compressible Fluids*, Journal of the Aeronautical Sciences, March 1951, pp 145-160, 216.

25. D. R. Chapman, W. R. Winbrow, and R. H. Kester, *Experimental Investigation of Base Pressure on Blunt-Trailing-Edge Wings at Supersonic Velocities*, NACA TR 1109, 1952.

26. D. R. Chapman, *An Analysis of Base Pressure at Supersonic Velocities and Comparison with Experiment*, NACA TR 1051, 1951.

27. L. H. Jorgenson, *A Method for Estimating Static Aerodynamic Characteristics for Slender Bodies of Circular and Noncircular Cross Section Alone and with Lifting Surfaces at Angles of Attack from 0° to 90°*, NASA TN D-7228, 1973.

28. V. Shankar, K.-Y. Szema, and E. Bonner, *Full Potential Methods for Analysis/Design of Complex Aerospace Configurations*, NASA CR 3982, May 1986.

29. R. T. Stancil, *Improved Wave Drag Predictions Using Modified Linear Theory*, Journal of Aircraft, Vol. 16, January 1979, pp 41-46.

30. M. J. Siclari, *The NCOREL Computer Program for 3D Nonlinear Supersonic Potential Flow Computations*, NASA CR 3694, 1983.

31. J. C. Townsend, D. T. Howell, I. K. Collins, and C. Hayes, *Surface Pressure Data on a Series of Analytic Forebodies at Mach Numbers from 1.7 to 4.5 and Combined Angles of Attack and Sideslip*, NACA TM 80002, May 1979.

32. E. B. Graves, *Aerodynamic Characteristics of a Monoplanar Missile Concept with Bodies of Circular and Elliptical Cross Sections*, NASA TM 74079, October 1977.

33. A. F. Bromm, Jr. and J. M. Goodwin, *Investigation at Supersonic Speeds of the Wave Drag of Seven Boattail Bodies of Revolution Designed for Minimum Wave Drag*, NACA TN 3054, December 1953.

34. K. L. Babenko, G. P. Voskresenskiy, A. N. Lyubimov, and V. V. Rusanov, *Three-Dimensional Flow of an Ideal Gas Past Smooth Bodies*, NASA TT F-300, April 1966 (Original Russian 1964).

35. F. K. Goodwin, and C. D. Dyer, *Data Report for an Extensive Store Separation Test Program Conducted at Supersonic Speeds*, AFFDL TR 79-3130, December 1979.

36. M. F. E. Dillenius, M. J. Hemsch, W. C. Sawyer, J. A. Allen, and A. B., Blair Jr., *Comprehensive Missile Aerodynamics Programs for Preliminary Design*, AIAA Paper 82-0375, AIAA 20th Aerospace Sciences Meeting, Orlando, Florida, January 1982.

37. E. B. Graves, and R. H. Fournier, *Effect of Nose Bluntness and Afterbody Shape on Aerodynamic Characteristics of a Monoplanar Missile Concept with Bodies of Circular and Elliptical Cross Sections at a Mach Number of 2.5*, NASA TM 80055, May 1979.

38. J. M. Allen, G. Hernandez, and M. Lamb, *Body-Surface Pressure Data on Two Monoplane-Wing Missile Configurations with Elliptical Cross Sections at Mach 2.5*, NASA TM 85645, September 1983.

39. W. C. Sawyer, and G. Sangiorgio, *Stability and Control Characteristics of a Monoplanar Elliptic Missile Model at Mach Numbers from 1.60 to 2.86*, NASA TP 1352, February 1979.

40. J. M. Allen, *Comparison of Analytical and Experimental Supersonic Aerodynamic Characteristics of a Forward Control Missile*, AIAA Paper No. 81-0398, AIAA 19th Aerospace Sciences Meeting, St. Louis, Missouri, January 1981.

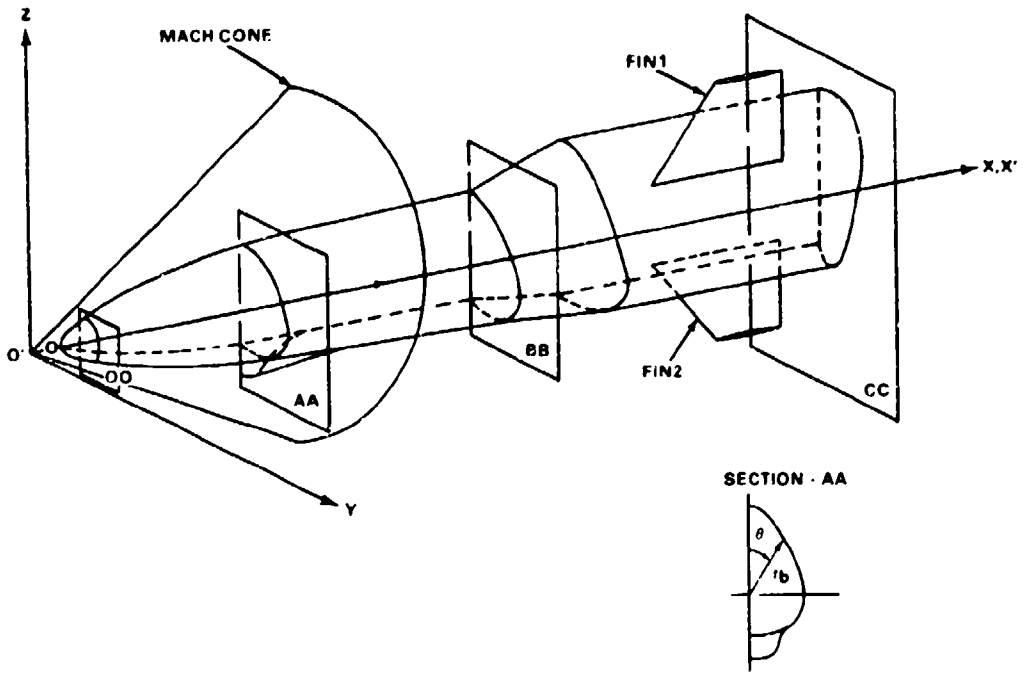

FIGURE 1. HALF-PLANE BODY GEOMETRY

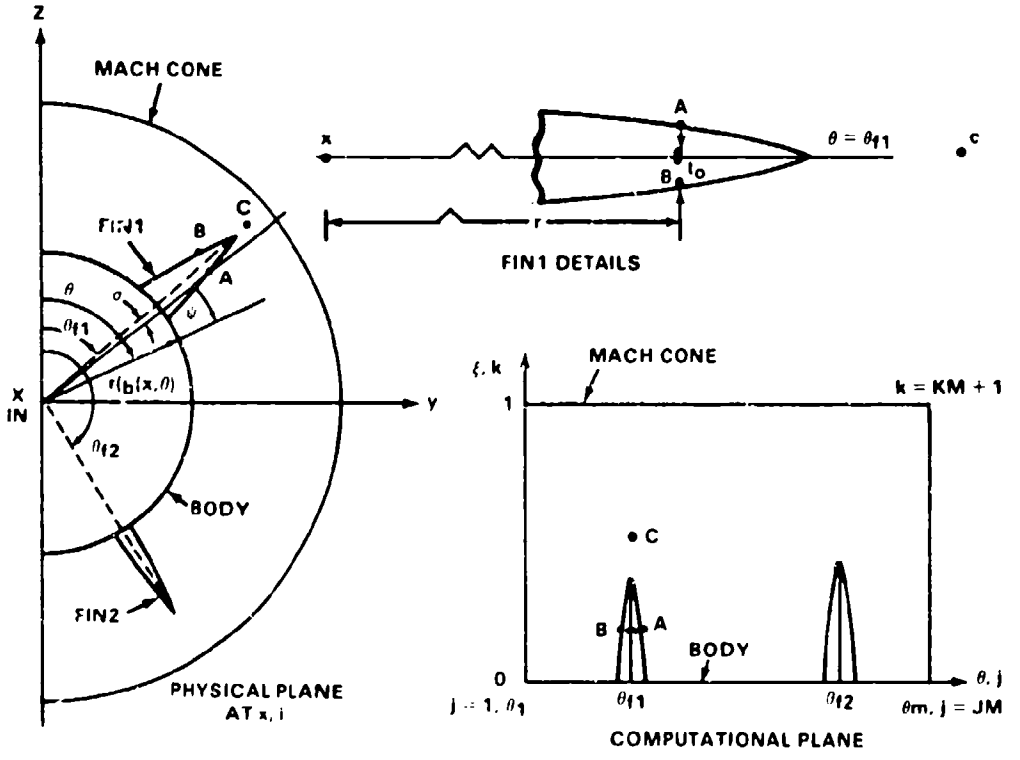

FIGURE 2. THIN FIN GEOMETRY

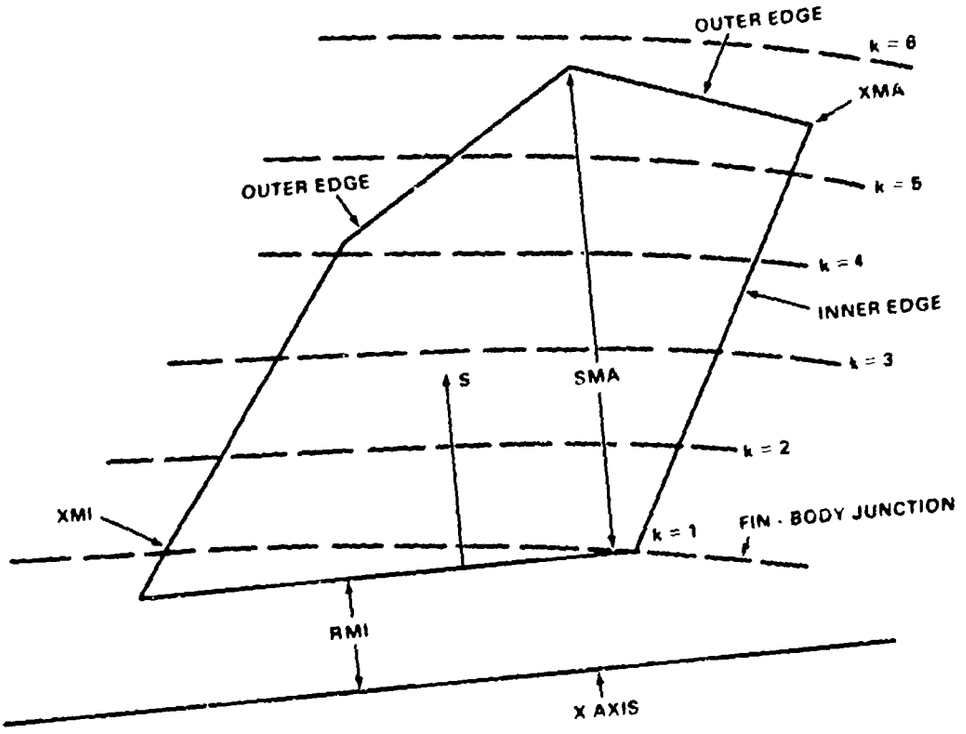

FIGURE 3. FIN PLANFORM GEOMETRY

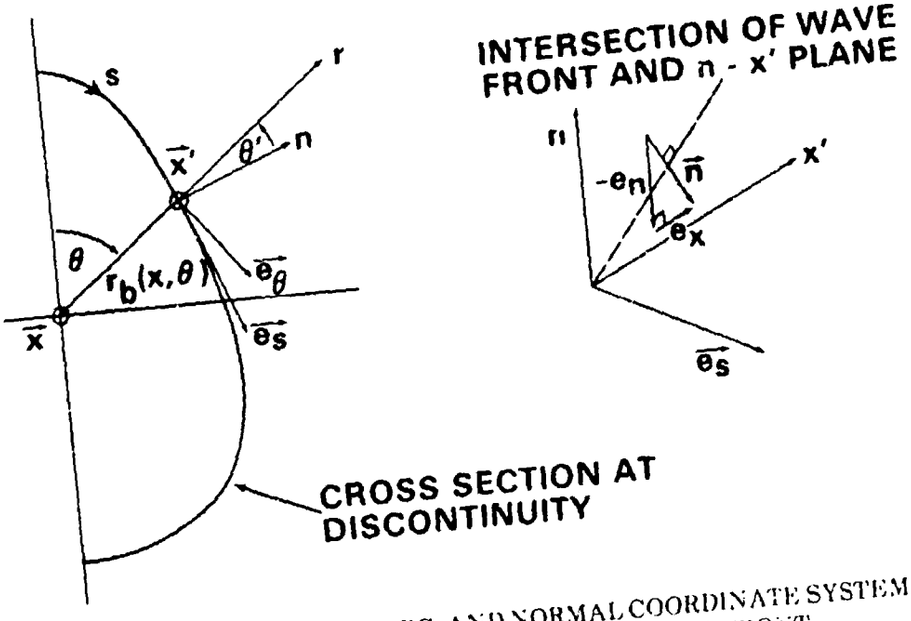

FIGURE 4. CYLINDRICAL, ARC, AND NORMAL COORDINATE SYSTEM ASSOCIATED WITH A DISCONTINUITY WAVEFRONT

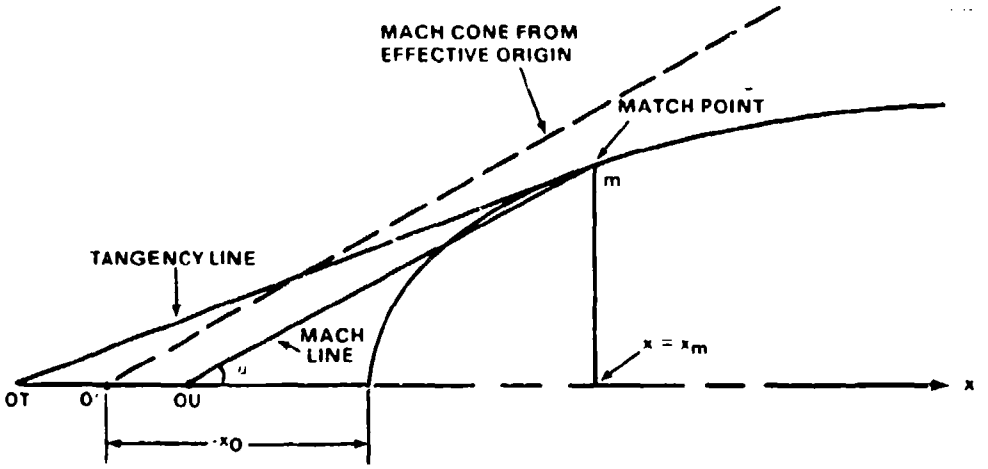

FIGURE 5. BLUNT BODY GEOMETRY

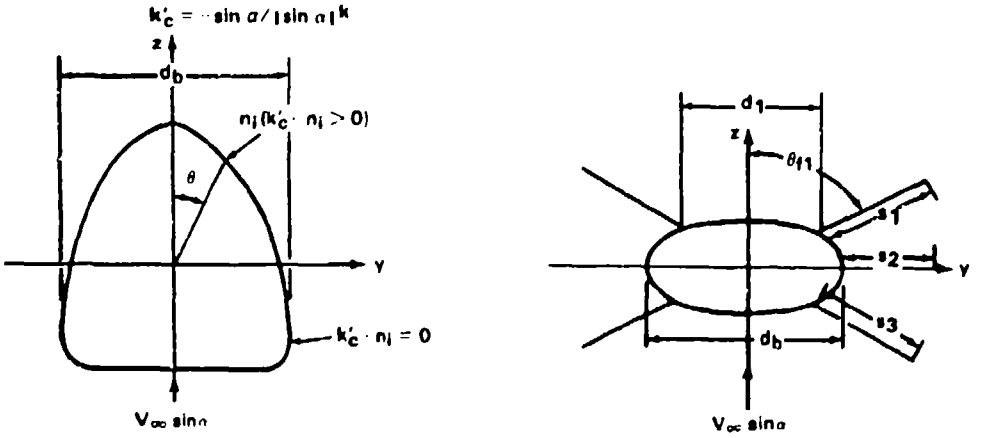

FIGURE 6. WAKE SHADOW GEOMETRY FOR NEWTONIAN CROSSFLOW ESTIMATES

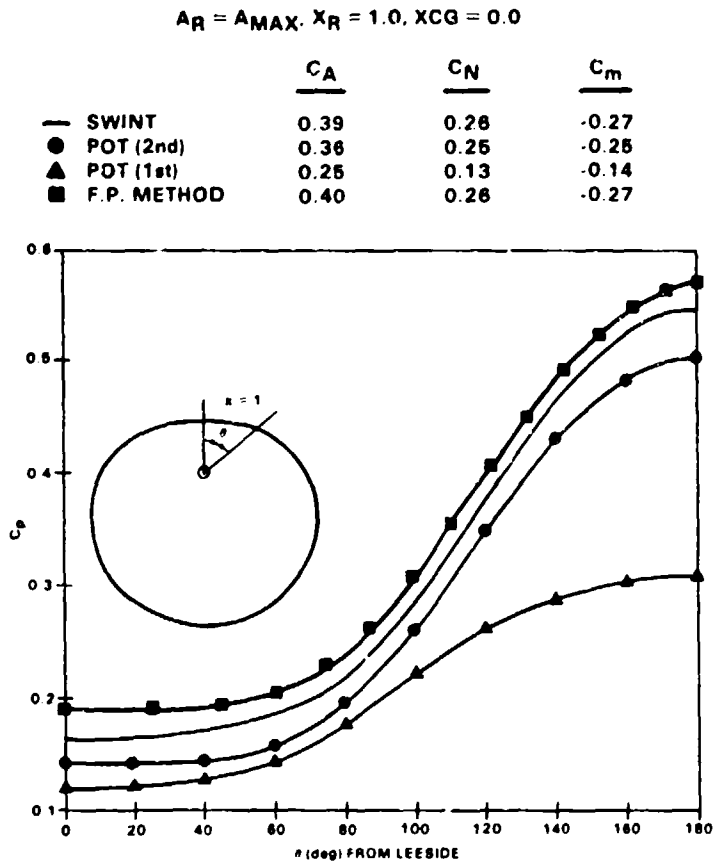

FIGURE 7. COMPARISON COMPUTATIONS FOR A dr_b/dx = tan (20 deg) (1-0.5 cos θ), CONE, $M_\infty = 2.0$, $\alpha = 0.0$ DEG, $\beta' = 0.0$ DEG

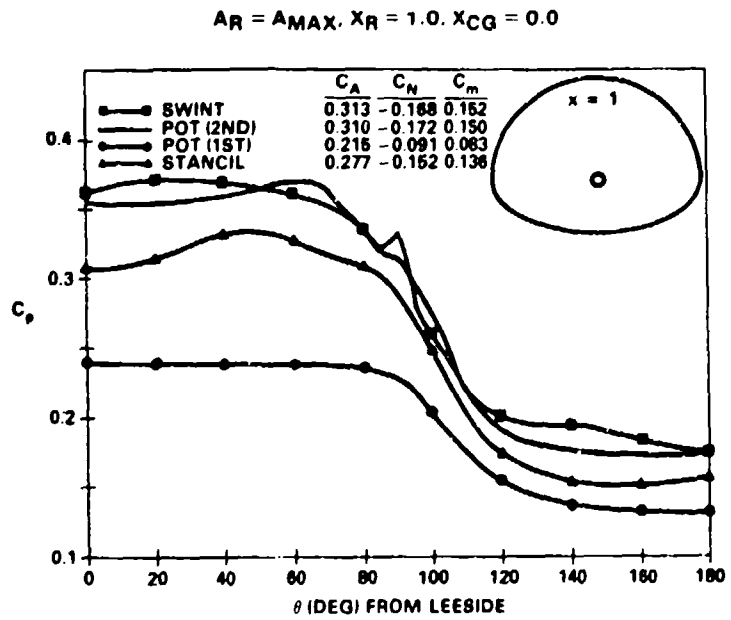

FIGURE 8. COMPARISON COMPUTATIONS, HALF CIRCLE, $dr_b/dx = 0.4$ ($0 < \theta < 90$ deg); HALF 2/1 ELLIPSE, $M_\infty = 2$, $\alpha = 0.0$ DEG, $\beta' = 0.0$ DEG

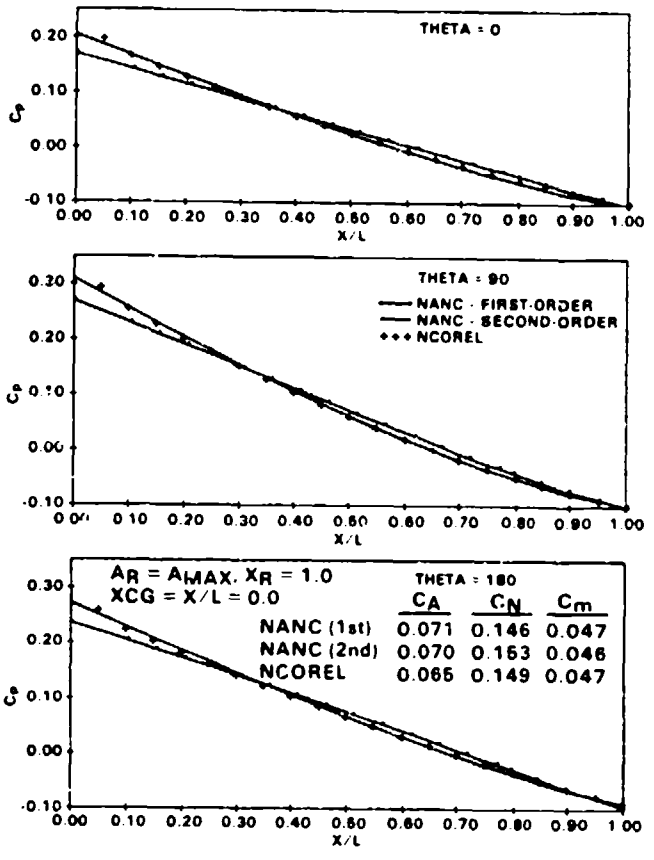

FIGURE 9. COMPARISONS FOR 2/1 ELLIPTICAL CROSS-SECTION BODY, $M_\infty = 1.2$, $\alpha = 2.$ DEG, $\beta' = 0.0$ DEG

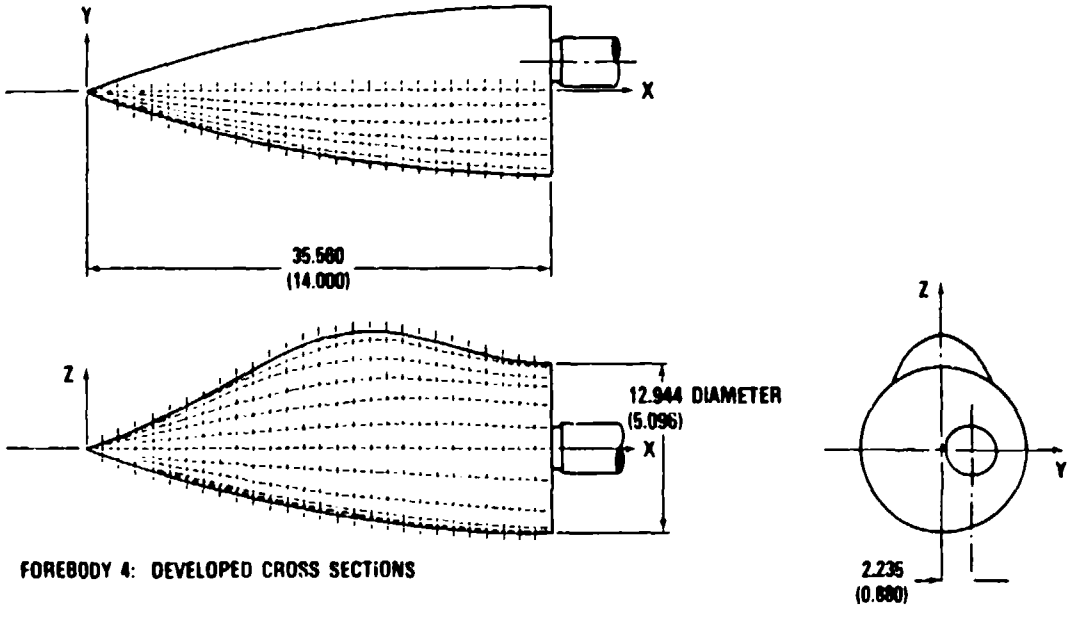

FIGURE 10. NONSIMILAR NASA FOREBODY

$A_R = A_{MAX}$, $X_R = 1.0$, $X_{CG} = 0.0$

	C_A	C_N	C_m	C_y	C_n	C_ℓ
NANC (1st)	0.173	0.265	0.048	-0.268	-0.083	-0.0043
NANC (2nd)	0.209	0.295	0.041	-0.333	-0.095	-0.0071
SWINT INTEGRATED Cp DATA	0.208	0.312	0.039	-0.315	-0.087	-0.0070
	0.215	0.270	0.035	-0.319	-0.090	-0.0070

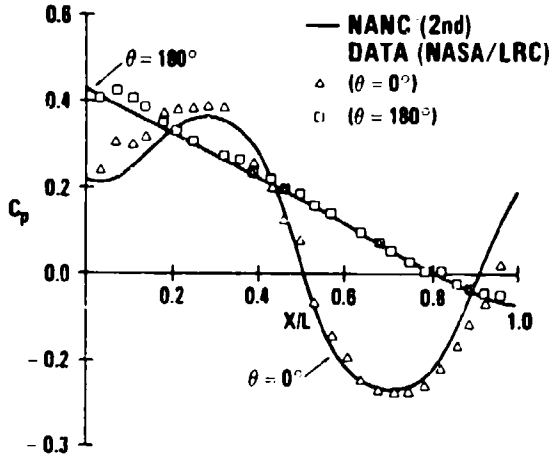

FIGURE 11a. C_p (0,180 DEG) AND TOTAL LOAD COMPARISONS FOR FOREBODY 4, $M_\infty = 1.7$, $\alpha = 5.0$ DEG, $\beta' = 5.02$ DEG

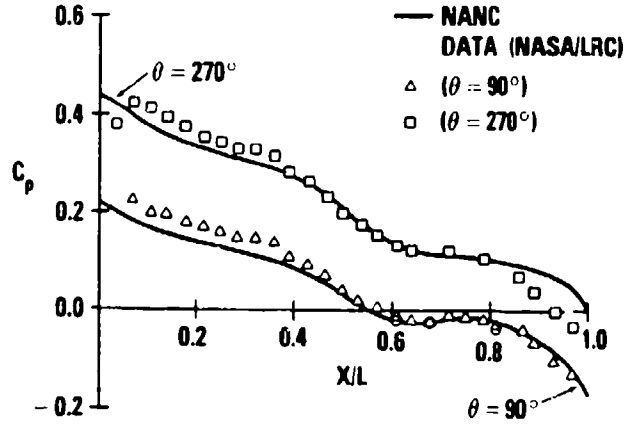

FIGURE 11b. C_p (90, 270 DEG) COMPARISON FOR FOREBODY 4, $M_\infty = 1.7$, $\alpha = 5.0$ DEG, $\beta' = 5.02$ DEG

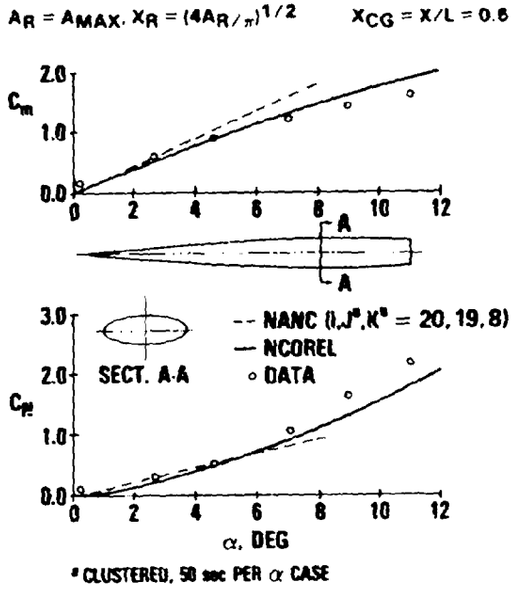

FIGURE 12. HAACK-ADAMS 3/1 ELLIPTICAL CROSS-SECTION BODY C_N AND C_m COMPARISONS, $M_\infty = 2$

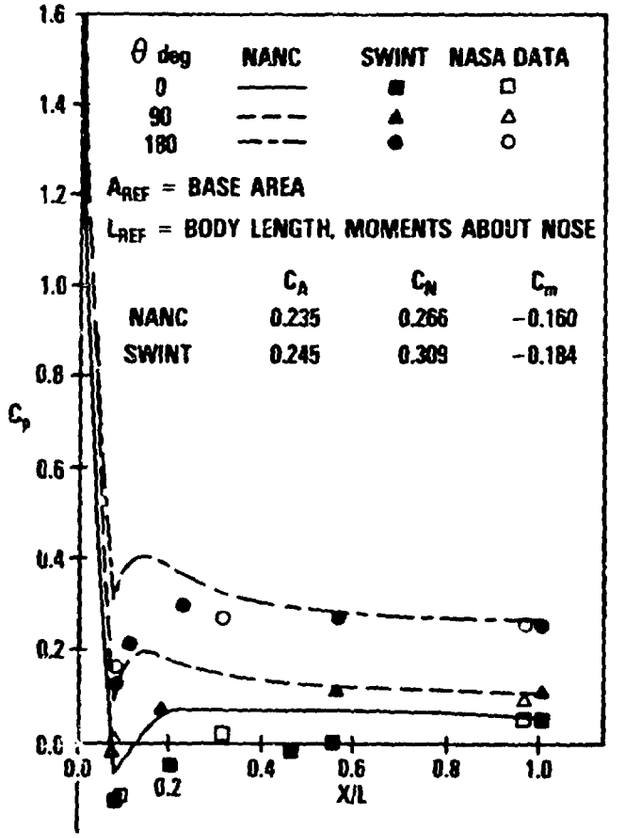

FIGURE 13. COMPARISON OF NASA DATA WITH SWINT AND NANC FOR A BLUNTED CONE, $M_\infty = 1.9$, $\alpha = 8$ DEG, $r_n = 0.175$ CALIBERS, $\delta_c = 11.5$ DEG

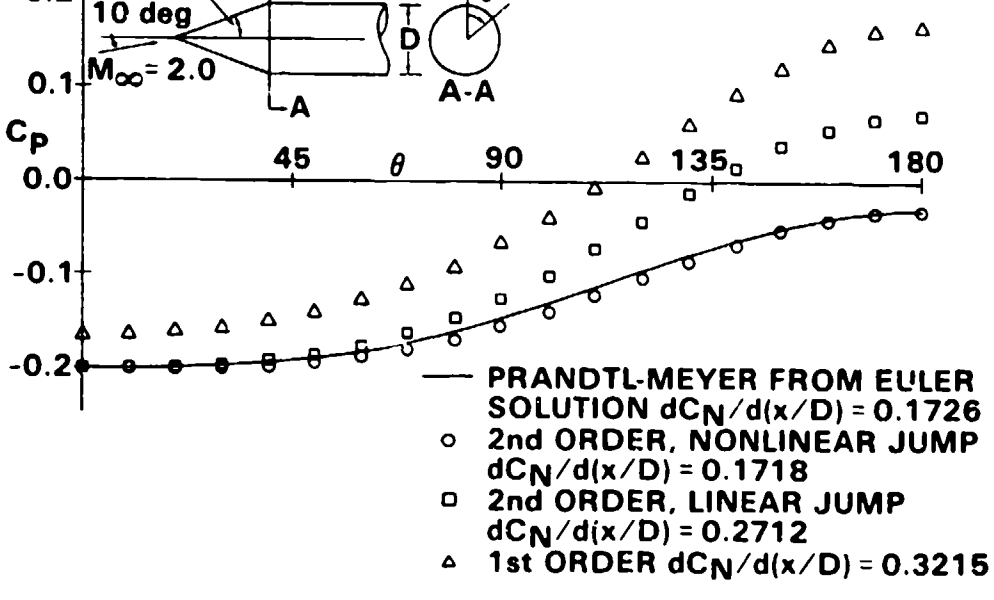

FIGURE 14. C_p AND $dC_N/d\,(x/D)$ COMPARISONS FOR A CONE-CYLINDER DISCONTINUITY

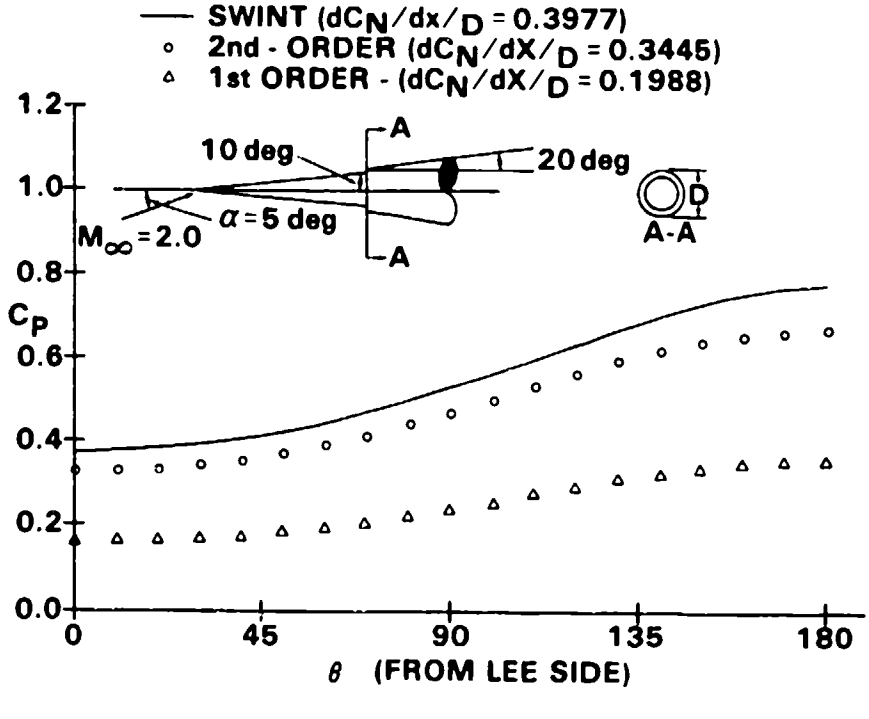

FIGURE 15. C_p AND $dC_N/d\,(x/D)$ COMPARISONS FOR A CIRCULAR INLET DISCONTINUITY

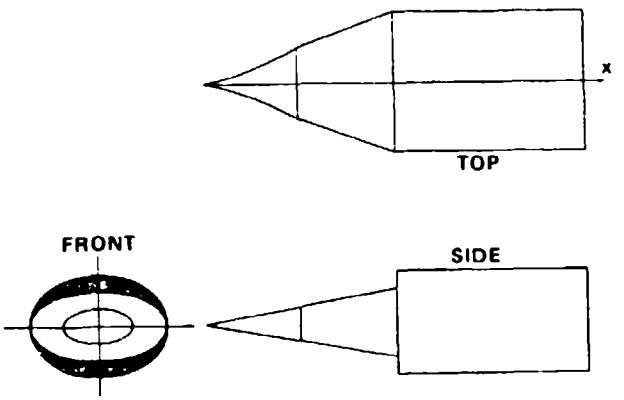

FIGURE 16. INLET-CYLINDER BODY WITH TWO DISCONTINUITIES

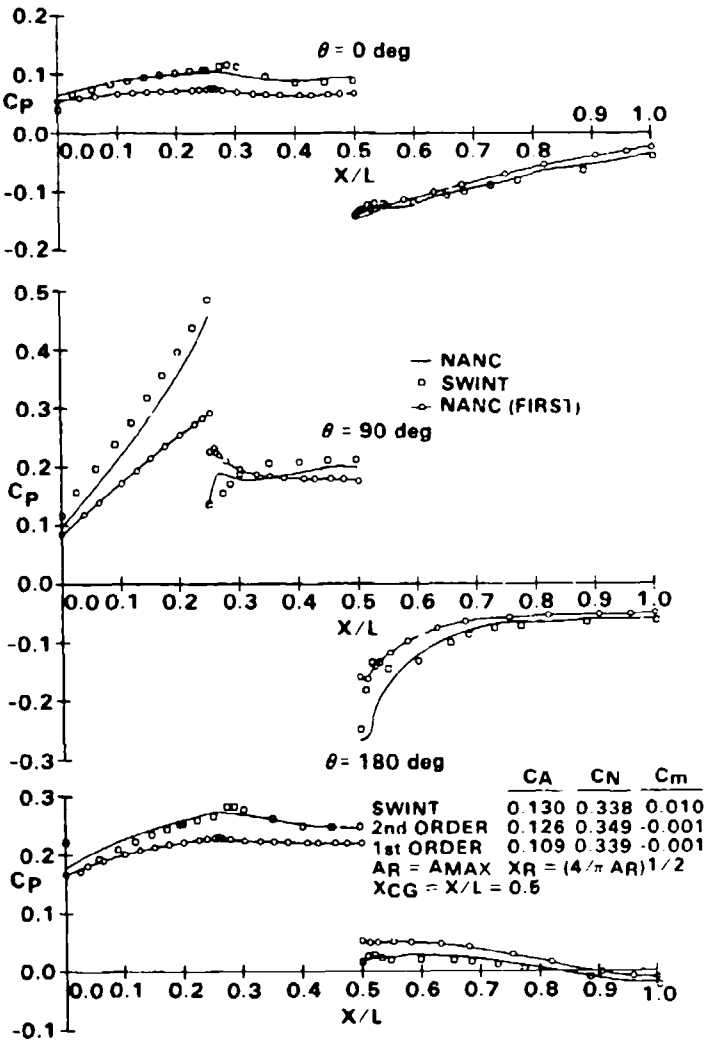

FIGURE 17. C_p AND AERODYNAMIC COEFFICIENT COMPARISONS FOR AN INLET-CYLINDER BODY, $M_\infty = 1.7$, $\alpha = 5$ DEG, $\beta' = 0$ DEG

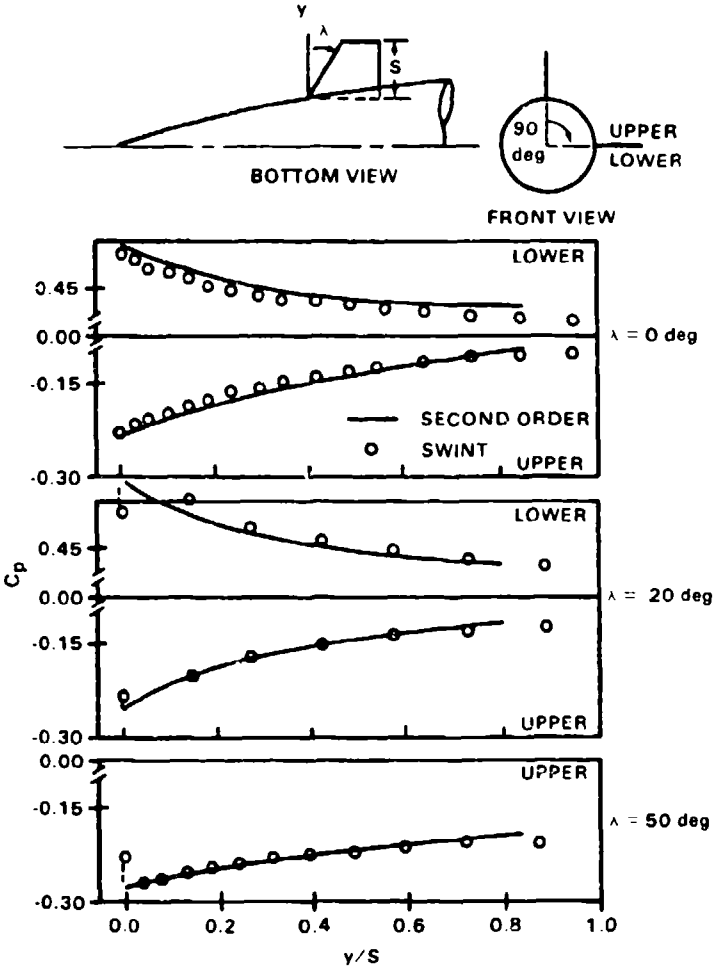

FIGURE 18. LEADING EDGE JUMPS FOR VARIOUS SWEEP ANGLES, $M_\infty = 2$, $\alpha = 10$ DEG

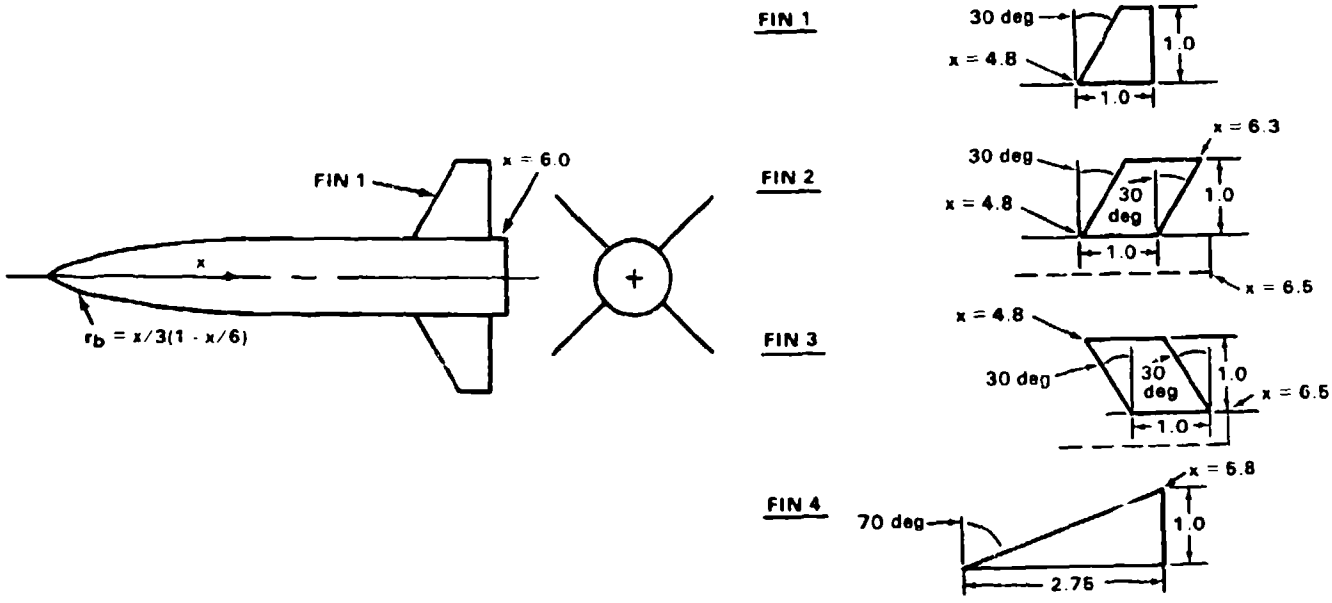

FIGURE 19. BODY-TAIL CONFIGURATIONS IN CALIBER DIMENSIONS

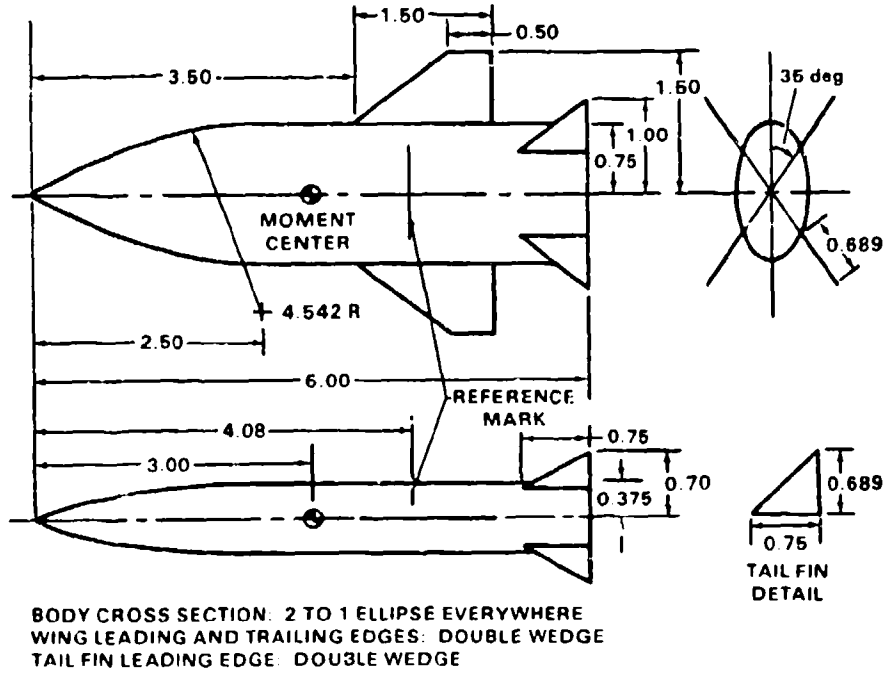

FIGURE 20. 2/1 ELLIPTICAL CROSS-SECTION BODY CONFIGURATION

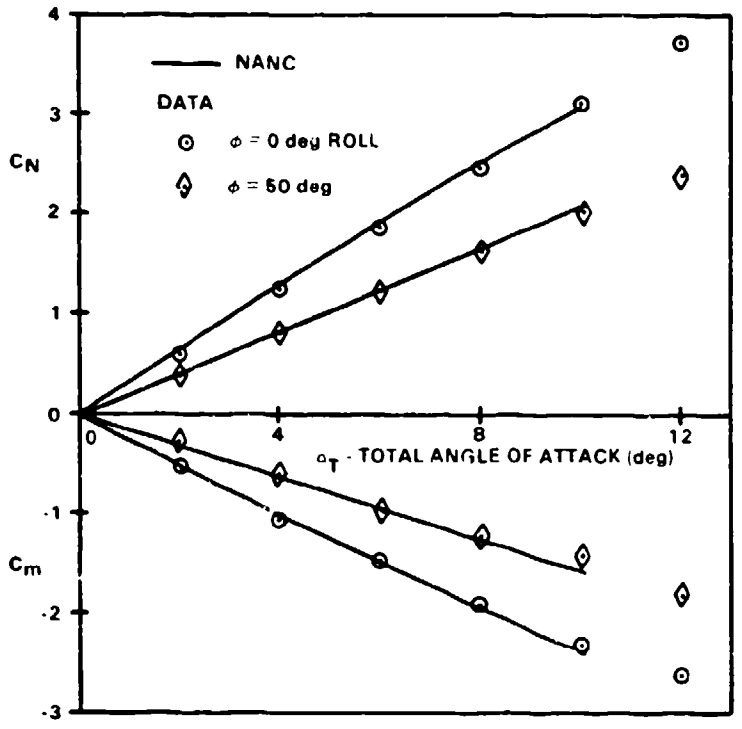

FIGURE 21. C_N AND C_m COMPARISONS FOR A 2/1 ELLIPTICAL CROSS-SECTION MISSILE, $M_\infty = 1.5$, $\phi = 0$ DEG, $\phi = 50$ DEG

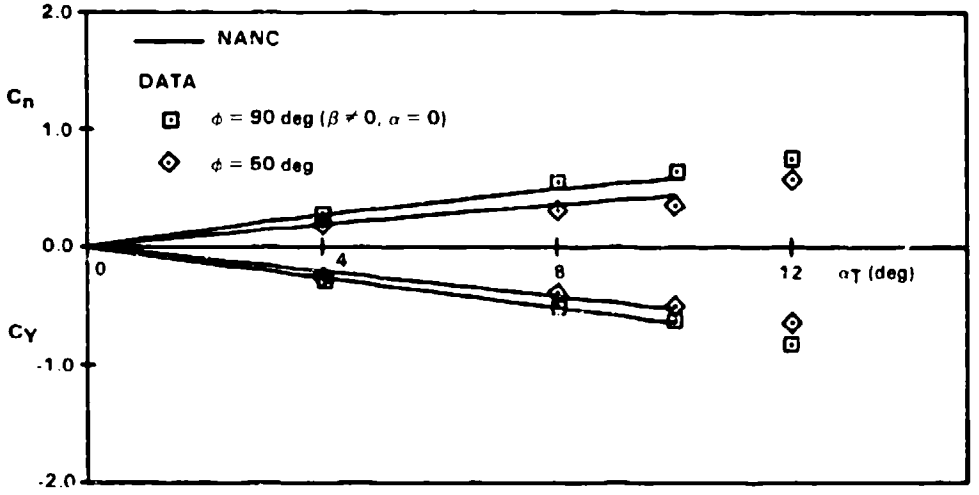

FIGURE 22. C_Y AND C_n COMPARISONS FOR A 2/1 ELLIPTICAL CROSS-SECTION MISSILE, $M_\infty = 1.5$, $\phi = 90$ DEG, $\phi = 50$ DEG

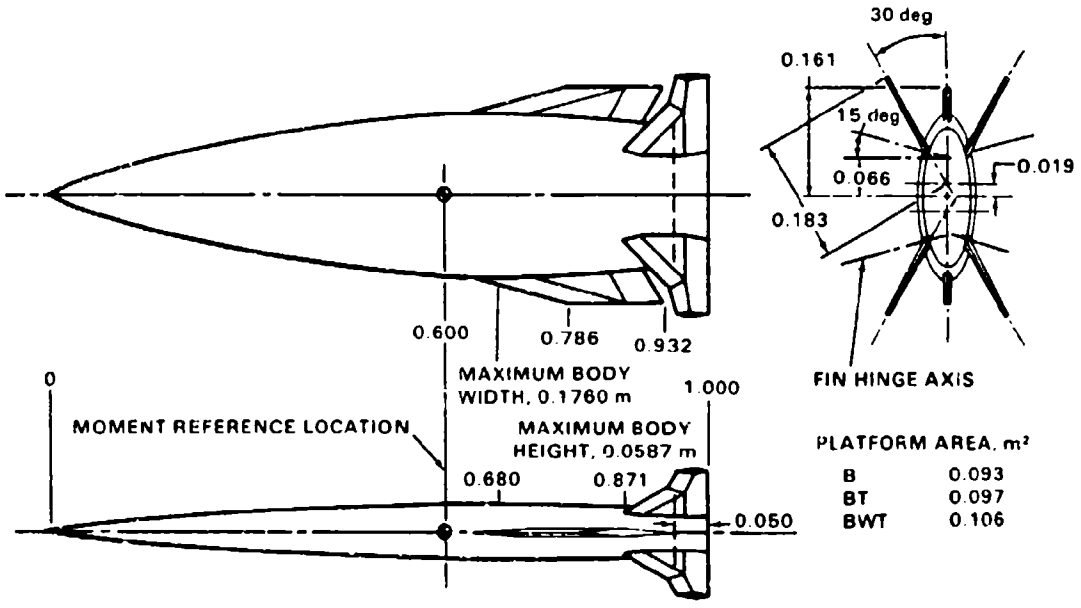

FIGURE 23. 3/1 ELLIPTICAL BWT CONFIGURATION
(DIMENSIONS IN BODY LENGTHS)

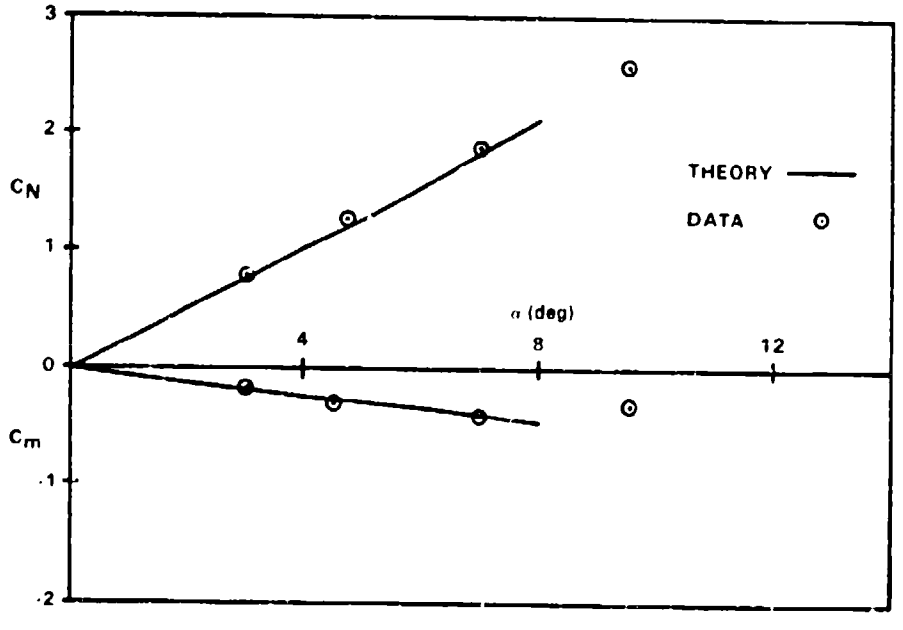

FIGURE 24. C_N AND C_m COMPARISONS FOR A 3/1 ELLIPTICAL CROSS SECTION BWT CONFIGURATION, $M_\infty = 2.0$

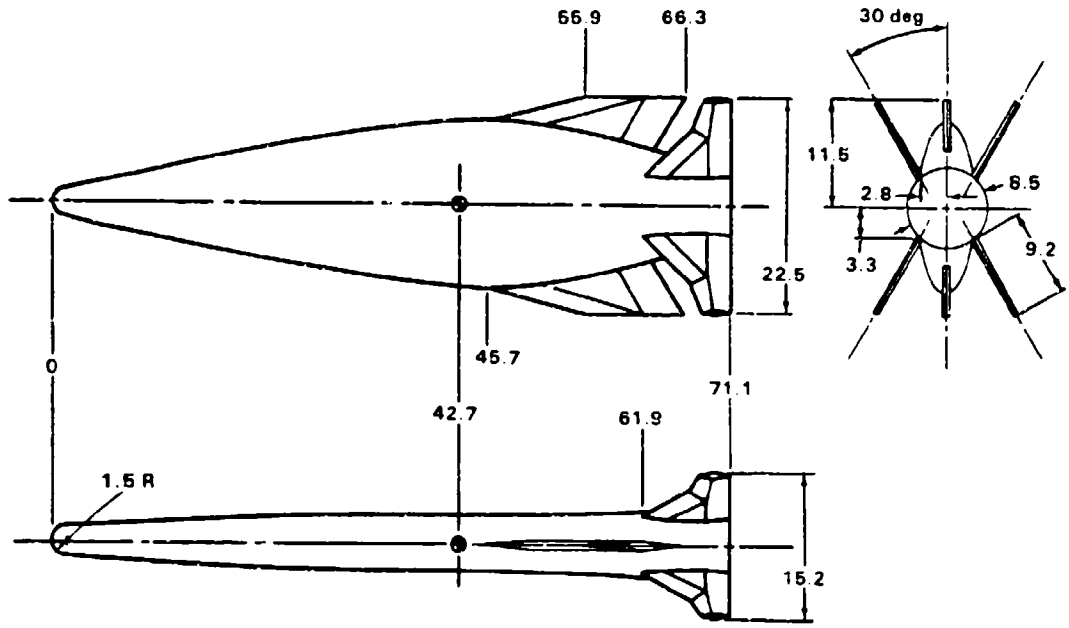

FIGURE 25. VARIABLE ELLIPTICAL CROSS-SECTION BODY MISSILE MODEL (DIMENSIONS IN CENTIMETERS)

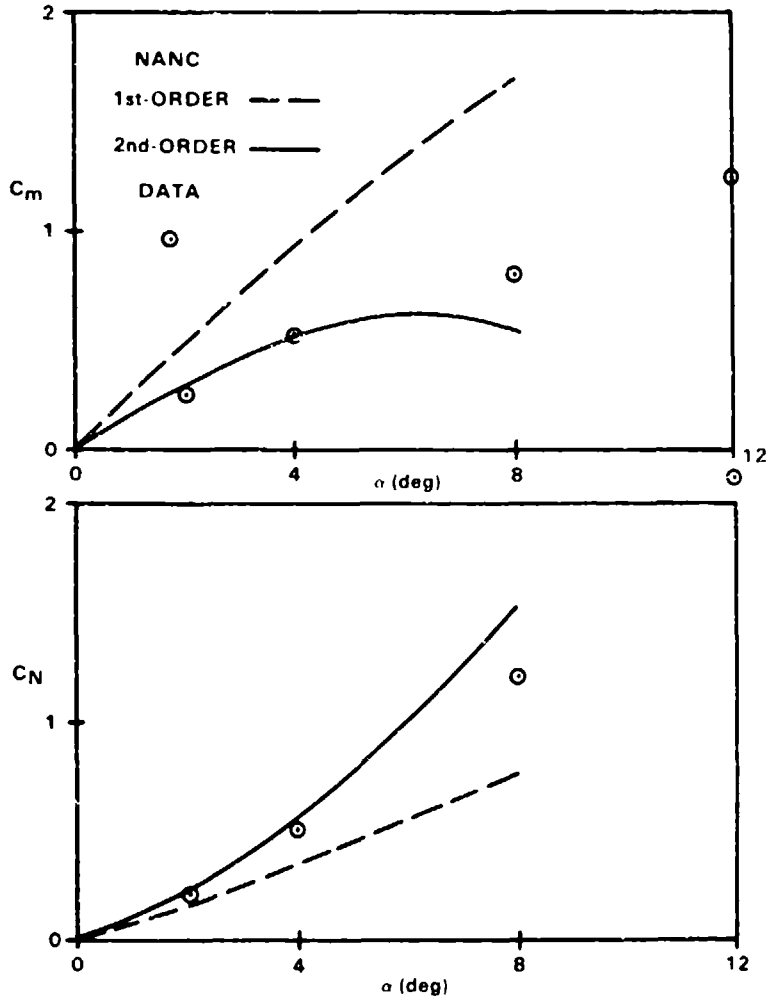

FIGURE 26. C_N AND C_m COMPARISONS FOR A VARIABLE ELLIPTICAL CROSS-SECTION BLUNTED BODY, $M_\infty = 2.5$

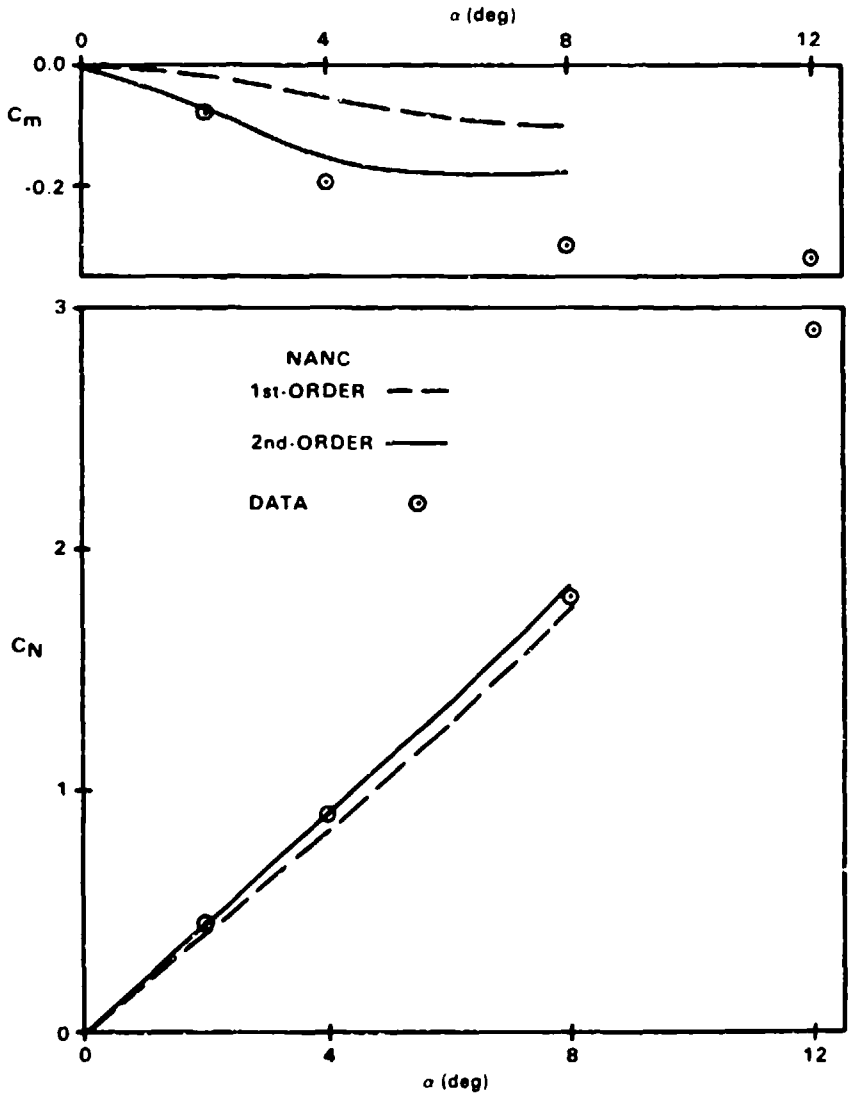

FIGURE 27. C_N AND C_m FOR A VARIABLE ELLIPTICAL CROSS-SECTION BWT CONFIGURATION, $M_\infty = 2.5$

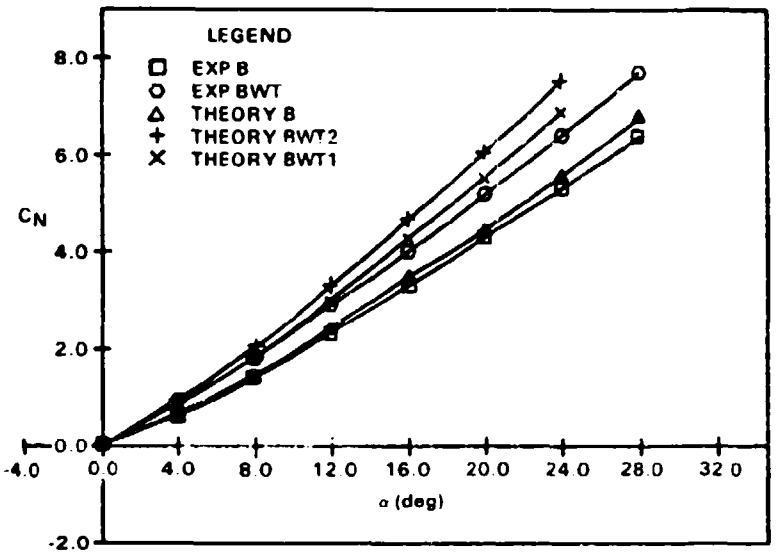

FIGURE 28. C_N COMPARISON FOR A 3/1 ELLIPTICAL CROSS-SECTION BWT CONFIGURATIONS, $M_\infty = 2.96$

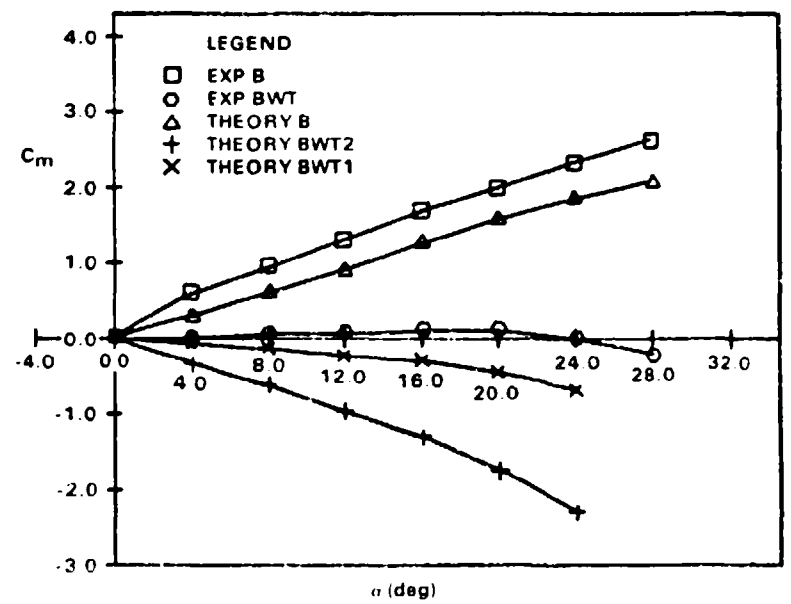

FIGURE 29. C_m COMPARISON FOR A 3/1 ELLIPTICAL CROSS-SECTION BODY CONFIGURATION, $M_\infty = 2.96$

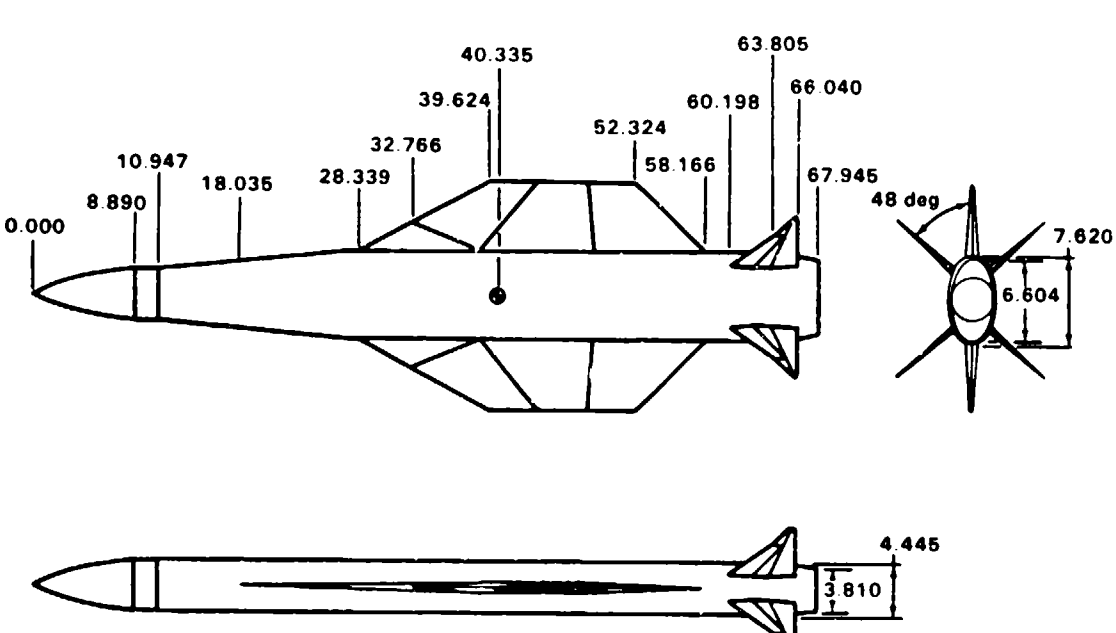

(a) $BW_CR_NT_1$

FIGURE 30. MONOPLANE-WING ELLIPTIC MISSILE MODEL (DIMENSIONS IN CENTIMETERS)

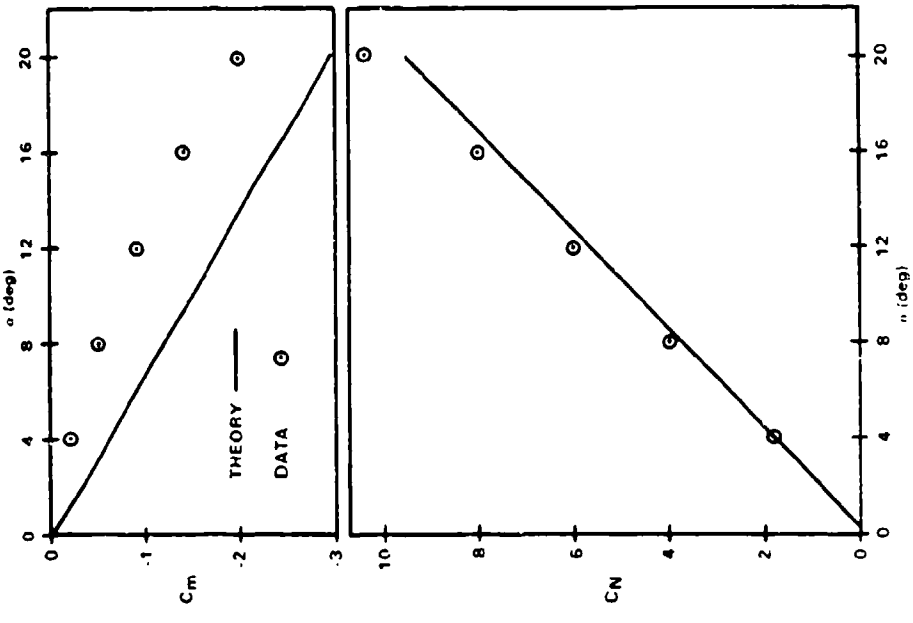

FIGURE 31. C_N and C_m COMPARISONS FOR A MONOPLANE-WING ELLIPTIC MISSILE MODEL, $M_\infty = 2.86$

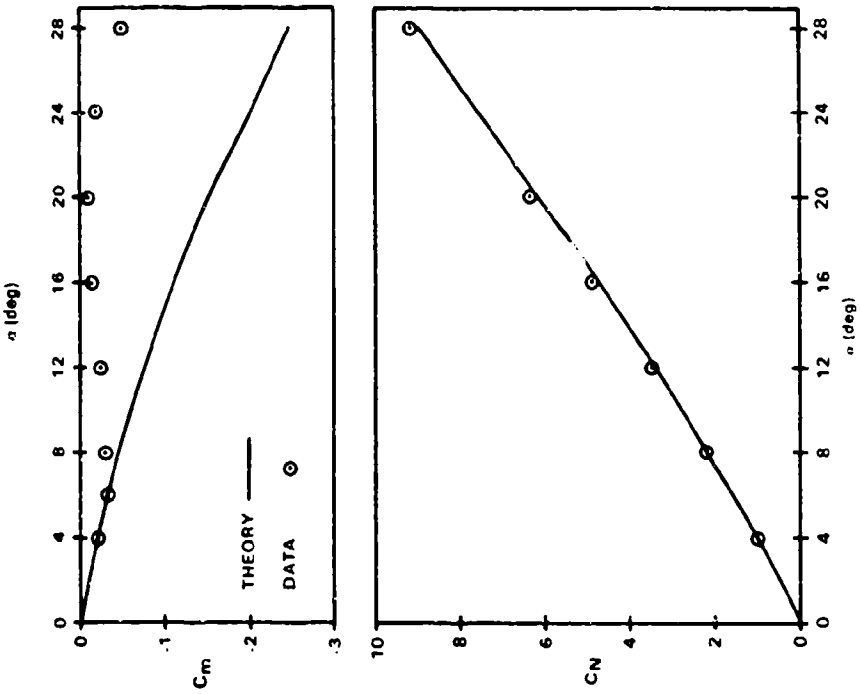

FIGURE 32. C_N AND C_m COMPARISONS FOR A 3/1 ELLIPTIC MONOPLANAR MISSILE MODEL AT HIGH ANGLE OF ATTACK, $M_\infty = 2.0$

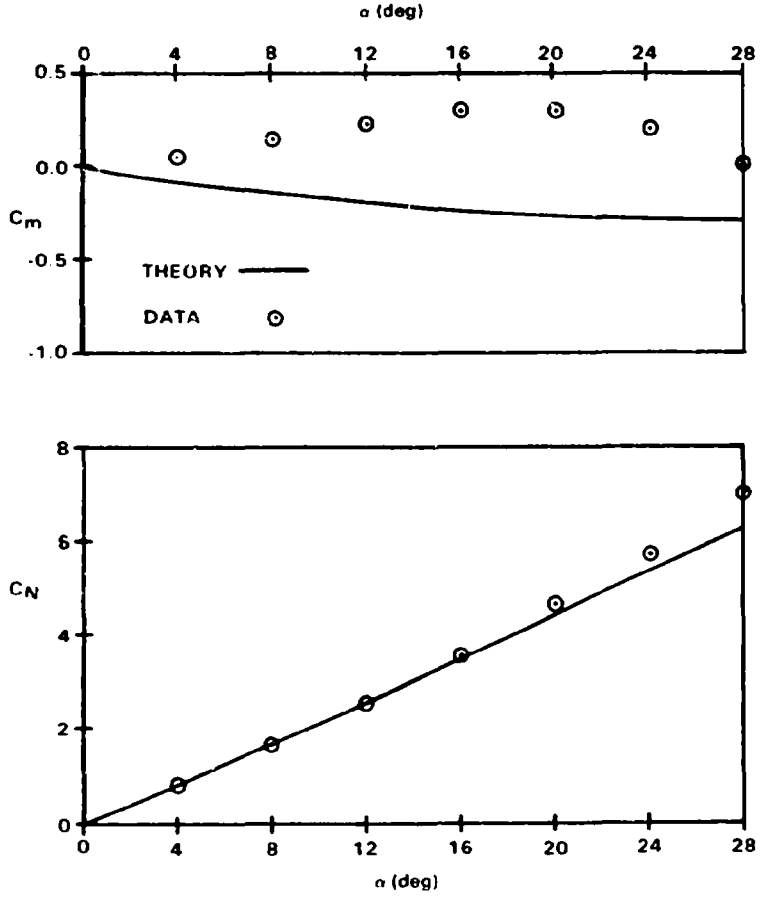

FIGURE 33. C_N and C_m COMPARISONS FOR A 3/1 ELLIPTIC MONOPLANAR MISSILE MODEL AT HIGH ANGLE OF ATTACK, $M_\infty = 3.95$

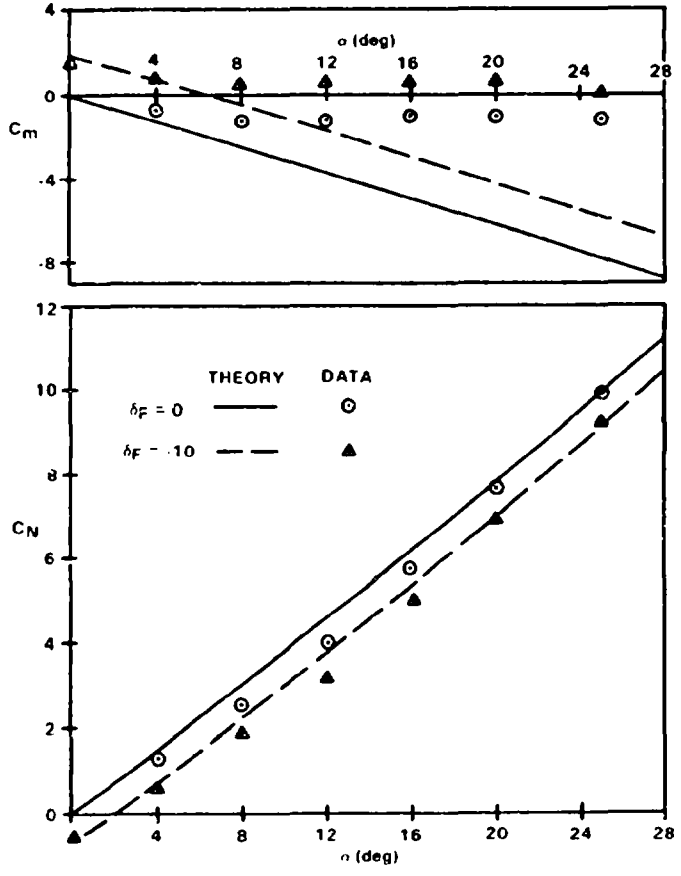

FIGURE 34. C_N AND C_m COMPARISONS FOR A 3/1 ELLIPTIC MONOPLANAR MISSILE MODEL AT HIGH ANGLE OF ATTACK, $M_\infty = 1.3$

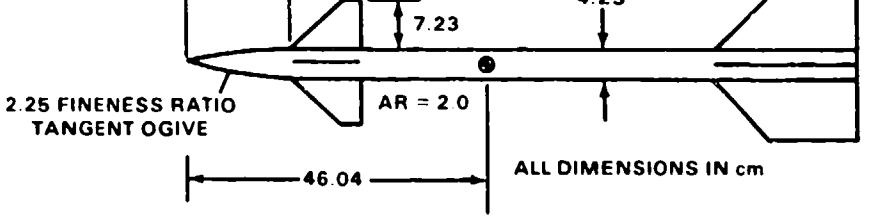

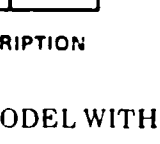

TAIL	KING
ROOT CHORD	21.59
TIP CHORD	12.65
SEMI-SPAN	9.04
AR	1.06

TAIL FIN DESCRIPTION

FIGURE 35. NASA/LRC TF-4 MISSILE MODEL WITH KING-SIZE TAIL FINS

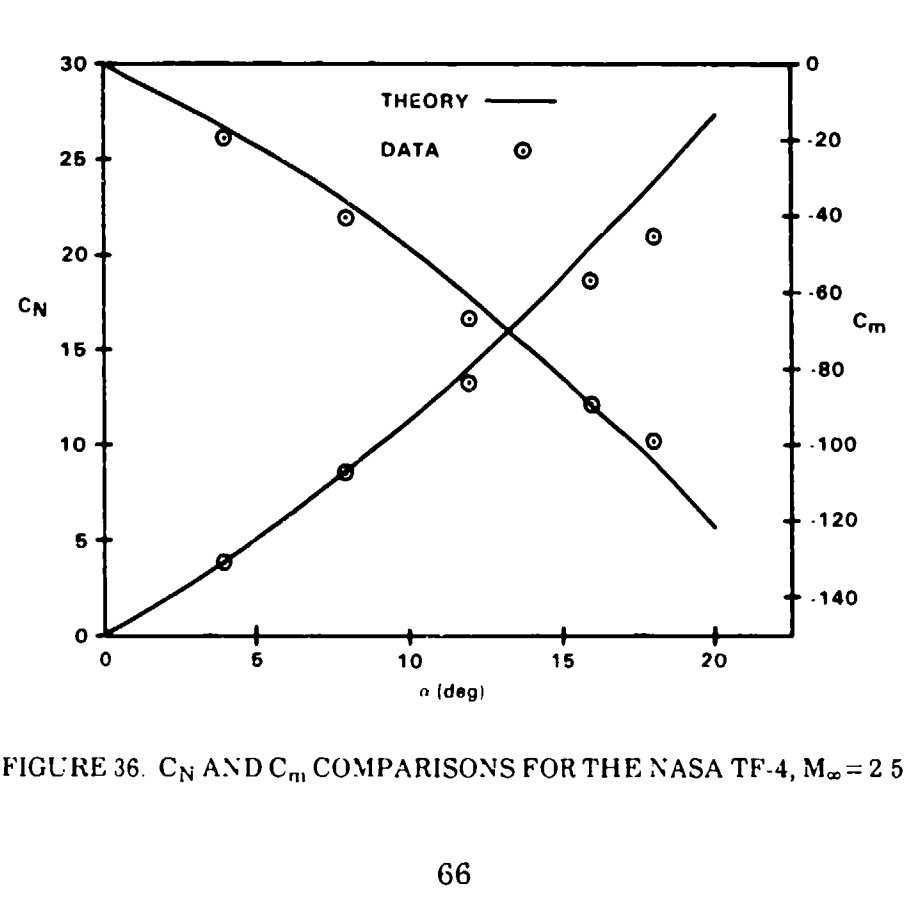

FIGURE 36. C_N AND C_m COMPARISONS FOR THE NASA TF-4, $M_\infty = 2.5$

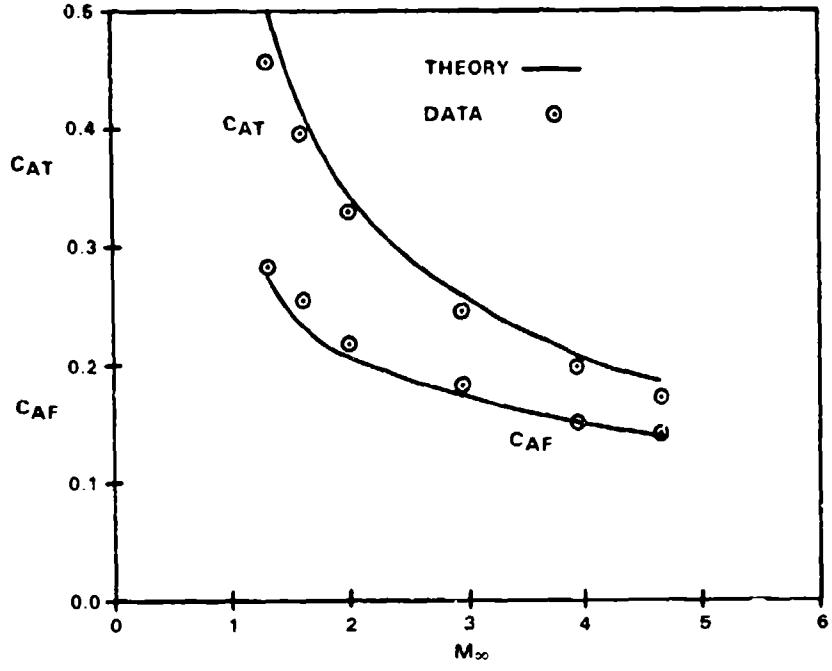

FIGURE 37. FOREBODY AND TOTAL AXIAL FORCE COMPARISONS FOR A 3/1 ELLIPTIC BODY MONOPLANAR MISSILE MODEL, $\alpha = 0$ DEG

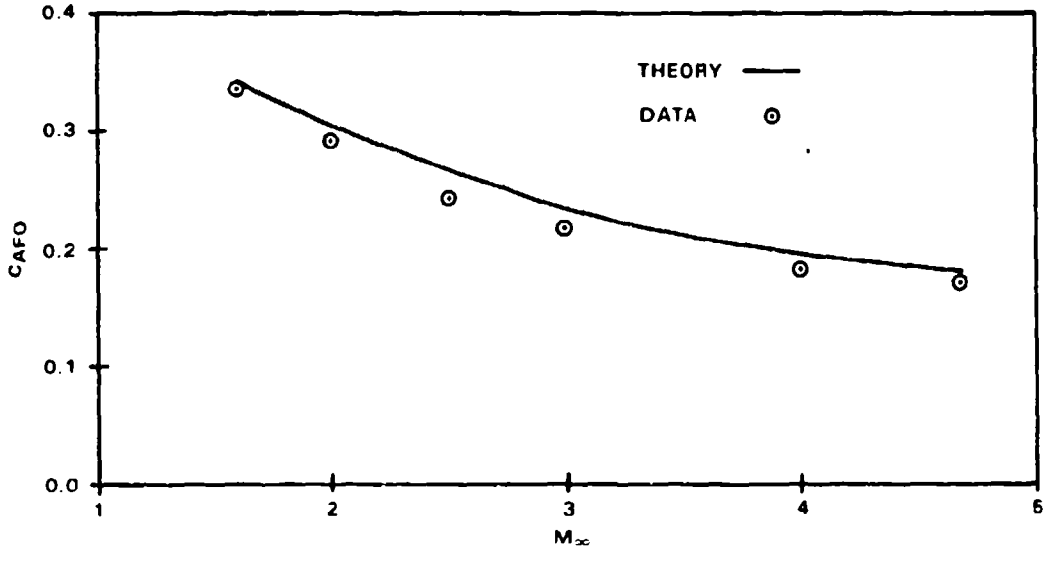

FIGURE 38. FOREBODY AXIAL FORCE COMPARISON FOR A 3/1 ELLIPTIC BODY MISSILE MODEL, $\alpha = 0$, $\delta_f = -10$

TABLE 1. LOCAL SOLUTION PREDICTION METHODS

Cross-Sectional Shape	Body Section	(Windward Plane)	(Leeward Plane)
Circular	Nose	Dahlem-Buck	Dahlem-Buck
	Body	Inclined Cone	ACM Emperical
Noncircular	Nose	Dahlem-Buck	Dahlem Buck
	Body	Tangent-Cone	ACM Emperical
.....	Fins/Wing	Tangent-Wedge	Prandl-Meyer

TABLE 2. COMPARISON COMPUTATIONS FOR BODY/FIN I CONFIGURATIONS, $M_\infty = 2.0$, $\alpha = 5$ DEG, $x' = 3.0$ CALIBERS FROM NOSE, A_R = CYLINDER CROSS-SECTION, L_R = CYLINDER DIAMETER

Case	C_A	C_N	C_m
FIN 1			
$\delta = 0$, t/c = 0.0			
NANC (first)	0.091	0.81	-1.09
NANC (second)	0.097	0.83	-1.09
SWINT	0.096	0.83	-1.13
FIN 1			
$\delta = 0$, t/c = 0.1			
NANC (first)	0.21	0.78	-1.03
NANC (second)	0.21	0.77	-0.90
SWINT	0.19	0.77	-0.96
FIN 1			
$\delta = -10.0$, t/c = 0.0			
NANC (first)	0.21	-0.26	1.52
NANC (second)	0.21	-0.24	1.54
SWINT	0.19	-0.26	1.54
FIN 1			
$\delta = -10.0$, t/c = 0.1			
NANC (first)	0.30	-0.22	1.45
NANC (second)	0.30	-0.17	1.33
SWINT	0.29	-0.18	1.29
FIN 2			
$\delta = 0$, t/c = 0.1			
NANC (first)	0.23	1.01	-1.7
NANC (second)	0.23	1.00	-1.57
SWINT	0.21	1.00	-1.73
FIN 3			
$\delta = 0$, t/c = 0.1			
NANC (first)	0.24	0.98	-1.65
NANC (second)	0.25	0.97	-1.53
SWINT	0.21	0.88	-1.39
FIN 3			
$\delta = 0$, t/c = 0.0			
NANC (first)	0.091	1.02	-1.79
NANC (second)	0.097	1.03	-1.77
SWINT	0.096	0.96	-1.65
FIN 4			
$\delta = 0$, t/c = 0.0			
NANC (first)	0.091	1.04	-1.18
NANC (second)	0.097	1.18	-1.37
SWINT	0.096	1.18	-1.50

TABLE 3. SEMI-MAJOR, SEMI-MINOR AXIS VARIATIONS FOR VARIABLE ELLIPTICAL CROSS-SECTION BODIES

Sharp-Nose Body			Blunt-Nose Body		
x/L	a/L	b/L	x/L	a/L	b/L
0.0000	0.0000	0.0000	0.0000	0.0000	0.0000
0.0100	0.0071	0.0024	0.0216	0.0217	0.0217
0.0200	0.0118	0.0039	0.0258	0.0222	0.0219
0.0250	0.0140	0.0047	0.0799	0.0337	0.0257
0.0500	0.0234	0.0078	0.1340	0.0452	0.0287
0.0750	0.0314	0.0105	0.1881	0.0564	0.0311
0.1000	0.0388	0.0129	0.2423	0.0673	0.0332
0.1250	0.0455	0.0152	0.2964	0.0777	0.0349
0.1500	0.0518	0.0173	0.3505	0.0875	0.0365
0.2000	0.0633	0.0211	0.4046	0.0965	0.0378
0.2500	0.0737	0.0246	0.4587	0.1048	0.0389
0.3000	0.0831	0.0277	0.5669	0.1177	0.0405
0.3500	0.0915	0.0305	0.6210	0.1220	0.0410
0.4000	0.0991	0.0330	0.6481	0.1233	0.0412
0.4500	0.1059	0.0353	0.6800	0.1237	0.0412
0.5000	0.1118	0.0373	0.7000	0.1229	0.0413
0.5750	0.1188	0.0396	0.7292	0.1190	0.0418
0.6000	0.1206	0.0402	0.7500	0.1166	0.0421
0.6250	0.1221	0.0407	0.7833	0.1093	0.0431
0.6500	0.1231	0.0410	0.8000	0.1066	0.0435
0.6800	0.1237	0.0412	0.8314	0.0965	0.0452
0.7000	0.1234	0.0411	0.8500	0.0945	0.0458
0.7292	0.1221	0.0407	0.8716	0.0867	0.0476
0.7500	0.1213	0.0404	0.9000	0.0813	0.0492
0.7833	0.1188	0.0396	0.9250	0.0748	0.0514
0.8000	0.1180	0.0393	0.9500	0.0687	0.0540
0.8314	0.1146	0.0382	0.9750	0.0635	0.0567
0.8500	0.1139	0.0380	1.0000	0.0595	0.0595
0.8716	0.1113	0.0371			
0.9000	0.1096	0.0365			
0.9250	0.1075	0.0358			
0.9500	0.1056	0.0352			
0.9750	0.1039	0.0346			
1.0000	0.1030	0.0343			

NOMENCLATURE

a_∞	Free-stream speed of sound
A	$u_1[\frac{1}{2} q_1^2 - (2-\gamma)/6\, M_\infty^2 u_1^2 - 1] + \cos\alpha\cos\beta[q_1^2 + q_1 q_\infty + (\gamma-1)/2\, M_\infty^2 u_1]$, second-order gradient component.
A_R	Reference area
B = 0,1.	Body boundary condition factor
C	Source vector in conservation equation (see E)
C_A	Axial force coefficient
C_{AB}	Base axial force coefficient
C_{AF}	Skin friction axial force coefficient
C_F	$F/(A_R Q_D)$, general force coefficient
C_ℓ	Roll moment coefficient
C_m	Pitching moment coefficient
C_M	$M/(A_R L_R Q_D)$, general moment coefficient
C_n	Yawing moment coefficient
C_N	Normal force coefficient
C_p	$(p/p_\infty - 1)/(\gamma/2\, M_\infty^2)$, pressure coefficient
C_Y	Side force coefficient
D	Circular body diameter or equivalent circular body diameter
DO	$\Delta\xi$ at the body boundary
E	Conservation vector (two or three components). Unified almost conservation form vector equation for flow field, body surface, and fin surface is

$$\frac{\partial E}{\partial x} + \frac{\partial G}{\partial \xi} + \frac{\partial H}{\partial \theta} = C + q_N \left(\frac{\partial S}{\partial \xi} + \frac{\partial T}{\partial \theta} \right)$$

E_x

$$- \left[R + x \frac{\partial R_b}{\partial x} (1 - \xi) \right]$$

E_T

$$- \frac{\partial R_b}{\partial \theta} (1 - \xi)$$

F	General force, or fin surface boundary condition factor (F = 0,1.0)
$F_{1,2}$	First- and second-order conical potential functions
G	See E
H	See E
i	Grid index for constant x plane
i'	Unit vector in x direction
j	Grid index for constant θ plane
j'	Unit vector in r direction
JM	Maximum j value
k	Grid index for constant ξ value
k'	Unit vector in θ direction
KI, KO	Minimum and maximum k on a fin
KM	Maximum k value
L	Body or element length
L_c	Conversion factor from length units to feet
L_f	Mean aerodynamic chord for a fin
LM	Aerodynamic symmetry mode
$L_R = X_R$	Reference length
M	General moment or local Mach number
M'	Local Mach number at the end of a body

M_∞	Free-stream Mach number
n	Normal distance from a body cross-section boundary curve (in the plane of section) or unit normal from a solid surface
p	Local pressure
p_∞	Free-stream pressure

* All q values below are nondimensional

q	Perturbation velocity vector
q_c	Crossflow component of perturbation velocity vector
q_N	$M_\infty^4 (q_{1c}^2) (2-\gamma)/(2\beta^2)$
q_r	$v_1 q_1^2/2 + v_\infty (q_\infty \cdot q_1 + q_1^2) + (\gamma-1) M_\infty^2/\beta^2 [v_\infty/2 (v_1^2 - w_1^2) + w_\infty v_1 w_1]$
q_θ	$w_1 q_1^2/2 + w_\infty (q_\infty \cdot q_1 + q_1^2) + (\gamma-1) M_\infty^2/\beta^2 [-w_\infty/2 (v_1^2 - w_1^2) + v_\infty v_1 w_1]$
q_1	First-order perturbation vector
q_{1c}	First-order crossflow perturbation vector
q_2	Second-order perturbation vector
q_{2c}	Second-order crossflow perturbation vector
q_∞	Free-stream velocity vector
$q_{\infty c}$	Crossflow component of free-stream velocity vector
Q	Total velocity vector
Q_D	$p_\infty \gamma / \cdot M_\infty^2$, dynamic pressure
r	General cylindrical coordinate radius
r_b	Body radius
r_i, r_o	Minimum and maximum radial distance on a fin for a value of x
R	r/x
R_b	r_b/x

RMI	Minimum fin radial distance
RMFN	Reynolds number per Mach number per foot per million $= \rho_\infty a_\infty/(\mu_\infty 10^6)$
RNF	Reynolds number per foot = RMFN $(10^6)(M_\infty)$
RNL	Element Reynolds number
s	r – RMI or curve arc length
SMA	Maximum s for a fin
S	See E
S_w	Wetted surface area
t	Fin thickness
t_x	Fin slope
T	See E
u_1, u_2	x components of q_1 and q_2
u_{2e}	$u_2 + M_\infty^2/\beta^2 A$
u_∞	$\cos\alpha \cos\beta$, x component of q_∞
U	x component of Q
v_1, v_2	r component of q_1, q_2
v_{2e}	$v_2 - M_x^2 q_r$
v_∞	$\sin\beta \sin\theta + \sin\alpha \sin\beta \cos\theta$, r component of q_∞
V	r component of Q
v_{s1}, v_{s2}	First- and second-order tangential velocity components
w_1, w_2	θ components of q_1, q_2
w_{2e}	$w_2 - M_x^2 q_\theta$
w_∞	$\sin\beta \cos\theta - \sin\alpha \cos\beta \sin\theta$, θ component of q_∞
W	θ component of Q
x	Distance from nose
x' = XCG	Moment center from the nose

XMI	Minimum x for a fin
XMA	Maximum x for a fin
X_R	See L_R
y	Cartesian distance to right looking downstream
z	Cartesian distance; up looking downstream
α	Angle of attack
β	$(M_\infty^2 - 1)^{\frac{1}{2}}$
β'	Sideslip angle
γ	Heat capacity ratio
δ_f	Fin deflection
ζ	Clustering transformation for ξ variable
θ	Angle distance from z axis
θ_f	Angle location of a fin
κ	Curve radius of curvature
λ	Fin sweepback angle
μ_∞	Free-stream viscosity
ξ	Shearing transformation
ρ_∞	Free-stream density
σ	Angle from fin midplane to fin surface
ϕ	Angle clustering transformation variable, roll angle
ψ	$\theta - \theta_f - \sigma$
∇	Gradient operator
∇_c	Crossflow gradient operator

DISTRIBUTION

	Copies
Commander Naval Sea Systems Command	
Attn: SEA-62D (Mr. R. Hill)	1
Technical Library	1
Washington, DC 20362	
Commander Naval Air Systems Command	
Attn: AIR-93 (Mr. D. Hutchins)	1
Technical Library	1
Washington, DC 20361	
Commander Naval Weapons Center	
Attn: Mr. R. Van Aken	1
Mr. R. E. Smith	1
Dr. R. Berman	1
Technical Library	1
China Lake, CA 93555	
Commander Naval Ship Research and Development Center	
Attn Dr. J Schott	1
Technical Library	1
Washington, DC 20007	
Office of Naval Research	
Attn: Mr. D Siegel	1
Dr. R. Whitehead	1
Dr. S. Lykoudis	1
Dr. T. C. Tai	1
Technical Library	1
800 N. Quincy St.	
Arlington, VA 22217	
Commander Naval Development Center	
Attn: Mr. S. Greenhalgh	1
Mr. W. Tseng	1
Technical Library	1
Warminster, PA 18974	

	Copies
Superintendent U.S. Naval Academy	
Attn: Head, Weapons Dept.	1
Head, Science Dept.	1
Dr. A. Maddox	1
Technical Library	1
Annapolis, MD 21402	
Superintendent U.S. Naval Postgraduate School	
Attn Prof. T. Sarpkaya	1
Technical Library	1
Monterey, CA 95076	
Officer in Charge Naval Intelligence Support Center	
Attn: Dr. M. Krumins	1
Technical Library	1
4301 Suitland Road	
Washington, DC 20390	
Commanding Officer Naval Ordnance Station	
Attn: Technical Library	1
Indian Head, MD 20640	
Commanding Officer Naval Weapons Support Center	
Attn: Code 5062 (Mr. D. Jensen)	1
Crane, IN 47522	
Defense Intelligence Agency	
Attn: Mr. P. Murad	1
DIAC/DT-4A	
Washington, DC 20546	
Commanding General Ballistic Research Laboratory	
Attn Dr. C. H. Murphy	1
Dr. R. Sedney	1
Dr. W. Sturek	1
Mr C. Nietubicz	1
Dr. A. Mikhail	1
Technical Library	1
Aberdeen, MD 21005	

DISTRIBUTION (Continued)

		Copies
Commanding General		
ARRADCOM		
Picatinny Arsenal		
Attn:	Mr. A. Loeb	1
	Mr. H. Hudgins	1
	Mr. T. Hoffman	1
	Technical Library	1
Dover, N. J. 07801		
Commanding General		
U.S. Army Missile R and D Command		
DROMI-TDK		
Redstone Arsenal		
Attn:	Mr. Billy J. Walker	1
	Dr. C. D. Mikkelsen	1
	Technical Library	1
Huntsville, AL 35809		
Commanding Officer		
Harry Diamond Laboratories		
Attn:	Technical Library	1
Adelphi, MD 20783		
Arnold Engineering Development Center		
USAF		
Attn:	Technical Library	1
Tullahoma, TN 37389		
Commanding Officer		
Air Force Armanent Laboratory (AFATL)		
Attn:	Dr. D. Daniel	1
	Mr. F. Stevens	1
	Mr. C. Cottrell	1
	Mr. S. Korn	1
	Dr. L. E. Lijewski	1
Eglin AFB, FL 32542		

		Copies
Commanding Officer		
Air Force Wright Aeronautical		
Laboratories (AFSC)		
Attn:	Dr V. Dahlem	1
	Mr. G. O'Connell	1
	Mr. M. Pinney	1
	Dr. G. Kurylowich	1
	Mr. D. Shereda	1
	Mr. J. Jenkins	1
Wright-Patterson AFB, OH 45433		
Commanding Officer		
HQ/FTD/SDDV (72651)		
Attn:	Mr. R. S. Samuels	1
Wright-Patterson AFB, OH 45433		
USAF Academy		
Attn:	Technical Library	1
Colorado Springs, CO 80912		
Advanced Research Projects Agency		
Department of Defense		
Attn:	Technical Library	1
Washington, DC 20305		
NASA		
Attn:	Technical Library	1
Washington, DC 20546		
NASA		
Ames Research Center		
Attn:	Dr. G. Chapman	1
	Dr. J. Nielsen	1
	Technical Library	1
Moffet Field, CA 94035		
NASA		
Langley Research Center		
Attn:	Mr. J. South	1
	Mr. C. M. Jackson, Jr	1
	Mr. W. C. Sawyer	1
	Mr. J. M. Allen	1
	Dr. J. Townsend	1
	Technical Library	1
Hampton, VA 23365		

DISTRIBUTION (Continued)

	Copies
Virginia P.I.S. University	
Department of Aerospace and Ocean Engineering	
Attn: Prof. J. A. Schetz	1
Prof. B. Grossman	1
Technical Library	1
Blacksburg, VA 24060	
North Carolina State University	
Department of Mechanical and Aerospace Engineering	
Attn: Prof. F. R. DeJarnette	1
Prof. H. A. Hassan	1
Technical Library	1
Box 5246	
Raleigh, NC 27607	
The University of Tennessee Space Institute	
Attn: Prof. J. M. Wu	1
Technical Library	1
Tullahoma, TN 37388	
University of Notre Dame	
Department of Aerospace and Mechanical Engineering	
Attn: Dr. R. Nelson	1
Technical Library	1
Notre Dame, IN 46556	
Purdue University	
School of Engineering and Technology	
Attn: Prof. A. Ecer	1
Technical Library	1
P.O. Box 647	
1201 E. 38th St.	
Indianapolis, IN 46223	

	Copies
Stanford University	
Department of Aeronautics and Astronautics	
Attn: Prof. M. D. Van Dyke	1
Technical Library	1
Stanford, CA 94305	
University of Texas	
Aerospace Engineering and Engineering Mechanics Department	
Attn: Prof. J. J. Bertin	1
Technical Library	1
Austin, TX 78712	
Applied Physics Laboratory	
The John Hopkins University	
Attn: Mr. E. T. Marley	1
Mr. E. Lucero	1
Mr. L. E. Tisserand	1
Mr. R. E. Lee	1
John Hopkins Road	
Laurel, MD 20810	
Raytheon Missile Systems	
Bedford Laboratories	
Attn: Mr. P. Giragosian	1
Dr. D. P. Forsmo	1
Hartwell Road	
Bedford, MA 01730	
McDonnell-Douglas Astronautics Co. (West)	
Attn: Dr. J. Xerikos	1
5301 Bolsa Ave.	
Hunington Beach, CA 92647	
McDonnell-Douglas Astronautics Co. (East)	
Attn: Mr. J. Williams	1
Dr R. Krieger	1
Mr S. Vukelich	1
Box 516	
St. Louis, MO 61366	

DISTRIBUTION (Continued)

	Copies
Lockheed Missiles and Space Co, Inc.	
Attn: Dr. L. E. Ericsson	1
Mr. P. Reding	1
Sunnyvale, CA 94086	
Lockheed Missiles and Space Co., Inc.	
Attn: Mr. T. Lundy	1
Mr. Mark Miller	1
Huntsville, AL 35807	
Nielsen Engineering and Research, Inc.	
Attn: Dr. M. Mendenhall	1
Dr. M. F. E. Dillenius	1
510 Clyde Ave.	
Mountain View, CA 95043	
General Electric Co.	
Armament Systems Department	
Attn: Mr. R. Whyte	1
Burlington, VT 05401	
CALSPAN	
PWT-4T MS-600	
Attn: Dr. W. B. Baker, Jr.	1
Mr. W. A. Crosby	1
Arnold AFS, TN 37389	
Ling-Temco-Vought	
Attn: Mr. F. Prillman	1
Dr. W. B. Brooks	1
Mr. R. Stancil	1
P.O. Box 5907	
Dallas, TX 75222	
Hughes Aircraft Corp.	
Attn: Mr. R. Reed	1
Mr. R. Cummings	1
Canoga Park, CA 91304	
Sandia National Laboratories	
Attn: Dr. W. Oberkampf	1
Mr. W. Rutledge	1
Albuqueque, NM 87115	

	Copies
Martin Marietta Aerospace	
Attn: Mr. L. A. Kania	1
Mr. J. Donahue	1
Mr. M. Shoemaker	1
P.O. Box 5837	
Orlando, FL 32805	
Mortorola Inc.	
Missile System Operations	
Attn: Mr. G. H. Rapp	1
P.O. Box 1417	
Scottsdale, AZ 85252	
TRW Space and Technology Group	
Attn: Dr. T. Shivananda	1
One Space Park	
Redondo, Beach CA 90278	
TRW Electronics and Defense Sector	
Attn: Dr. T. Lin	1
Building 527	
P.O. Box 1310	
San Bernadino, CA 92402	
Dr. C. H. Lewis	
VRA, Inc.	1
P.O. Box 50	
Blacksburg, VA 24060	
Integrated Systems Inc.	
Attn: Mr M. M. Briggs	1
151 University Ave.	
Palo Alto, CA 94301	
DEI Tech. Inc.	
Attn: Mr. K. Walkley	1
Mr. G. Smith	1
11838 Bunker Blvd., Suite 500	
Newport News, VA 23606	
Grumman Aerospace Corp.	
Research and Development Center	
M.S. A 08-35	
Attn: Dr. M. J. Siclari	1
Dr. A. Cenko	1
Bethpage, NY 11714	

DISTRIBUTION (Continued)

	Copies
Olin Corporation Attn: Mr. L. A. Mason P. O. Box G Marion, IL 62959	1
United Technologies Norden Systems Attn: Dr. G. Ramanathan Mr. M. Fink M. S. K041 Norwalk, CT 06856	1 1
Aerojet Tactical Systems Co. Attn: Mr. D. O. Matejka Sacramento, CA 98513	1
General Dynamics Convair Division Attn: Mr. K. Hively Mr. D. Brower P.O. Box 85357 San Diego, CA 92138	1 1
AVCO Systems Division Attn: Mr. E. Lawlor 201 Lowell St. Wilmington, MA 01887	1
Aerojet Electro Systems Co. Attn: Dr. Y. C. Shen P.O. Box 296-III Azusa, CA 91702	1
North American Aircraft Operations Rockwell International Attn: Mr. R. Cavage Dr. E. Bonner P O. Box 92098 Los Angeles, CA 90009	1 1
PRC Kentron Attn: Dr. M. Hemsch 3221 N. Armisted Ave. Hampton, VA 23666	1
Traco Aerospace, Inc. Attn: Mr. W. Estes MIS 6-5 6500 Tracor Lane Austin, TX 78721	1
Teledyne Ryan Aeronautical Attn: Mr. J. C. Grams 2701 Harbor Drive San Diego, CA 92138	1
Goodyear Aerospace Corp Attn: Mr. S Black 1210 Massilan Road Akron, OH 44315	1
Texas Instruments, Inc. Attn: Mr. D. Vosburgh M. S. 3405 P.O. Box 405 Louisville, TX 75067	1
DYNA East Corp. Attn: Mr. W. J. Clark 3132 Market St. Philadelphia, PA 19104	1
Library of Congress Attn: Gift and Exchange Division Washington, DC 20390	1

DISTRIBUTION (Continued)

	Copies
Internal Distribution:	
E	1
E211 (Hall)	1
E231	10
E31 (GIDEP)	1
F	1
G	1
G06	1
G10	1
G13	1
G20	1
G205	1
G21	1
G22	1
G23	1
G23 (Devan)	20
G30	1
G33	1
G40	1
G42 (Graf)	1
H	1
K	1
K20	1
K204	1
K22	1
K24	1
N	1
N40	1
R	1
R44	5
U	1